Alma Mater Studiorum – Università di Bologna

DOTTORATO DI RICERCA IN

Chimica

Ciclo XXXIV

Settore Concorsuale: 03/A1

Settore Scientifico Disciplinare: CHIM/01

ESIX materials: insertion chemistry from a wide perspective

Presentata da: Dott.ssa Rosalinda Sciacca

Coordinatore Dottorato **Supervisore**

Prof.ssa Domenica Tonelli **Prof. Marco Giorgetti**

Esame finale anno 2022

To my grandparents.

INDEX

LIST OF FIGURES

LIST OF TABLES

Abstract

This thesis aim is the synthesis, characterization and ESIX proprieties studies of Prussian Blue analogues (or Metal Hexacyanometallates, MHCMs). They are distinguished by the generic formula $A_xM_y[B(CN)_6]\cdot mH_2O$ where, *x*, *y*, and *m* indicate stoichiometric coefficients, M and B are transition metals and A an alkaline metal cation. Prussian Blue (PB) analogues materials exhibit excellent physicochemical characteristics as ionic sieve. Moreover, their face-centered cubic crystal structure and the possibility to change the transition metal leads them to be an extremely versatile compound, in terms of synthesis and applications.

Properties and structures of these synthetized compounds, are investigated by using a multi-technique approach including X-ray Powder Diffraction (XRD), Scanning Electron Microscopy (SEM), Infrared Spectroscopy (IR) and electrochemical measurements. They were obtained both via electrochemical and chemical synthesis on the basis of the application field.

The main topic is related to the MHCFs release/uptake capabilities, specifically associated to structural changing.

Furthermore, their environmental sustainability and their wide field of application from sensing to batteries, allow to define them as innovative materials suitable for new analytical technologies.

Finally, the synthesis and characterization of green rust thin film is deepened, highlighting the electrochemical behavior of Akaganèite, which has a key role in the corrosion progress. Thus, understanding the electrochemical reaction involved in the corrosion processes, is useful for the diagnosis and prevention of artefacts. Also, VIMP

technique allows to compare the controlled-electrodeposited green rust electrochemical behaviour with the real sample one.

Chapter 1

Introduction

1.1 Metal-Hexacyanometallates

Metal- Hexacyanometallates or Prussian Blue analogues (PBAs) are compounds with the general formula $A_xM_y[B(CN)_6]\cdot zH_2O$, where x, y and z are stoichiometric coefficients, M and B are transition metals and A an alkaline metal. Metal-Hexacyanometallates structure is characterized by the binding of cyanide ion to metals in both terminals, making M-CN-M´ bridges that are usually linear [1]. Furthermore, as mixed-valance compounds the charge transfer mediated by cyano ligand is allowed.

Metalhexacyanoferrates are the commonly studied materials, and the most known one is Prussian Blue (PB), that was used in the 18th century in painting and, later, in photography [2,3].

The serendipitous finding of Prussian Blue is related to Heinrich Diesbach of Berlin in 1704, who obtained a blue-colour during the preparation of crimson lake colour. This mistake was due to a contamination of potash (Potassium carbonate) with the “animal oil” of an alchemist, containing cyanide group originating from the thermal degradation of molecules, such as haemoglobin. So Prussian Blue is the first synthetic pigment [4].

If iron (III) and hexacyanoferrate (III) ions are mixed in a water solution, a dark-yellow complex was achieved (Prussian Brown, PX). PX electroreduction produces PB as a thin film:

$$Fe^{III}[Fe^{III}(CN)_6] + e^- \rightleftharpoons Fe^{III}[Fe^{II}(CN)_6]^- \quad (1)$$

PX PB

Neff [5] reported for the first time a characterization of an electrodeposited PB thin film and its cyclic voltammetry shows the reversible oxidation and reduction of Prussian Blue (Fig.1)

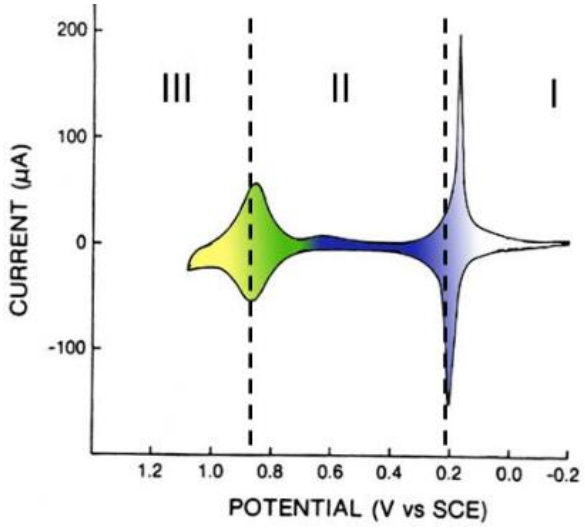

Figure 1.1. Cyclic voltammetry of a Glassy Carbon electrode modified[5]

with Prussian Blue using KCl 0,1 M as supporting electrolyte, scan rate: 40 mV s^{-1}, reference electrode: Ag/AgCl.

Figure 1 shows three redox states: in the second region, between 0.2 V and 0.9 V, the PB thin film shows the typical Prussian Blue colour, while the first region is characterized by the reduction to Prussian White (PW) and the discoloration of the film. This redox reaction is counterbalanced by the intercalation of cations (A^+) according to:

$$Fe_4^{III}[Fe^{II}(CN)_6]_3 + 4e^- + 4A^+ \rightleftharpoons A_4Fe_4^{II}[Fe^{II}(CN)_6]_3 \quad (2)$$

PB PW

Finally, the third region, with potential >0.9V, is characterized by the PB oxidation to Prussian Green (PG) as the following equation:

$$Fe_4^{III}[Fe^{II}(CN)_6]_3 - 3e^- + 3A^- \rightleftharpoons A_3Fe_4^{III}[Fe^{III}(CN)_6]_3 \quad (3)$$

PB PG

The electrochemical behavior of Prussian Blue was extensively analyzed years later than 1978, [6,7,8] and the analytical applications of PB thin film deposited on different supports were investigated [9].

Nowadays, this class of inorganic polymeric compounds is interesting for its chemical-physical proprieties like electrochromic [10 11], charge storage[12, 13], thermocromism [14] and cation exchange [15,16] , and for its technological applications.

1.1 Structure

The structure of PB was characterized for the first time by Keggin and Miles [17] who reported:

[..] The iron atoms are arranged, ferrous and ferric alternately, at the corners of a cubic lattice of 5.1 Å edge, and the CN groups lie in the edges of these small cubes. The alkali atoms occur at the centres of alternate small cubes. [..]

Then Buser *et al.*[18] well-studied the PB structure by XRD analysis, highlighting a cubic cell with a length of about 10 Å and a low density (1.8 g/cm3). The lower density is caused both by the iron atoms bonds and by the presence of vacancies and cavities in the 3D- lattice.

As shown in figure 2a PB structure contain alternately iron 2+ and 3+ linked by C-N pairs. the coordinated water molecules are attached to six Fe3+ ions. The other 8 water molecules (non-coordinated) are allocated in the vacancy, as the 8c sites of the unit cell.

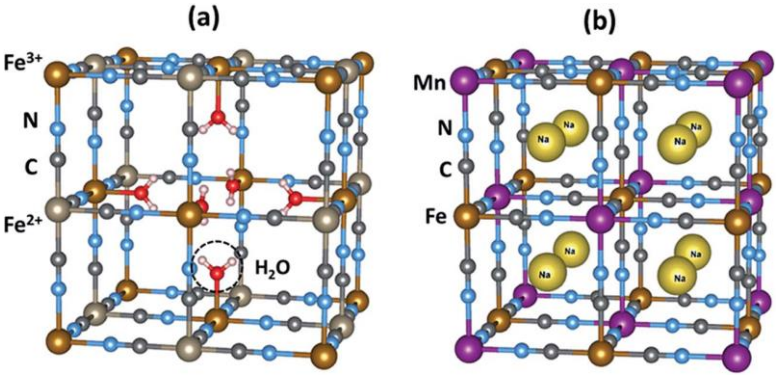

Figure 1.2 (a) Unit cell of the original Prussian blue (PB) $Fe_4[Fe(CN)_6]_3 \cdot n \times H_2O$ compound. Only "coordinated" water molecules are shown. (b) Prussian blue analogue (PBA) $NaxMnFe(CN)_6$ structure. All possible 8c positions of alkali ions are shown

Their channels size allows to host cations inside, in reversible ion intercalation/release intercalation reaction useful for energy storage and ionic sensors applications. Combining two transition metals instead of iron in the PB structure is possible, also the diffusion barrier can be decreased and ionic mobility can be increased concerning the characteristics of the transition metal [19].

The structure of PB was studied also by Ludi and Güdel, who defined "insoluble" another crystal structure, different from the Keggin and Miles described one, called "soluble" [18,20,21].

The difference between the two crystal structures is the replacing of ¼ of the group $[B(CN)_6]^{3-}$ with water coordinated to B octahedral and non-coordinated water molecules in the interstitial sites. The two different lattice structures result having chemical physical and electrochemical proprieties and, in addition, magnetic and optical ones.

It is worth noting that the definition "soluble" and "insoluble" is totally unconnected to the solubility of PBAs, which are insoluble in common solvents, but it is referred to their colloidal characteristics.

1.2 Synthesis approaches

Metal hexacyanometallates synthesis methods are richly reported [22–25]. The main two procedures are chemical synthesis [5,6] and electrochemical one[26,27]. The first one, allows to obtain powders of MHCF with an amount of monovalent or multivalent cations which are chosen for the synthesis. This procedure is based on the precipitation of a soluble hexacyanometallate (potassium, sodium or ammonium salt) and a soluble metal salt that represent the metal M in the structure $A_xM_y[B(CN)_6]\cdot zH_2O$.

The proprieties of the final compound, such as solubility and stability; composition, the ratio M/A in the basic formula $A_xM_y[B(CN)_6]\cdot zH_2O$; the specific size of the particle (mano or micro); the surface area; the density and crystalline structure (fcc, rhombic, cubic, rhombohedral, trigonal) and cell parameter; depend on the parameters of the experimental procedure:

- Type of reagents and their molar ratio;
- The addition of reagents (simultaneous or successive addition);
- The order (metal into hexacyanoferrate or vice versa);
- The velocity of the adding (drop by drop, slow or fast);
- The temperature;
- The aging;
- The work up of the product, like drying condition [19,28–30].

All these variables may be responsible of changing that influences the reproducibility of the results. For this reason, an alternative way consists in the “in-drop” synthesis of the MHCF, thanks to a mixing of the reagents in a single drop through two needles by a peristaltic pump.

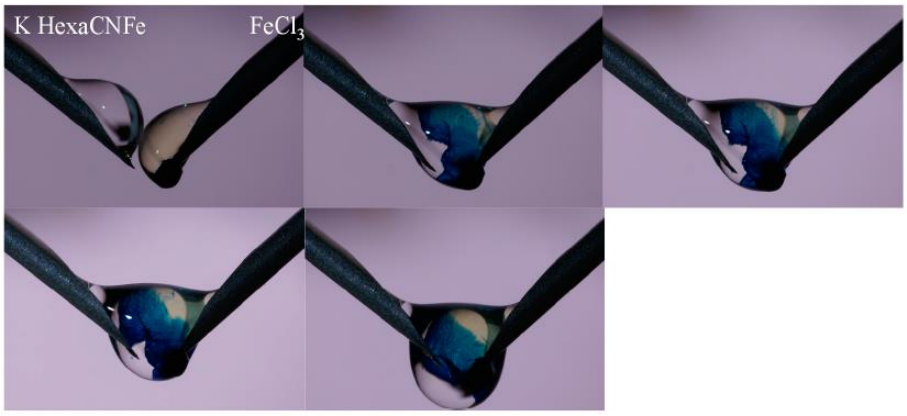

Figure 1.3."In-drop" synthesis of Prussian Blue31

Temperature and drying are important parameters for the sorption capacity, which enhances if the water releasing is fast. Also, the crystal structure changes with the progressive increasing of the temperature because of the crystallization water loss.

MHCF thin films are used in several applications (sensors, ion exchangers) thanks to the electrodeposition, an electric current driving synthesis in presence of the two precursors and a support electrolyte. Electrodeposition can be a versatile, fast and simple way to obtain MHCF modified electrodes or thin films using potentiostatic [32] or potentiodynamic techniques [33].

The films can be obtained by the in situ dosed of the metal ion on an active metal anode, for copper [34] and nickel [35] analogues.

The thin film can modify an inert electrode, such as gold, glassy carbon, graphite or platinum, by a in situ precipitation from a metal ion and ferricyanide diluted solution. The film obtained (MHCF) on the electrode surface is insoluble and it results testable by potentiodynamic analysis. The characterization can occur by other analysis such as XRD, while the growth of the film on the electrode can be quantified by electrochemical quartz crystal microgravimetry (EQCM) [36,37].

The potential window and the number of potentiodynamic cycles determine the stoichiometric composition of the MHCF films, according to the InHCF case [38]. Also, the M:Fe ratio is another parameter that characterizes the oxidation state of MHCF deposited.

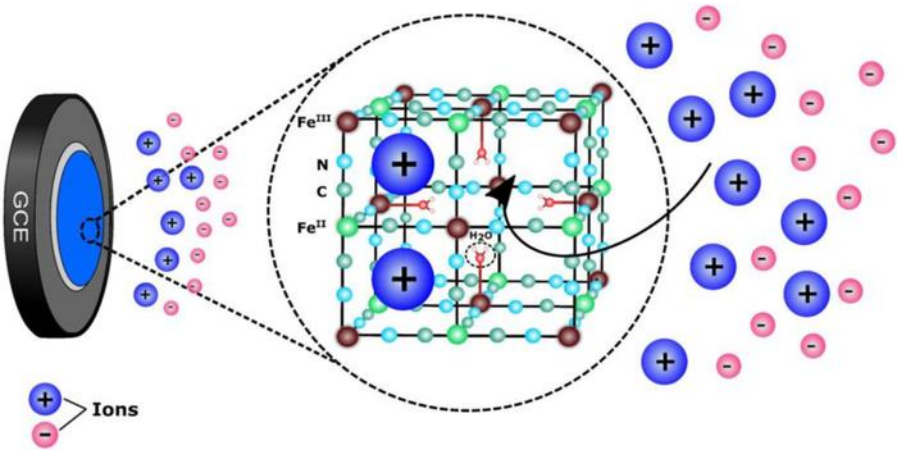

Figure 1.4. Representation of the modified electrode to electrodeposition and the intercalation of ions within the PB lattice39.

For PB electrodeposition, a the cathodic polarization takes place on an electrode soaked in a solution of $FeCl_3$ and $K_3Fe(CN)_6$. Cyclic voltammetry, galvanostatic and potentiostatic deposition can be used. Itaya, and others later, confirmed the deposition of insoluble form without potassium ions intercalated [40–42].

1.3 Proprieties and applications

Magnetic proprieties

Prussian blue can:

- can be synthesized at room temperature obtaining chemically stable structures;

- can be substituted by wide range of metals with different spin and oxidation states;

- create covalent link obtaining a final 3D network;

- the cyanide bridging structure allows magnetic exchange couplings between paramagnetic centers.

These proprieties make PB an attractive candidate for new molecule-based magnets [43].

MHCM characteristics are associated with the flexibility of their nanostructures due to the stretching and vibrational modes of cyano-bridging ligand. Magnetic field [44,45] and light [46,47] in a specific crystal environment are external conditions that can change the electromagnetic configurations. Generally, cyano-bridged metal complexes show charge-transfer (CT) phase transitions and change in magnetic proprieties. In MHCM, the electron delocalization and the octahedral symmetry preservation in the electronic ground state would be allowed by a strong electronic coupling. Otherwise, intramolecular distortion and solvation could stabilize the charge-transfer excited state, creating an electron localization and reduction of the molecular symmetry.

M^I/M^{II} ratio control leads to specific electronic spin states of MHCF containing alkali metals. They tolerate several electronic spins, which limit super-exchange interactions across the cyanide bridges and allow the magnetism and coloration changing [45,48].

Furthermore, valence M^I and M^{II} can be easily obtained by redox processes electrochemically performed [49], which is associated to an *in situ* metal alkali composition, as A^I/A^{II} ratio. This process takes place thanks to the PBAs framework structure that allow a potential-controlled ion exchanging, between the MHCM and solution to balance out the charge. During this compositional control, the ion can be allocated into two types of vacancies: ones adjacent to the $Fe(CN)_{6-m}m(H_2O)$ preferentially occupied, while other sites are not adjacent to the $Fe(CN)_{6-m}m(H_2O)$ and they endure repulsive interactions. These ones are occupied

when all sites of the first type of vacancies are already occupied, that represent fraction of 25% [50].

Thus, the *in situ* structural changeover entails physical-chemical changes as electromagnetic materials, such as their mechanical or magnetic properties. The stretching and vibrational modes of the cyanobridging ligand in PBAs lead to a typical structural flexibility. They are also characterized by the ligand-to-metal charge transfer mediated by the cyano ligand, for this reason classified as mixed-valence compounds. Hence, Magnetic proprieties are controlled by the atomic composition ratio of (high spin metallic sites)/(low spin metallic sites).

These features play important roles in the various magnetic functionalities of Prussian Blue analog-based magnets which are well-reported [51].

1) *Charge-transfer phase transition*: a metal ion and lattice strain interaction produce thermal phase transition. Because of strong interaction due to the bridged CN- ligand, in Prussian blue analogs thermal phase transitions are possible.
2) *Reversible photomagnetism*: several cyano-bridged bimetal assemblies, such as Cobalt Hexacyanoferrate, exhibit a photomagnetic effect. The electron spin state of a magnetic material can be changed obtaining an optical control of magnetization.
3) *Second harmonic generation (SHG) and magnetization-induced SHG (MSHG):* In $A^{I}B^{II}[M^{III}(CN)_6]$, the position of the A ion produces a $\bar{4}$ rotoinversion operator, *i.e.*, the crystal structure is noncentrosymmetric. *F*$\bar{4}$*3m*-type Prussian blue analog-based magnets are piezoelectric ferromagnets; that is, they are condensed matter with both piezoelectricity and ferromagnetism.

4) *Ferroelectric ferromagnetism*: to observe ferroelectric ferromagnetism, the attention is focused on hexacyanometallate-based materials because cyano-polymers are ferroelectric (at T_c 5.6 K, below Curie temperature, the Metal-Hexacyanoferrates exhibit a long-range ferromagnetic ordering).

5) *Humidity-sensitive magnetism*: vacancies of $B^{II}[M^{III}(CN)_6]_{2/3}\cdot zH_2O$ are filled with ligand water molecules coordinated to the B ion and non-coordinated water molecules. So, the magnetic material exhibits a humidity-sensitive characteristic, hence the magnetic variations can measure the humidity.

Electro- and thermo-chromism

Electrochromism is a property of a material that is able to change color or transparency to solar radiation in a reversible way, if they are undergone an electrochemical potential, that is, an electron-transfer (redox) process. Hence, switching between redox states fit with different visible region electronic absorption bands.

If in the compound more than two redox states are electrochemically available, the electrochromic material may exhibit several colors (polyelectrochromic). Electrochromic materials, have several advantages:

- A small switching voltage (1-5 V);
- Show specular reflection;
- Possess a gray scale;
- Require power only during switching;
- Exhibit adjustable memory, up to 12-48 hours.

Nowadays, the research field of electrochromic compounds is very broad and includes inorganic, organic, and polymeric, as well as several hybrid materials, covering

a range of technology for the glazing, mirrors, transparent displays, etc.

Surely, an electrochromic device must have an ion-containing material (electrolyte) in close proximity to the electrochromic layer, as well as transparent layers for applying a distributed electric field.

Table 1 shows some Metal-Hexacyanoferrates electrochromic propriety, on the base of their redox states.

Table 1 Electrochromic property exhibited by Metal-Hexacyanoferrate compounds.

Compounds	**Color of the reduced species**	**Color of the oxidized species**
CuHCF	Red-brown	Yellow
NiHCF	Gray	Yellow
InHCF	White	Pale yellow
CoHCF	Green	Red-magenta
CrHCF	Gray	Blue
PdHCF	Green	Orange
VHCF	Yellow	Green

Thermochromism is related to the color variation if the temperature changes. Inorganic compounds get often change color because of the crystalline phase variation, or a change in ligand geometry, or a change in the number of molecules in the coordination solvent sphere. Several examples about CoHCF are known [52]. As a matter of fact, CoHCF film with caesium or potassium intercalated change color from olive-brown to green by heating (ca. 61°C). this phenomenon is explained by a partial dehydration, from octahedral $Co(H_2O)_6^{2+}$ to less hydrated structure, tetrahedral $Co(H_2O)_4^{2+}$.

Hence, for cobalt compounds is easily identify the degree of solvation Co(II) in the structure because of the different coloring. As well as the counteractions hydrated accommodated into the CoHCF structure can influence the hydration, and the coloring consequently [53].

Electrocatalysis

The zeolitic structure of PBAs with a cubic unit cell of 10.2 Å and with channel diameters of about 3.2 Å allows the diffusion of low molecular weight molecules (such as O_2 and H_2O_2) through the crystal. The facile deposition achieved of various Metal-Hexacyanoferrates showed excellent electrocatalytic properties.

The most common electrocatalysis example is related to the reduction of H_2O_2, in fact, Itaya describe the mechanism as hydrogen peroxide (or oxygen) penetration into the PB lattice, it is located in the center of each vacancy, in which four divalent iron ions favor the catalytic reduction of H_2O_2 through a four-electron reaction [8]. Although this mechanism can be reliable the real is still not very clear because of the difficult characterization of PB as catalyst.

Several studies report the inorganic [54] and organic [55] substrates oxidation by hexacyanoferrates, revealing that electron transfer mechanism depends both on the substrate and the medium of reaction. In biological field, hexacyanoferrates are useful as catalyst for amino acids [56,57].

These studies have been the first steps for the future applications of PB as (bio)sensors: from the amperometric detection of H_2O_2 to other substrates detailed in the following Table 2, in which are shown the Metal Hexacyanometallates electrocatalytic properties towards the substrates.

Table 2 Substrates to which Metal-Hexacyanoferrates show electrocatalytic property.

MHCF	Substrates
CuHCF	Ascorbic acid [58], NADH, Hydrazine, Hydroxylamine, Cysteine,[59] Glutathione[60] , H_2O_2 [61]
CoHCF	Ascorbic acid [62], Hydroquinone[63], NADH[64], Dopamine[65], Epinephrine,**Errore. Il segnalibro non è d efinito.** Norepinephrine,**Errore. Il segnalibro non è definito.** Hydrazine [66] , Morphine**Errore. Il segnalibro non è definito.**
CoHCF modified with Ru	Thiosulphate,**Errore. Il segnalibro non è d efinito.** p-Chlorophenol**Errore. Il segnalibro non è definito.**
NiHCF	Ascorbic acid, [67] Dopamine, [68] Hydrazine [69]
InHCF	Cysteine,[70] Glutathione,**Errore. Il s egnalibro non è definito.** 6-thiopurine,**Errore. Il segnalibro non è d efinito.** Methimazole**Errore. Il segnalibro non è definito.**
Several MHCFs	Hydrogen peroxide [71]

MHCM as Ion exchanger

The potassium intercalation into the MHCF lattice was detected for the first time in 1965[72], since then, researchers have been more and more interested in MHCMs as molecular sieves in several fields (clean-up, batteries,…). The cation intercalation in the frameworks defines mainly the electrochemical behavior of MHCMs. In fact, the

electron transfer is related to the cation insertion/ de-insertion process [73,74], which occurs as showed by the equation (5).

$$B[Fe^{III}(CN)_6]_x + yA^{n+} + y\,e^- \leftrightarrows A_yB[Fe^{II}(CN)_6]_x \quad (5)$$

The various cation species cause a potential shifting and a peak shape variation in CVs. This behavior has been reported for other MHCFs [75–77]. Furthermore, Scholz suggests a dependence between potential and metal ions coordinated in the MHCM lattice, as well [78]. Another factor influences the insertion capability is due to the cation hydration degree: Ions with smaller ionic radii have larger hydrated radii so they hold on their hydration shells. On the other hand, larger radii ions are less strongly hydrated, therefore they able to break off their hydration shells during the insertion into the MHCM lattice.

The cation insertion into the lattice and the ion-exchanger proprieties depends on the nature of the precursors used for the synthesis or electrosynthesis. Several conditions must be evaluated: firstly the use of ferro or ferricyanide can influence the oxidation state of the final product as well as experimental conditions influence its stability. [79,80]

Secondly, the monovalent cation involved (Na^+, K^+, etc.) influence the mechanism of metal binding, allowing the exchange process. [79]

Lastly, the type of metal salt (Ni, Cu, Zn, Co,…) influence the potential release of cations during the sorption process [81] as well as the chemical structure [82] and the crystallographic structure. All these features are important for the cage effect (affinity for the cation) and for the kinetics of the uptake process [79,83].

Some studies are focused on the most conventional hexacyanoferrates, such as NiHCF[28,82,84,85], CuHCF[16,29,75,80] and CoHCF[14,30,53]

Other “uncommon” metals in this field are palladium and vanadium which are used for the MHCF’s synthesis but their main application is in the electrocatalytic field.

As a matter of fact, Grandjean et al. report a different sorption capability of Cs, when the metal salt is Copper, Cobalt and Nickel, following the order Cu > Co > Ni [83].

Ayrault et al. show how the presence of alkali ion, such as K^+ in the framework is enhances the uptake kinetics and the increases the sorption capacities of the ion exchanger [79]. MHCM are suitable for recovering alkali or alkaline-earth metals including Sr[86] or Rb[87], also other metals from industrial wastewater such as Co[87], Cr[87], As[88], Cu[89]. Some hexacyanoferrates, Nickel hexacyanoferrate particularly, have been used as ionic sieve for caesium recovery, as fully reported [30,85,86,90,91].

Actually, several investigations on Cs sorption by a series of hexacyanoferrate-based materials are reported: Ramaswamy shows the log-log plot of the distribution coefficient against ammonium nitrate concentration, obtaining a slope close to one. This behaviour suggests a 1:1 ion exchange ratio Cs^+/NH_4^+[92]. The mechanism involved is very complex, depending on the structure due to the experimental condition of the synthesis procedure, confirmed by Mössbauer spectroscopy [93].

Changing in the crystalline structure can influence the stoichiometric ratio of the ion releasing or uptake, in particular in mixed hexacyanoferrate [94]. Moreover, the zeolitic material can choose to uptake/release an ion (H^+) rather than Cs if pH change [95]. Another important feature that influences the binding during the exchange process is the ionic radius of the cation. It contributes to the selectivity of the zeolitic cage for the recovery of Cs from mixed-

electrolyte solutions [96,97]. Lastly, the oxidation state of iron in MHCF impacts on the sorption proprieties [79,98].

Batteries

Recently, Prussian Blue analogues have gained attention as promising materials for alkali ion batteries because stable redox capabilities and uniform porosity are important factor for this application [99–101]. As detailed in the follow section 1.3, PBAs open framework structures allow a fast and reversible ion intercalation of several alkali cations from aqueous medium, like Li^+, Na^+, K^+ and NH_4^+. Therefore, they can be used as cathode materials for lithium or sodium secondary batteries [102]. More than monovalent cations, PBAs can reversibly guest alkaline-earth metal ions[79,103] and trivalent ions [84,104] as well. During charging and discharging processes no modification of the cells size and the structure stiffness occur, hence long PBAs' batteries have longer cycle lives.

Furthermore, PBAs have suitable characteristics for batteries applications: be safe although high volume production, be quite inexpensive, show excellent electrochemical performances usually in aqueous electrolytes, synthesized by low temperature procedure and in bulk processes.

For these reasons they gain attention especially for large-scale stationary storage batteries for supply the energy deficit due to renewable sources to the grid [105]. In the early 1990's studies were carried out on PBAs and Nafion as rechargeable batteries components [106].

Several studies report the high voltages associated to different Prussian Blue analogues and their capability to intercalate not only monovalent cations but di- and tri-valent as well [107].

Nickel [84], Copper [108], Zinc[109], Indium [33], Cobalt [110] hexacyanoferrates were studied as host of di- and tri-valent cations. This feature is noteworthy because of their promising energy efficiency [102]: if a material cans guest cations with two or three charges, the redox reaction is associated to a more energy storage than in monovalent ion batteries. The key role of the PBAs large channel structures allows the larger cations accommodation.

2. ESIX

Lilga reports the acronym ESIX for the first time, in 1996 [111]. ESIX (electrochemically switched ion exchange) is a reversible and selective method that combines electrochemistry and ion exchange. In particular, it allows to gain ion separation minimizing waste generation with lower costs. At the beginning it was used for alkali metals ion separations. Several studies for caesium recovery are available [112–114]. Later, ESIX has been applied to other cations [104,115].

For ESIX is essential to gain an ion exchange medium as an electroactive film deposited on an electrode. In this way, it is possible to manage the redox reactions, that are the uptake and release of cations, modulating potential easily. Hence, applying a cathodic potential to the film (X) is enough to lead a redox reaction that forces the uptake of a cation (A) from the solution into the film. Whereas an anodic potential (oxidation) induces the release of the cation from the film to a fresh solution containing high concentration of another cation. The reduction process occurs as:

$e^- + X + A^+ \rightarrow X\text{-}A^+$ (6)

the reoxidation follows the mechanism:

$X\text{-}A^+ \rightarrow e^- + X + A^+$ (7)

In this way the film works just as a cage, which can release the cation in a fresh high concentrated solution of a different cation in order to achieve the desalination of the first solution (waste), realising an ion exchange:

$$X\text{-}A^{+} + A'^{+} \leftrightarrows XA' + A^{+} \qquad (8)$$

Furthermore, the film can reveal a greater selectivity for a cation (A^{+}) rather than another one. It is an advantage during the uptake from a solution in which there is a mixture of cations. In this case, a competition binding occurs with a thermodynamically driven process.

2.1 EIXMs: electroactive ion exchange materials.

Materials suitable for ESIX method are defined as electroactive ion exchange materials (EIXMs), which have recently received considerable attention because of their peculiar proprieties [116]. These materials have to be suitable for an ion exchange reaction that takes place through a transferring electronic charge during a redox reaction. Therefore, EIXMs include two families of compounds which the charging and discharging processes occur easily: inorganic mixed-valence transition metals compounds and organic conducting polymers (CPs).

The best representative compounds that belong to the first class are the MHCFs, which show both electric and ionic conductivity during the electrochemical redox process. Their characteristics are extensively described below.

On the other hand, CPs are another class of EIXM because of their combination between conventional polymers and electronic proprieties of semiconductors or metals, for this reason called as “synthetic metals” [117,118].

The reversible oxidation or reduction of the conducting polymer cause the positive or negative charge generation, and the opposite charge counterions will be uptaken on released from the polymer matric neutrality conservation

[119]. CPs have been widely studied [118,120,121], in particular the modifications associated to the redox processes [106,111–113] and their applications consequently [125–127].

The electrochemical conductivity, ion transfer and exchange capability, and stability can be improved applying several strategies:

1) having a large surface area, a shortened pathway for ion transport and low interfacial impedance between the electrode and electrolyte;
2) using carbon materials to enhance the conductivity and mechanical stability;
3) developing inorganic and organic as hybrid EXIMs in order to achieve synergistic effects [128].

2.2 EXIM as Hexacyanoferrate

As described in the section 1.1 the structure of Prussian Blue (or iron hexacyanoferrate) is characterized by the cage structures in which the Fe^{II} atoms are linked by carbon atoms of cyanide ions, while Fe^{III} are surrounded octahedrally by nitrogen atoms. The charge compensation occurs with the alkali metal cations allocation in the tetrahedral sites of the structure. The unit cells are ¼ available in the "insoluble" form of PB to maintain the electroneutrality [18]. Otherwise, the empty nitrogen sites are occupied by water molecules.

Oxidation and reduction can take place both in the "insoluble" and in the "soluble" form of PB, working as a EXIM, where the ESIX process is related to the follow reactions [128,129]

$A_4Fe_4^{III}[Fe^{II}(CN)_6]_4 + 4\,A^+ + 4\,e^- \leftrightarrow A_8Fe_4^{II}[Fe^{II}(CN)_6]_4$ (9) Prussian White - "soluble"

$A_4Fe_4^{III}[Fe^{II}(CN)_6]_4 \leftrightarrow 4\,A^+ + 4\,e^- + Fe_4^{II}[Fe^{III}(CN)_6]_4$ (10) Berlin Green - "soluble"

$Fe_4^{III}[Fe^{II}(CN)_6]_3 + 4\ A^+ + 4\ e^- \leftrightarrow A_4Fe_4^{II}[Fe^{II}(CN)_6]_3$

(11) Prussian White – "insoluble"

$Fe_4^{III}[Fe^{II}(CN)_6]_3 + 3C^- \leftrightarrow 3\ e^- + Fe_4^{III}[Fe^{III}(CN)_6C]_3$

(12) Berlin Green - "insoluble"

Other MHCFs work as ionic sieve thank to their zeolitic structure that allow to accommodate cations, *i.e.* Copper Hexacyanoferrate (CuHCF), Nickel Hexacyanoferrate (NiHCF), etc.

CuHCF nanoparticles [130] and thin film [131] are studied as ionic sieve for Caesium recovery and alkali cations as well. About CuHCF, in addition to ion exchange capability, electrocatalytic proprieties are reported [61].

Also CoHCF is a good ion exchanger based on two redox couples (Fe^{II}/Fe^{III} and Co^{II}/Co^{III}) [132] and it shows the light switchable magnetism capability [133].

Furthermore, other MHCFs such as ZnHCF [109,134,135], MnHCF [136,137], InHCF [33].

NiHCF is the most studied PBA because of its open framework structure and the kinetic behaviour in sodium and potassium. It has been prepared using several methods from nanoparticles [97] to thin films [84], nanosheet [138] and nanotube [139]. In addition, NiHCF was the first PBAs used as ion exchanger from Lilga *et al.*[112] because of its selective affinity for ^{137}Cs and its well-stability, which provide for industrial applications [140]. The selectivity of PB for caesium occurs even if H_3O^+ or K^+ concentrations were higher than Cs^+ ones, with an only reducing of the adsorption amount [141]. The problem of PB and PBAs is due to their fine size particles that form a colloidal suspension. It makes the separation from the solution difficult after use. To overcome this problem, PBAs can be coupled with polymer matrix or fixed on supports [142].

Hence, the zeolitic structure of PBAs allow not only to recover radioactive cations as ^{137}Cs, but also to catch alkali cations (in desalinization processes [143], electrochemical ion sensors[144] or batteries applications [145,146]).

In particular, thallium is a high toxic rare metal, because its salts can be exchanged for K^+ by human fluids, interfering with physiological processes[147]. Many techniques are available to remove them from industrial wastewater, like precipitation, electrochemical deposition or solvent extraction)[148]. Several studies concern about the PBAs capability to remove Tl, highlighting the psysicochemical influences of PBAs [98,149].

Also, gases like ammonia can be adsorbed by PBAs, like a CoHCF, prepared by Zhang et al., cans selectively adsorb dissolved ammonia (NH_4^+) and ammonia (NH_3)[150].

References

(1) Tiwari, A.; Nordin, A. N. *Advanced Biomaterials and Biodevices*; John Wiley & Sons, 2014.
(2) *Miscellanea Berolinensia Ad Incrementium Scientiarium*; Berlin, 1710.
(3) Brown, D. **1724**, *33*, 17.
(4) Ware, M. Prussian Blue: Artists' Pigment and Chemists' Sponge. *J. Chem. Educ.* **2008**, *85* (5), 612. https://doi.org/10.1021/ed085p612.
(5) Neff, V. D. Electrochemical Oxidation and Reduction of Thin Films of Prussian Blue. *J. Electrochem. Soc.* **1978**, *125* (6), 886. https://doi.org/10.1149/1.2131575.
(6) Ellis, D.; Eckhoff, M.; Neff, V. D. Electrochromism in the Mixed-Valence Hexacyanides. 1. Voltammetric and Spectral Studies of the Oxidation and Reduction of Thin Films of Prussian Blue. *J. Phys. Chem.* **1981**, *85* (9), 1225–1231. https://doi.org/10.1021/j150609a026.
(7) Rajan, K. P.; Neff, V. D. Electrochromism in the Mixed-Valence Hexacyanides. 2. Kinetics of the Reduction of Ruthenium Purple and Prussian Blue. *J. Phys. Chem.* **1982**, *86* (22), 4361–4368. https://doi.org/10.1021/j100219a017.
(8) Itaya, K.; Uchida, I.; Neff, V. D. Electrochemistry of Polynuclear Transition Metal Cyanides: Prussian Blue and Its Analogues. *Acc. Chem. Res.* **1986**, *19* (6), 162–168. https://doi.org/10.1021/ar00126a001.
(9) Itaya, K.; Shoji, N.; Uchida, I. Catalysis of the Reduction of Molecular Oxygen to Water at Prussian Blue Modified Electrodes. *J. Am. Chem. Soc.* **1984**, *106* (12), 3423–3429. https://doi.org/10.1021/ja00324a007.
(10) Speiser, B. Electrochromism. Fundamentals and Applications. Von P. M. S. Monk, R. J. Mortimer Und D. R. Rosseinsky. VCH Verlagsgesellschaft, Weinheim, 1995. 216 S., Geb. 168.00 DM. - ISBN 3-527-29063-X. *Angew. Chem.* **1996**, *108* (7), 853–854. https://doi.org/10.1002/ange.19961080733.
(11) Carpenter, M. K.; Conell, R. S.; Simko, S. J. Electrochemistry and Electrochromism of Vanadium Hexacyanoferrate. *Inorg. Chem.* **1990**, *29* (4), 845–850. https://doi.org/10.1021/ic00329a054.
(12) Neff, V. D. Some Performance Characteristics of a Prussian Blue Battery. *J. Electrochem. Soc.* **1985**, *132* (6), 1382. https://doi.org/10.1149/1.2114121.
(13) Kaneko, M.; Okada, T. A Secondary Battery Composed of Multilayer Prussian Blue and Its Reaction Characteristics. *J. Electroanal. Chem. Interfacial Electrochem.* **1988**, *255* (1), 45–52. https://doi.org/10.1016/0022-0728(88)80003-2.
(14) Zamponi, S.; Giorgetti, M.; Berrettoni, M.; Kulesza, P. J.; Cox, J. A.; Kijak, A. M. Cobalt Hexacyanoferrate in PAMAM-Doped Silica Matrix. *Electrochimica Acta* **2005**, *51* (1), 118–124. https://doi.org/10.1016/j.electacta.2005.04.044.
(15) Coon, D. R.; Amos, L. J.; Bocarsly, A. B.; Fitzgerald Bocarsly, P. A. Analytical Applications of Cooperative Interactions Associated with Charge Transfer in Cyanometalate Electrodes: Analysis of Sodium and Potassium in Human Whole Blood. *Anal. Chem.* **1998**, *70* (15), 3137–3145. https://doi.org/10.1021/ac970975a.
(16) Tani, Y.; Eun, H.; Umezawa, Y. A Cation Selective Electrode Based on Copper(II) and Nickel(II) Hexacyanoferrates: Dual Response Mechanisms, Selective Uptake or Adsorption of Analyte Cations. *Electrochimica Acta* **1998**, *43* (23), 3431–3441. https://doi.org/10.1016/S0013-4686(98)00089-9.
(17) Keggin, J. F.; Miles, F. D. Structures and Formulæ of the Prussian Blues and Related Compounds. *Nature* **1936**, *137* (3466), 577–578. https://doi.org/10.1038/137577a0.
(18) Buser, H. J.; Schwarzenbach, D.; Petter, W.; Ludi, A. The Crystal Structure of Prussian Blue: Fe4[Fe(CN)6]3.XH2O. *Inorg. Chem.* **1977**, *16* (11), 2704–2710. https://doi.org/10.1021/ic50177a008.
(19) Paolella, A.; Faure, C.; Timoshevskii, V.; Marras, S.; Bertoni, G.; Guerfi, A.; Vijh, A.; Armand, M.; Zaghib, K. A Review on Hexacyanoferrate-Based Materials for Energy Storage and Smart Windows: Challenges and Perspectives. *J. Mater. Chem. A* **2017**, *5* (36), 18919–18932. https://doi.org/10.1039/C7TA05121B.
(20) Ludi, A.; Güdel, H. U.; Müller, A.; Diemann, E.; Jørgensen, C. K.; Hathaway, B. J.; Schäffer, C. E.; Magyar, B.; Müller, U. *Inorganic Chemistry*; Structure and Bonding; Springer-Verlag: Berlin Heidelberg, 1973. https://doi.org/10.1007/BFb0016868.
(21) Herren, F.; Fischer, P.; Ludi, A.; Haelg, W. Neutron Diffraction Study of Prussian Blue, Fe4[Fe(CN)6]3.XH2O. Location of Water Molecules and Long-Range Magnetic Order. *Inorg. Chem.* **1980**, *19* (4), 956–959. https://doi.org/10.1021/ic50206a032.
(22) de Tacconi, N. R.; Rajeshwar, K.; Lezna, R. O. Metal Hexacyanoferrates: Electrosynthesis, in Situ Characterization, and Applications. *Chem. Mater.* **2003**, *15* (16), 3046–3062. https://doi.org/10.1021/cm0341540.

(23) Berrettoni, M.; Giorgetti, M.; Zamponi, S.; Conti, P.; Ranganathan, D.; Zanotto, A.; Saladino, M. L.; Caponetti, E. Synthesis and Characterization of Nanostructured Cobalt Hexacyanoferrate. *J. Phys. Chem. C* **2010**, *114* (14), 6401–6407. https://doi.org/10.1021/jp100367p.
(24) Ayers, J. B.; Waggoner, W. H. Synthesis and Properties of Two Series of Heavy Metal Hexacyanoferrates. *J. Inorg. Nucl. Chem.* **1971**, *33* (3), 721–733. https://doi.org/10.1016/0022-1902(71)80470-0.
(25) Itaya, K.; Ataka, T.; Toshima, S. Electrochemical Preparation of a Prussian Blue Analog: Iron-Ruthenium Cyanide. *J. Am. Chem. Soc.* **1982**, *104* (13), 3751–3752. https://doi.org/10.1021/ja00377a048.
(26) Itaya, K.; Akahoshi, H.; Toshima, S. Electrochemistry of Prussian Blue Modified Electrodes: An Electrochemical Preparation Method. *J. Electrochem. Soc.* **1982**, *129* (7), 1498. https://doi.org/10.1149/1.2124191.
(27) Kellawi, H.; Rosseinsky, D. R. Electrochemical Bichromic Behaviour of Ferric Ferrocyanide (Prussian Blue) in Thin Film Redox Processes. *J. Electroanal. Chem. Interfacial Electrochem.* **1982**, *131*, 373–376. https://doi.org/10.1016/0022-0728(82)87089-7.
(28) Ismail, I. M.; El-Sourougy, M. R.; Moneim, N. A.; Aly, H. F. Preparation, Characterization, and Utilization of Potassium Nickel Hexacyanoferrate for the Separation of Cesium and Cobalt from Contaminated Waste Water. *J. Radioanal. Nucl. Chem.* **1998**, *237* (1), 97–103. https://doi.org/10.1007/BF02386669.
(29) Ayrault, S.; Loss-Neskovic, C.; Fedoroff, M.; Garnier, E. Copper Hexacyanoferrates: Preparation, Composition and Structure. *Talanta* **1994**, *41* (9), 1435–1452. https://doi.org/10.1016/0039-9140(94)E0022-J.
(30) Lehto, J.; Haukka, S.; Harjula, R.; Blomberg, M. Mechanism of Caesium Ion Exchange on Potassium Cobalt Hexacyanoferrates(II). *J. Chem. Soc. Dalton Trans.* **1990**, No. 3, 1007–1011. https://doi.org/10.1039/DT9900001007.
(31) Vincent, T.; Vincent, C.; Guibal, E. Immobilization of Metal Hexacyanoferrate Ion-Exchangers for the Synthesis of Metal Ion Sorbents—A Mini-Review. *Molecules* **2015**, *20* (11), 20582–20613. https://doi.org/10.3390/molecules201119718.
(32) Giorgetti, M.; Guadagnini, L.; Tonelli, D.; Minicucci, M.; Aquilanti, G. Structural Characterization of Electrodeposited Copper Hexacyanoferrate Films by Using a Spectroscopic Multi-Technique Approach. *Phys. Chem. Chem. Phys.* **2012**, *14* (16), 5527–5537. https://doi.org/10.1039/C2CP24109A.
(33) Ciabocco, M.; Berrettoni, M.; Zamponi, S.; Cox, J. A.; Marini, S. Electrochemical Behavior of Inhcf in Alkali Metal Electrolytes. *J. Solid State Electrochem.* **2013**, *17* (9), 2445–2452. https://doi.org/10.1007/s10008-013-2123-2.
(34) Siperko, L. M.; Kuwana, T. Electrochemical and Spectroscopic Studies of Metal Hexacyanometalate Films: I . Cupric Hexacyanoferrate. *J. Electrochem. Soc.* **1983**, *130* (2), 396. https://doi.org/10.1149/1.2119718.
(35) Bocarsly, A. B.; Sinha, S. Chemically-Derivatized Nickel Surfaces: Synthesis of a New Class of Stable Electrode Interfaces. *J. Electroanal. Chem. Interfacial Electrochem.* **1982**, *137* (1), 157–162. https://doi.org/10.1016/0022-0728(82)85075-4.
(36) Schumacher, R. The Quartz Microbalance: A Novel Approach to the In-Situ Investigation of Interfacial Phenomena at the Solid/Liquid Junction [New Analytical Methods (40)]. *Angew. Chem. Int. Ed. Engl.* **1990**, *29* (4), 329–343. https://doi.org/10.1002/anie.199003293.
(37) Buttry, D. A.; Ward, M. D. Measurement of Interfaclal Processes at Electrode Surfaces with the Electrochemical Quartz Crystal Microbalance. *Chem. Rev.* **1992**, *92* (6), 1355–1379. https://doi.org/10.1021/cr00014a006.
(38) de Tacconi*, N. R.; Rajeshwar*, K.; Lezna, R. O. Photoelectrochemistry of Indium Hexacyanoferrate–Titania Composite Films. *J. Electroanal. Chem.* **2001**, *500* (1), 270–278. https://doi.org/10.1016/S0022-0728(00)00315-6.
(39) Matos-Peralta, Y.; Antuch, M. Review—Prussian Blue and Its Analogs as Appealing Materials for Electrochemical Sensing and Biosensing. *J. Electrochem. Soc.* **2019**, *167* (3), 037510. https://doi.org/10.1149/2.0102003JES.
(40) Itaya, K.; Ataka, T.; Toshima, S. Spectroelectrochemistry and Electrochemical Preparation Method of Prussian Blue Modified Electrodes. *J. Am. Chem. Soc.* **1982**, *104* (18), 4767–4772. https://doi.org/10.1021/ja00382a006.
(41) Isfahani, V. B.; Memarian, N.; Dizaji, H. R.; Arab, A.; Silva, M. M. The Physical and Electrochromic Properties of Prussian Blue Thin Films Electrodeposited on ITO Electrodes. *Electrochimica Acta* **2019**, *304*, 282–291. https://doi.org/10.1016/j.electacta.2019.02.120.
(42) Lundgren, C. A.; Murray, R. W. Observations on the Composition of Prussian Blue Films and Their Electrochemistry. *Inorg. Chem.* **1988**, *27* (5), 933–939. https://doi.org/10.1021/ic00278a036.
(43) Giménez-Romero, D.; Agrisuelas, J.; García-Jareño, J. J.; Gregori, J.; Gabrielli, C.; Perrot, H.; Vicente, F. Electromechanical Phase Transition in Hexacyanometallate Nanostructure (Prussian Blue). *J. Am. Chem. Soc.* **2007**, *129* (22), 7121–7126. https://doi.org/10.1021/ja070895g.
(44) Yamamoto, T.; Umemura, Y.; Sato, O.; Einaga, Y. Observation of the Anisotropic Photoinduced Magnetization Effect in Co−Fe Prussian Blue Thin Films Fabricated by Using Clay Langmuir−Blodgett Films as a Template. *J. Am. Chem. Soc.* **2005**, *127* (46), 16065–16073. https://doi.org/10.1021/ja053131e.
(45) Champion, G.; Escax, V.; Cartier dit Moulin, C.; Bleuzen, A.; Villain, F.; Baudelet, F.; Dartyge, E.; Verdaguer, M. Photoinduced Ferrimagnetic Systems in Prussian Blue Analogues CIxCo4[Fe(CN)6]y (CI = Alkali Cation). 4. Characterization of the Ferrimagnetism of the Photoinduced Metastable State in Rb1.8Co4[Fe(CN)6]3.3·13H2O by K Edges X-Ray Magnetic Circular Dichroism. *J. Am. Chem. Soc.* **2001**, *123* (50), 12544–12546. https://doi.org/10.1021/ja011297j.
(46) Sato, O.; Iyoda, T.; Fujishima, A.; Hashimoto, K. Electrochemically Tunable Magnetic Phase Transition in a High-Tc Chromium Cyanide Thin Film. *Science* **1996**, *271* (5245), 49–51. https://doi.org/10.1126/science.271.5245.49.
(47) Sato, O.; Kawakami, T.; Kimura, M.; Hishiya, S.; Kubo, S.; Einaga, Y. Electric-Field-Induced Conductance Switching in FeCo Prussian Blue Analogues. *J. Am. Chem. Soc.* **2004**, *126* (41), 13176–13177. https://doi.org/10.1021/ja046329s.
(48) Sato, O.; Iyoda, T.; Fujishima, A.; Hashimoto, K. Photoinduced Magnetization of a Cobalt-Iron Cyanide. *Science* **1996**, *272* (5262), 704–705. https://doi.org/10.1126/science.272.5262.704.
(49) Giménez-Romero, D.; Bueno, P. R.; Gabrielli, C.; García-Jareño, J. J.; Perrot, H.; Vicente, F. Kinetic Aspects of Ion Exchange in KhFek[Fe(CN)6]L·mH2O Compounds: A Combined Electrical

and Mass Transfer Functions Approach. *J. Phys. Chem. B* **2006**, *110* (39), 19352–19363. https://doi.org/10.1021/jp061533i.
(50) Bueno, P. R.; Giménez-Romero, D.; Gabrielli, C.; García-Jareño, J. J.; Perrot, H.; Vicente, F. Changeover during in Situ Compositional Modulation of Hexacyanoferrate (Prussian Blue) Material. *J. Am. Chem. Soc.* **2006**, *128* (51), 17146–17152. https://doi.org/10.1021/ja066982a.
(51) Tokoro, H.; Ohkoshi, S. Novel Magnetic Functionalities of Prussian Blue Analogs. *Dalton Trans.* **2011**, *40* (26), 6825–6833. https://doi.org/10.1039/C0DT01829E.
(52) Zhang, H.; Li, C.; Chen, D.; Zhao, J.; Jiao, X.; Xia, Y. Facile Preparation of Prussian Blue Analogue Co 3 [Co(CN) 6] 2 with Fine-Tuning Color Transition Temperature as Thermochromic Material. *CrystEngComm* **2017**, *19* (15), 2057–2064. https://doi.org/10.1039/C7CE00384F.
(53) Kulesza, P. J.; Malik, M. A.; Miecznikowski, K.; Wolkiewicz, A.; Zamponi, S.; Berrettoni, M.; Marassi, R. Countercation-Sensitive Electrochromism of Cobalt Hexacyanoferrate Films. *J. Electrochem. Soc.* **1996**, *143* (1), L10. https://doi.org/10.1149/1.1836374.
(54) Tandon, P. K.; Mehrotra, A.; Singh, A. K.; Baboo, R.; Dwivedi, P. B. Cocatalysis by Ruthenium(III) in Hydrogen Ions Catalyzed Oxidation of Iodide Ions: A Kinetic Study. *Int. J. Chem. Kinet.* **2004**, *36* (10), 545–553. https://doi.org/10.1002/kin.20030.
(55) Naik, R. M.; Srivastava, A.; Verma, A. K. The Kinetics and Mechanism of Ruthenium(III)-Catalyzed Oxidation of Tris(2-Amino Ethyl)Amine by Hexacyanoferrate(III) in Aqueous Alkaline Medium. *Turk. J. Chem.* **2008**, *32* (4), 495–503.
(56) Goel, A.; Sharma, S. Mechanistic Study of the Oxidation of L-Phenylalanine by Hexacyanoferrate(III) Catalyzed by Iridium(III) in Aqueous Alkaline Medium. *Transit. Met. Chem.* **2010**, *35* (5), 549–554. https://doi.org/10.1007/s11243-010-9362-1.
(57) Sharanabasamma, K.; Angadi, M. A.; Salunke, M. S.; Tuwar, S. M. Osmium(VIII) Catalyzed Oxidative Cleavage of Pyrrolidine Ring in l-Proline by Hexacyanoferrate(III) in Alkaline Media. *Ind. Eng. Chem. Res.* **2009**, *48* (23), 10381–10386. https://doi.org/10.1021/ie901049p.
(58) Shankaran, D. R.; Narayanan, S. S. Characterization and Application of an Electrode Modified by Mechanically Immobilized Copper Hexacyanoferrate. *Fresenius J. Anal. Chem.* **1999**, *364* (8), 686–689. https://doi.org/10.1007/s002160051414.
(59) Chen, S.-M.; Chan, C.-M. Preparation, Characterization, and Electrocatalytic Properties of Copper Hexacyanoferrate Film and Bilayer Film Modified Electrodes. *J. Electroanal. Chem.* **2003**, *543* (2), 161–173. https://doi.org/10.1016/S0022-0728(03)00017-2.
(60) Shankaran, D. D.; Narayanan, S. S. Mechanically Immobilized Copper Hexacyanoferrate Modified Electrode for Electrocatalysis Amperometric Determination of Glutathione. *Bull. Korean Chem. Soc.* **2001**, *22* (8), 816–820.
(61) Giorgetti, M.; Tonelli, D.; Berrettoni, M.; Aquilanti, G.; Minicucci, M. Copper Hexacyanoferrate Modified Electrodes for Hydrogen Peroxide Detection as Studied by X-Ray Absorption Spectroscopy. *J. Solid State Electrochem.* **2014**, *4* (18), 965–973. https://doi.org/10.1007/s10008-013-2343-5.
(62) Cai, C.-X.; Xue, K.-H.; Xu, S.-M. Electrocatalytic Activity of a Cobalt Hexacyanoferrate Modified Glassy Carbon Electrode toward Ascorbic Acid Oxidation. *J. Electroanal. Chem.* **2000**, *486* (2), 111–118. https://doi.org/10.1016/S0022-0728(00)00114-5.
(63) Huang, K.; Yu, S.; Wang, L.; Gan, T.; Li, M. Simultaneous Determination of Hydroquinone, Catechol and Resorcinol Based on Graphene/Cobalt Hexacyanoferrate Modified Glassy Carbon Electrode. *Acta Chim. Sin.* **2012**, *70* (06), 735. https://doi.org/10.6023/A1110282.
(64) Cai, C.-X.; Ju, H.-X.; Chen, H.-Y. Cobalt Hexacyanoferrate Modified Microband Gold Electrode and Its Electrocatalytic Activity for Oxidation of NADH. *J. Electroanal. Chem.* **1995**, *397* (1), 185–190. https://doi.org/10.1016/0022-0728(95)04169-6.
(65) Xun, Z.; Cai, C.; Xing, W.; Lu, T. Electrocatalytic Oxidation of Dopamine at a Cobalt Hexacyanoferrate Modified Glassy Carbon Electrode Prepared by a New Method. *J. Electroanal. Chem.* **2003**, *545*, 19–27. https://doi.org/10.1016/S0022-0728(03)00062-7.
(66) Luo, X.; Pan, J.; Pan, K.; Yu, Y.; Zhong, A.; Wei, S.; Li, J.; Shi, J.; Li, X. An Electrochemical Sensor for Hydrazine and Nitrite Based on Graphene–Cobalt Hexacyanoferrate Nanocomposite: Toward Environment and Food Detection. *J. Electroanal. Chem.* **2015**, *745*, 80–87. https://doi.org/10.1016/j.jelechem.2015.03.017.
(67) Wang, Y.; Rui, Y.; Li, F.; Li, M. Electrodeposition of Nickel Hexacyanoferrate/Layered Double Hydroxide Hybrid Film on the Gold Electrode and Its Application in the Electroanalysis of Ascorbic Acid. *Electrochimica Acta* **2014**, *117*, 398–404. https://doi.org/10.1016/j.electacta.2013.11.141.
(68) Zhou, D.-M.; Ju, H.-X.; Chen, H.-Y. Catalytic Oxidation of Dopamine at a Microdisk Platinum Electrode Modified by Electrodeposition of Nickel Hexacyanoferrate and Nafion®. *J. Electroanal. Chem.* **1996**, *408* (1), 219–223. https://doi.org/10.1016/0022-0728(95)04522-8.
(69) Richard Prabakar, S. J.; Sriman Narayanan, S. Amperometric Determination of Hydrazine Using a Surface Modified Nickel Hexacyanoferrate Graphite Electrode Fabricated Following a New Approach. *J. Electroanal. Chem.* **2008**, *617* (2), 111–120. https://doi.org/10.1016/j.jelechem.2008.01.020.
(70) Tseng, K.-S.; Chen, L.-C.; Ho, K.-C. Amperometric Detection of Cysteine at an In3+ Stabilized Indium Hexacyanoferrate Modified Electrode. *Electroanalysis* **2006**, *18* (13–14), 1306–1312. https://doi.org/10.1002/elan.200603531.
(71) Garjonyt≒, R.; Malinauskas, A. Electrocatalytic Reactions of Hydrogen Peroxide at Carbon Paste Electrodes Modified by Some Metal Hexacyanoferrates. *Sens. Actuators B Chem.* **1998**, *46* (3), 236–241. https://doi.org/10.1016/S0925-4005(98)00123-3.
(72) Prout, W. E.; Russell, E. R.; Groh, H. J. Ion Exchange Absorption of Cesium by Potassium Hexacyanocobalt (II) Ferrate (II). *J. Inorg. Nucl. Chem.* **1965**, *27* (2), 473–479. https://doi.org/10.1016/0022-1902(65)80367-0.
(73) Lee, H.-W.; Wang, R. Y.; Pasta, M.; Woo Lee, S.; Liu, N.; Cui, Y. Manganese Hexacyanomanganate Open Framework as a High-Capacity Positive Electrode Material for Sodium-Ion Batteries. *Nat. Commun.* **2014**, *5* (1), 5280. https://doi.org/10.1038/ncomms6280.
(74) Ling, C.; Chen, J.; Mizuno, F. First-Principles Study of Alkali and Alkaline Earth Ion Intercalation in Iron Hexacyanoferrate: The Important Role of Ionic Radius. *J. Phys. Chem. C* **2013**, *117* (41), 21158–21165. https://doi.org/10.1021/jp4078689.
(75) Chen, S.-M.; Chan, C.-M. Preparation, Characterization, and Electrocatalytic Properties of Copper Hexacyanoferrate Film and Bilayer Film Modified Electrodes. *J. Electroanal. Chem.* **2003**, *543* (2), 161–173. https://doi.org/10.1016/S0022-0728(03)00017-2.
(76) Rutkowska, I. A.; Stroka, J.; Galus, Z. Electrochemical Properties of Modified Copper–Thallium Hexacyanoferrate Electrode in the Presence of Different Univalent Cations. *Electrochimica Acta* **2008**, *53* (11), 3870–3878. https://doi.org/10.1016/j.electacta.2007.12.042.

(77) Bárcena Soto, M.; Scholz, F. The Thermodynamics of the Insertion Electrochemistry of Solid Metal Hexacyanometallates. *J. Electroanal. Chem.* **2002**, *521* (1), 183–189. https://doi.org/10.1016/S0022-0728(02)00710-6.
(78) Scholz, F.; Doménech-Carbó, A. The Thermodynamics of Insertion Electrochemical Electrodes—A Team Play of Electrons and Ions across Two Separate Interfaces. *Angew. Chem. Int. Ed.* **2019**, *58* (11), 3279–3284. https://doi.org/10.1002/anie.201809631.
(79) Ayrault, S.; Jimenez, B.; Garnier, E.; Fedoroff, M.; Jones, D. J.; Loos-Neskovic, C. Sorption Mechanisms of Cesium on CuII2FeII(CN)6and CuII3[FeIII(CN)6]2Hexacyanoferrates and Their Relation to the Crystalline Structure. *J. Solid State Chem.* **1998**, *141* (2), 475–485. https://doi.org/10.1006/jssc.1998.7997.
(80) Ayrault, S.; Loos-Neskovic, C.; Fedoroff, M.; Garnier, E.; Jones, D. J. Compositions and Structures of Copper Hexacyanoferrates(II) and (III): Experimental Results. *Talanta* **1995**, *42* (11), 1581–1593. https://doi.org/10.1016/0039-9140(95)01611-2.
(81) Vincent, T.; Vincent, C.; Barré, Y.; Guari, Y.; Saout, G. L.; Guibal, E. Immobilization of Metal Hexacyanoferrates in Chitin Beads for Cesium Sorption: Synthesis and Characterization. *J. Mater. Chem. A* **2014**, *2* (26), 10007–10021. https://doi.org/10.1039/C4TA01128G.
(82) de Tacconi, N. R.; Rajeshwar, K.; Lezna, R. O. Metal Hexacyanoferrates: Electrosynthesis, in Situ Characterization, and Applications. *Chem. Mater.* **2003**, *15* (16), 3046–3062. https://doi.org/10.1021/cm0341540.
(83) Grandjean, A.; Delchet, C.; Causse, J.; Barré, Y.; Guari, Y.; Larionova, J. Effect of the Chemical Nature of Different Transition Metal Ferrocyanides to Entrap Cs. *J. Radioanal. Nucl. Chem.* **2016**, *307* (1), 427–436. https://doi.org/10.1007/s10967-015-4098-1.
(84) Ciabocco, M.; Berrettoni, M.; Zamponi, Silvia. An Overview on the Facile and Reversible Cations Intercalation in Nickel-Hexacyanoferrate Open Framework. *Int. J. Electrochem. Sci.* **2018**, 5535–5551. https://doi.org/10.20964/2018.06.37.
(85) D, D.; Z, L.; Y, Y.; C, F.; Z, Z. Selective Removal of Cesium from Aqueous Solutions with Nickel (II) Hexacyanoferrate (III) Functionalized Agricultural Residue-Walnut Shell. *J. Hazard. Mater.* **2014**, *270*, 187–195. https://doi.org/10.1016/j.jhazmat.2014.01.056.
(86) Kazemian, H.; Zakeri, H.; Rabbani, M. S. Csand Sr Removal from Solution Using Potassium Nickel Hexacyanoferrateimpregnated Zeolites. *J. Radioanal. Nucl. Chem.* **2006**, *268* (2), 231–236. https://doi.org/10.1007/s10967-006-0158-x.
(87) Mostafa, M.; El-Absy, M. A.; Amin, M.; El-Amir, M. A.; Farag, A. B. Partial Purification of Neutron-Activation 99Mo from Cross-Contaminant Radionuclides onto Potassium Nickel Hexacyanoferrate(II) Column. *J. Radioanal. Nucl. Chem.* **2010**, *285* (3), 579–588. https://doi.org/10.1007/s10967-010-0584-7.
(88) Kołodyńska, D. D.; Hubicki, Z.; Kubica, B. Hexacyanoferrate Composite Sorbent in Removal of Anionic Species From Waters and Waste Waters. *Sep. Sci. Technol.* **2012**, *47* (9), 1361–1368. https://doi.org/10.1080/01496395.2012.672525.
(89) Sheha, R. R. Preparation and Performance of a Novel Composite as a Reactive Resin for Copper Retention. *Chem. Eng. J.* **2012**, *213*, 163–174. https://doi.org/10.1016/j.cej.2012.09.113.
(90) Chen, R.; Tanaka, H.; Kawamoto, T.; Asai, M.; Fukushima, C.; Kurihara, M.; Ishizaki, M.; Watanabe, M.; Arisaka, M.; Nankawa, T. Thermodynamics and Mechanism Studies on Electrochemical Removal of Cesium Ions from Aqueous Solution Using a Nanoparticle Film of Copper Hexacyanoferrate. *ACS Appl. Mater. Interfaces* **2013**, *5* (24), 12984–12990. https://doi.org/10.1021/am403748b.
(91) Chen, R.; Tanaka, H.; Kawamoto, T.; Asai, M.; Fukushima, C.; Na, H.; Kurihara, M.; Watanabe, M.; Arisaka, M.; Nankawa, T. Selective Removal of Cesium Ions from Wastewater Using Copper Hexacyanoferrate Nanofilms in an Electrochemical System. *Electrochimica Acta* **2013**, *87*, 119–125. https://doi.org/10.1016/j.electacta.2012.08.124.
(92) Ramaswamy, M. Sorption of Cesium by Hexacyanoferrate Composites from Neutral and Acidic Media. *Solvent Extr. Ion Exch.* **1997**, *15* (6), 1119–1131. https://doi.org/10.1080/07366299708934525.
(93) Rykov, A. I.; Wang, J.; Zhang, T.; Nomura, K. Cs Sorption by "Soluble" and "Insoluble" Iron Hexacyanocobaltates Probed by Mössbauer Spectroscopy. *Hyperfine Interact.* **2013**, *218* (1), 53–58. https://doi.org/10.1007/s10751-012-0705-5.
(94) Loos-Neskovic, C.; Fedoroff, M. Fixation Mechanisms of Cesium on Nickel and Zinc Ferrocyanides. *Solvent Extr. Ion Exch.* **1989**, *7* (1), 131–158. https://doi.org/10.1080/07360298908962302.
(95) Sheha, R. R. Synthesis and Characterization of Magnetic Hexacyanoferrate (II) Polymeric Nanocomposite for Separation of Cesium from Radioactive Waste Solutions. *J. Colloid Interface Sci.* **2012**, *388* (1), 21–30. https://doi.org/10.1016/j.jcis.2012.08.042.
(96) Volkov, A. G.; Paula, S.; Deamer, D. W. Two Mechanisms of Permeation of Small Neutral Molecules and Hydrated Ions across Phospholipid Bilayers. *Bioelectrochem. Bioenerg.* **1997**, *42* (2), 153–160. https://doi.org/10.1016/S0302-4598(96)05097-0.
(97) Qing, Y.; Li, J.; Kang, B.; Chang, S.; Dai, Y.; Long, Q.; Yuan, C. Selective Sorption Mechanism of Cs+ on Potassium Nickel Hexacyanoferrate(II) Compounds. *J. Radioanal. Nucl. Chem.* **2015**, *304* (2), 527–533. https://doi.org/10.1007/s10967-014-3876-5.
(98) Faustino, P. J.; Yang, Y.; Progar, J. J.; Brownell, C. R.; Sadrieh, N.; May, J. C.; Leutzinger, E.; Place, D. A.; Duffy, E. P.; Houn, F.; Loewke, S. A.; Mecozzi, V. J.; Ellison, C. D.; Khan, M. A.; Hussain, A. S.; Lyon, R. C. Quantitative Determination of Cesium Binding to Ferric Hexacyanoferrate: Prussian Blue. *J. Pharm. Biomed. Anal.* **2008**, *47* (1), 114–125. https://doi.org/10.1016/j.jpba.2007.11.049.
(99) Wessells, C. D.; Huggins, R. A.; Cui, Y. Copper Hexacyanoferrate Battery Electrodes with Long Cycle Life and High Power. *Nat. Commun.* **2011**, *2* (1), 550. https://doi.org/10.1038/ncomms1563.
(100) Wessells, C. D.; Peddada, S. V.; Huggins, R. A.; Cui, Y. Nickel Hexacyanoferrate Nanoparticle Electrodes For Aqueous Sodium and Potassium Ion Batteries. *Nano Lett.* **2011**, *11* (12), 5421–5425. https://doi.org/10.1021/nl203193q.
(101) Wang, L.; Lu, Y.; Liu, J.; Xu, M.; Cheng, J.; Zhang, D.; Goodenough, J. B. A Superior Low-Cost Cathode for a Na-Ion Battery. *Angew. Chem.* **2013**, *125* (7), 2018–2021. https://doi.org/10.1002/ange.201206854.
(102) Wang, R. Y.; Wessells, C. D.; Huggins, R. A.; Cui, Y. Highly Reversible Open Framework Nanoscale Electrodes for Divalent Ion Batteries. *Nano Lett.* **2013**, *13* (11), 5748–5752. https://doi.org/10.1021/nl403669a.
(103) Mizuno, Y.; Okubo, M.; Hosono, E.; Kudo, T.; Zhou, H.; Oh-ishi, K. Suppressed Activation Energy for Interfacial Charge Transfer of a Prussian Blue Analog Thin Film Electrode with

Hydrated Ions (Li+, Na+, and Mg2+). *J. Phys. Chem. C* **2013**, *117* (21), 10877–10882. https://doi.org/10.1021/jp311616s.
(104) Wang, R. Y.; Shyam, B.; Stone, K. H.; Weker, J. N.; Pasta, M.; Lee, H.-W.; Toney, M. F.; Cui, Y. Reversible Multivalent (Monovalent, Divalent, Trivalent) Ion Insertion in Open Framework Materials. *Adv. Energy Mater.* **2015**, *5* (12), 1401869. https://doi.org/10.1002/aenm.201401869.
(105) Huggins, R. A. Review—A New Class of High Rate, Long Cycle Life, Aqueous Electrolyte Battery Electrodes. *J. Electrochem. Soc.* **2017**, *164* (1), A5031–A5036. https://doi.org/10.1149/2.0571701jes.
(106) Honda, K.; Hayashi, H. Prussian Blue Containing Nafion Composite Film as Rechargeable Battery. *J. Electrochem. Soc.* **1987**, *134* (6), 1330–1334. https://doi.org/10.1149/1.2100668.
(107) Ma, F.; Li, Q.; Wang, T.; Zhang, H.; Wu, G. Energy Storage Materials Derived from Prussian Blue Analogues. *Sci. Bull.* **2017**, *62* (5), 358–368. https://doi.org/10.1016/j.scib.2017.01.030.
(108) Jia, Z.; Wang, B.; Wang, Y. Copper Hexacyanoferrate with a Well-Defined Open Framework as a Positive Electrode for Aqueous Zinc Ion Batteries. *Mater. Chem. Phys.* **2015**, *149–150*, 601–606. https://doi.org/10.1016/j.matchemphys.2014.11.014.
(109) Zhang, L.; Chen, L.; Zhou, X.; Liu, Z. Morphology-Dependent Electrochemical Performance of Zinc Hexacyanoferrate Cathode for Zinc-Ion Battery. *Sci. Rep.* **2015**, *5* (1), 18263. https://doi.org/10.1038/srep18263.
(110) Padigi, P.; Kuperman, N.; Thiebes, J. J.; Goncher, G.; Evans, D.; Solanki, R. Calcium Cobalt Hexacyanoferrate Cathodes for Rechargeable Divalent Ion Batteries. *J. New Mater. Electrochem. Syst.* **2016**, *19* (2), 057–064. https://doi.org/10.14447/jnmes.v19i2.231.
(111) Lilga, M. A.; Orth, R. J.; Sukamto, J. P. H. *Electrically Switched Cesium Ion Exchange. FY 1997 Annual Report*; PNNL-11766; Pacific Northwest National Lab. (PNNL), Richland, WA (United States), 1997. https://doi.org/10.2172/565622.
(112) Lilga, M. A.; Orth, R. J.; Sukamto, J. P. H.; Haight, S. M.; Schwartz, D. T. Metal Ion Separations Using Electrically Switched Ion Exchange. *Sep. Purif. Technol.* **1997**, *11* (3), 147–158. https://doi.org/10.1016/S1383-5866(97)00017-8.
(113) Sun, B.; Hao, X.-G.; Wang, Z.-D.; Guan, G.-Q.; Zhang, Z.-L.; Li, Y.-B.; Liu, S.-B. Separation of Low Concentration of Cesium Ion from Wastewater by Electrochemically Switched Ion Exchange Method: Experimental Adsorption Kinetics Analysis. *J. Hazard. Mater.* **2012**, *233–234*, 177–183. https://doi.org/10.1016/j.jhazmat.2012.07.010.
(114) Lilga, M. A.; Orth, R. J.; Sukamto, J. P. H.; Rassat, S. D.; Genders, J. D.; Gopal, R. Cesium Separation Using Electrically Switched Ion Exchange. *Sep. Purif. Technol.* **2001**, *24* (3), 451–466. https://doi.org/10.1016/S1383-5866(01)00145-9.
(115) Wang, Z.; Tian, S.; Niu, J.; Kong, W.; Lin, J.; Hao, X.; Guan, G. An Electrochemically Switched Ion Exchange Process with Self-Electrical-Energy Recuperation for Desalination. *Sep. Purif. Technol.* **2020**, *239*, 116521. https://doi.org/10.1016/j.seppur.2020.116521.
(116) Hillman, A. R.; Pickup, P.; Seeber, R.; Skompska, M.; Vorotyntsev, M. A. Electrochemistry of Electroactive Materials. *Electrochimica Acta* **2014**, *122*, 1–2. https://doi.org/10.1016/j.electacta.2014.01.001.
(117) Long, Y.-Z.; Li, M.-M.; Gu, C.; Wan, M.; Duvail, J.-L.; Liu, Z.; Fan, Z. Recent Advances in Synthesis, Physical Properties and Applications of Conducting Polymer Nanotubes and Nanofibers. *Prog. Polym. Sci.* **2011**, *36* (10), 1415–1442. https://doi.org/10.1016/j.progpolymsci.2011.04.001.
(118) Shi, Y.; Peng, L.; Ding, Y.; Zhao, Y.; Yu, G. Nanostructured Conductive Polymers for Advanced Energy Storage. *Chem. Soc. Rev.* **2015**, *44* (19), 6684–6696. https://doi.org/10.1039/C5CS00362H.
(119) Bruckenstein, S.; Chen, J.; Jureviciute, I.; Hillman, A. R. Ion and solvent transfers accompanying redox switching of polypyrrole films immersed in divalent anion solutions. *Electrochimica Acta* **2009**, *54* (13), 3516–3525.
(120) Hillman, A. R.; Mohamoud, M. A. Ion, Solvent and Polymer Dynamics in Polyaniline Conducting Polymer Films. *Electrochimica Acta* **2006**, *51* (27), 6018–6024. https://doi.org/10.1016/j.electacta.2005.11.054.
(121) Seh, Z. W.; Wang, H.; Hsu, P.-C.; Zhang, Q.; Li, W.; Zheng, G.; Yao, H.; Cui, Y. Facile Synthesis of Li2S–Polypyrrole Composite Structures for High-Performance Li2S Cathodes. *Energy Environ. Sci.* **2014**, *7* (2), 672. https://doi.org/10.1039/c3ee43395a.
(122) Peng, X.; Peng, L.; Wu, C.; Xie, Y. Two Dimensional Nanomaterials for Flexible Supercapacitors. *Chem. Soc. Rev.* **2014**, *43* (10), 3303. https://doi.org/10.1039/c3cs60407a.
(123) Hangarter, C. M.; Chartuprayoon, N.; Hernández, S. C.; Choa, Y.; Myung, N. V. Hybridized Conducting Polymer Chemiresistive Nano-Sensors. *Nano Today* **2013**, *8* (1), 39–55. https://doi.org/10.1016/j.nantod.2012.12.005.
(124) Ćirić-Marjanović, G. Recent Advances in Polyaniline Research: Polymerization Mechanisms, Structural Aspects, Properties and Applications. *Synth. Met.* **2013**, *177*, 1–47. https://doi.org/10.1016/j.synthmet.2013.06.004.
(125) Wang, G.; Zhang, L.; Zhang, J. A Review of Electrode Materials for Electrochemical Supercapacitors. *Chem Soc Rev* **2012**, *41* (2), 797–828. https://doi.org/10.1039/C1CS15060J.
(126) Lu, X.; Yu, M.; Wang, G.; Tong, Y.; Li, Y. Flexible Solid-State Supercapacitors: Design, Fabrication and Applications. *Energy Environ. Sci.* **2014**, *7* (7), 2160. https://doi.org/10.1039/c4ee00960f.
(127) Ronkainen, N. J.; Halsall, H. B.; Heineman, W. R. Electrochemical Biosensors. *Chem. Soc. Rev.* **2010**, *39* (5), 1747. https://doi.org/10.1039/b714449k.
(128) Du, X.; Hao, X.; Wang, Z.; Guan, G. Electroactive Ion Exchange Materials: Current Status in Synthesis, Applications and Future Prospects. *J. Mater. Chem. A* **2016**, *4* (17), 6236–6258. https://doi.org/10.1039/C6TA01385F.
(129) Mullaliu, A.; Giorgetti, M. Metal Hexacyanoferrates: Ion Insertion (or Exchange) Capabilities. In *Applications of Ion Exchange Materials in the Environment*; Inamuddin, Ahamed, M. I., Asiri, A. M., Eds.; Springer International Publishing: Cham, 2019; pp 109–133. https://doi.org/10.1007/978-3-030-10430-6_6.
(130) Jayalakshmi, M.; Scholz, F. Performance Characteristics of Zinc Hexacyanoferrate/Prussian Blue and Copper Hexacyanoferrate/Prussian Blue Solid State Secondary Cells. *J. Power Sources* **2000**, *91* (2), 217–223. https://doi.org/10.1016/S0378-7753(00)00475-4.
(131) Ventura, M.; Mullaliu, A.; Ciurduc, D. E.; Zappoli, S.; Giuli, G.; Tonti, D.; Enciso, E.; Giorgetti, M. Thin Layer Films of Copper Hexacyanoferrate: Structure Identification and Analytical Applications. *J. Electroanal. Chem.* **2018**, *827*, 10–20. https://doi.org/10.1016/j.jelechem.2018.08.044.

(132) Yang, S.; Li, G.; Wang, G.; Zhao, J.; Hu, M.; Qu, L. A Novel Nonenzymatic H2O2 Sensor Based on Cobalt Hexacyanoferrate Nanoparticles and Graphene Composite Modified Electrode. *Sens. Actuators B Chem.* **2015**, *208*, 593–599. https://doi.org/10.1016/j.snb.2014.11.055.
(133) Itoi, M.; Jike, T.; Nishio-Hamane, D.; Udagawa, S.; Tsuda, T.; Kuwabata, S.; Boukheddaden, K.; Andrus, M. J.; Talham, D. R. Direct Observation of Short-Range Structural Coherence During a Charge Transfer Induced Spin Transition in a CoFe Prussian Blue Analogue by Transmission Electron Microscopy. *J. Am. Chem. Soc.* **2015**, *137* (46), 14686–14693. https://doi.org/10.1021/jacs.5b08242.
(134) Jassal, V.; Shanker, U.; Kaith, B. S.; Shankar, S. Green Synthesis of Potassium Zinc Hexacyanoferrate Nanocubes and Their Potential Application in Photocatalytic Degradation of Organic Dyes. *RSC Adv.* **2015**, *5* (33), 26141–26149. https://doi.org/10.1039/C5RA03266K.
(135) Sciacca, R.; Zamponi, S.; Berrettoni, M.; Giorgetti, M. Stable Films of Zinc-Hexacyanoferrate: Electrochemistry and Ion Insertion Capabilities. *J. Solid State Electrochem.* **2021**. https://doi.org/10.1007/s10008-021-05005-w.
(136) Song, J.; Wang, L.; Lu, Y.; Liu, J.; Guo, B.; Xiao, P.; Lee, J.-J.; Yang, X.-Q.; Henkelman, G.; Goodenough, J. B. Removal of Interstitial H2O in Hexacyanometallates for a Superior Cathode of a Sodium-Ion Battery. *J. Am. Chem. Soc.* **2015**, *137* (7), 2658–2664. https://doi.org/10.1021/ja512383b.
(137) Subramani, K.; Jeyakumar, D.; Sathish, M. Manganese Hexacyanoferrate Derived Mn3O4 Nanocubes–Reduced Graphene Oxide Nanocomposites and Their Charge Storage Characteristics in Supercapacitors. *Phys. Chem. Chem. Phys.* **2014**, *16* (10), 4952. https://doi.org/10.1039/c3cp54788d.
(138) Jiang, H.; Xu, Y.-T.; Wang, T.; Zhu, P.-L.; Yu, S.; Yu, Y.; Fu, X.-Z.; Sun, R.; Wong, C.-P. Nickel Hexacyanoferrate Flower-like Nanosheets Coated Three Dimensional Porous Nickel Films as Binder-Free Electrodes for Neutral Electrolyte Supercapacitors. *Electrochimica Acta* **2015**, *166*, 157–162. https://doi.org/10.1016/j.electacta.2015.03.089.
(139) Chen, W.; Xia, X. H. Highly Stable Nickel Hexacyanoferrate Nanotubes for Electrically Switched Ion Exchange. *Adv. Funct. Mater.* **2007**, *17* (15), 2943–2948. https://doi.org/10.1002/adfm.200700015.
(140) Hao, X.; Li, Y.; Pritzker, M. Pulsed Electrodeposition of Nickel Hexacyanoferrate Films for Electrochemically Switched Ion Exchange. *Sep. Purif. Technol.* **2008**, *63* (2), 407–414. https://doi.org/10.1016/j.seppur.2008.06.001.
(141) Fujita, H.; Sasano, H.; Miyajima, R.; Sakoda, A. Adsorption Equilibrium and Kinetics of Cesium onto Insoluble Prussian Blue Synthesized by an Immediate Precipitation Reaction between Fe3+ and [Fe(CN)6]4−. *Adsorption* **2014**, *20* (7), 905–915. https://doi.org/10.1007/s10450-014-9635-7.
(142) Delchet, C.; Tokarev, A.; Dumail, X.; Toquer, G.; Barré, Y.; Guari, Y.; Guerin, C.; Larionova, J.; Grandjean, A. Extraction of Radioactive Cesium Using Innovative Functionalized Porous Materials. *RSC Adv.* **2012**, *2* (13), 5707–5716. https://doi.org/10.1039/C2RA00012A.
(143) Singh, K.; Zhang, L.; Zuilhof, H.; de Smet, L. C. P. M. Water Desalination with Nickel Hexacyanoferrate Electrodes in Capacitive Deionization: Experiment, Model and Comparison with Carbon. *Desalination* **2020**, *496*, 114647. https://doi.org/10.1016/j.desal.2020.114647.
(144) Timofeev, V. V.; Levin, M. B.; Starikova, A. A.; Trofimov, M. A.; Korneev, S. M.; Mikhelson, K. N. Solid-Contact Ion-Selective Electrodes with Copper Hexacyanoferrate in the Transducer Layer. *Russ. J. Electrochem.* **2018**, *54* (4), 400–408. https://doi.org/10.1134/S1023193518040080.
(145) Liu, S.; Pan, G. L.; Li, G. R.; Gao, X. P. Copper Hexacyanoferrate Nanoparticles as Cathode Material for Aqueous Al-Ion Batteries. *J. Mater. Chem. A* **2015**, *3* (3), 959–962. https://doi.org/10.1039/C4TA04644G.
(146) Reed, L. D.; Ortiz, S. N.; Xiong, M.; Menke, E. J. A Rechargeable Aluminum-Ion Battery Utilizing a Copper Hexacyanoferrate Cathode in an Organic Electrolyte. *Chem. Commun.* **2015**, *51* (76), 14397–14400. https://doi.org/10.1039/C5CC06053B.
(147) Galván-Arzate, S.; Santamaría, A. Thallium Toxicity. *Toxicol. Lett.* **1998**, *99* (1), 1–13. https://doi.org/10.1016/S0378-4274(98)00126-X.
(148) Zhao, Z.; Xiong, Y.; Cheng, X.; Hou, X.; Yang, Y.; Tian, Y.; You, J.; Xu, L. Adsorptive Removal of Trace Thallium(I) from Wastewater: A Review and New Perspectives. *J. Hazard. Mater.* **2020**, *393*, 122378. https://doi.org/10.1016/j.jhazmat.2020.122378.
(149) Sangvanich, T.; Sukwarotwat, V.; Wiacek, R. J.; Grudzien, R. M.; Fryxell, G. E.; Addleman, R. S.; Timchalk, C.; Yantasee, W. Selective Capture of Cesium and Thallium from Natural Waters and Simulated Wastes with Copper Ferrocyanide Functionalized Mesoporous Silica. *J. Hazard. Mater.* **2010**, *182* (1), 225–231. https://doi.org/10.1016/j.jhazmat.2010.06.019.
(150) Zhang, N.; Kawamoto, T.; Jiang, Y.; Takahashi, A.; Ishizaki, M.; Asai, M.; Kurihara, M.; Zhang, Z.; Lei, Z.; Parajuli, D. Interpretation of the Role of Composition on the Inclusion Efficiency of Monovalent Cations into Cobalt Hexacyanoferrate. *Chem. – Eur. J.* **2019**, *25* (23), 5950–5958. https://doi.org/10.1002/chem.201900097.

Work aims

This work aims to obtain materials electrochemically, which show redox capabilities, easily identifiable through potentiostatic and potentiodynamic techniques. Specifically, these materials capability to be electrodeposited on conductive substrates, allows them to be characterized not only but electrochemical techniques but also though the most common spectroscopic techniques, such as XRD, ATR-FTIR, SEM, etc. A comparative discussion about the growth, characterization, and ionic sieves proprieties of the Cu, Ni, Co, Zn, In and Cr PB analogues is presented. In particular, Chapter 3 of this dissertation focuses on a facile approach to a stable modification of GCE by ZnHCF, obtaining a well-defined redox couple. Furthermore, ZnHCF was investigated in different support electrolytes (mono-, di- and trivalent cations), in order to highlight its capability as ionic sieve. In addition, ZnHCF powders were tested both as cathode for ZIBs and as standard for Zn/MnHCF batteries studies. Besides, Chapter 4 reports the electrochemical behaviour of different PBAs as sieves for REEs recovery, demonstrating their reversible insertion/de-insertion electrochemically controlled. Also, kinetic behaviour of NiHCF was demonstrated. This capability allows to use PBAs for different applications including wastewater treatment, batteries and element purification. Finally, the synthesis and characterization of green rust thin film is reported in the appendix section. In particular, the results obtained highlight that an iron oxy-hydroxides compound (Akaganèite) prefers to insert chloride ions, which is responsible of the corrosion progress. Thus, understanding the electrochemical reaction involved in the corrosion processes, is useful for the diagnosis and prevention of

artefacts. Also, VIMP technique allows to compare the controlled- electrodeposited green rust electrochemical behaviour with the real sample one.

Chapter 3

Zinc hexacyanoferrate as ESIX material

3.1 Introduction

In situ generation of thin film materials on a conductive substrate is a useful technique for the preparation of electrodes and electrochemical devices for many technological applications. For instance these methods allow steady films fabrication for ion sensors or ion sieves testing [1–3]. The advantage of the electrodeposition consists of the *in situ* functionalization of the electrode surface. This allows to tailor the thin film by controlling some experimental variables such as the applied potential, the precursors concentration, the supporting electrolytes [4, 5]. The surface modification could be achieved also by adsorption or via mechanical attachment. Metal hexacyanoferrates (MHCFs) or Prussian Blue analogues (MHCFs), are inorganic compounds which were successfully electroformed [6–8]. MHCFs thin films fabricated by electrodeposition were used for several applications such as electrocatalysis, energy storage and, above all for ion-sensing detection and exchange capability [9–12]. Their open structures, also called zeolitic-like, allow to intercalate and store alkali cations upon electrical charging, ensuring the electroneutrality of the compounds. So, they are the perfect candidates for the ion separation controlled by electrochemically switched ion exchange systems, which was reported for the first time by Lilga *et al*. [13]. The method explained the selective and reversible removal of Caesium using an electrode modified by Prussian blue analogue. Briefly, the potential was modulated and switched in polarity, forcing the oxidation/reduction of the thin film, which in turn caused the release or uptake of the alkali metal cation, as described by the Eq (1).

$$M[Fe^{III}(CN)_6]_x + yA^{n+} + ye^- \leftrightarrows A_yM[Fe^{II}(CN)_6]_x \quad (1)$$

Later on, other studies were carried out on the insertion/de-insertion involving mono, di and tri-valent cations, [14, 15] which, generally, influence the electrochemical behaviour of MHCFs [14, 16, 17]. In particular, their capability as sieves for pollutants like caesium, or for mixed aqueous electrolytes batteries, was widely reported [18–21].

Table 3.1 Cost and LD50 (rat, oral) of some metal chlorides. From reference [22]

	$BaCl_2$	**$CoCl_2$**	**$CuCl_2$**	**$MnCl_2$**	**$NiCl_2$**	**$SnCl_2$**	**$ZnCl_2$**
LD50 (mg kg^{-1})	118	80	584	1484	105	700	**350**
Price (€ kg^{-1})	45	1272	174	199	904	148	**122**

Cations are host in a given lattice site in MHCFs during the reduction reaction, while released during the oxidation step. The relative reduction and oxidation potential are closely related to both the hydration energy and the adsorption energy into the MHCF [23]. The transition metal of the MHCF material also influences their ability as ionic sieve [24, 25]. Additional key aspect refers to the abundance of the metal and safety concerns. Among MHCFs, zinc, manganese and iron analogues are characterized by low toxicity and low cost, therefore making them promising systems for development in several industrial applications [26, 27]. In particular, zinc hexacyanoferrate (ZnHCF) is one of the MHCFs used in aqueous ion battery improvement, thanks to its very high operating potential [28]. As shown in Table 1, the precursor salt $ZnCl_2$ has a LD50 of 350 mg/kg, and is relatively cheap while compared to other transition metal chloride salts [22]. LD50, lethal dose or median lethal dose, is defined as the amount of a toxic agent lethal to the 50% of the experimental animals exposed to it. However, although procedures

for the deposition of zinc hexacyanoferrate film are available, there is a lack of deposition protocol on the common electrode support (Glassy Carbon electrode) [29]. For instance, Fenga and Stradiotto suggest a controlled electrodeposit procedure of ZnHCF on piezoelectric quartz crystal [30] and the ZnHCF preparation on graphite-epoxy composite [31]. Eftekhari [32] reported the dependence of the formal potential values in different supporting electrolytes and the electrocatalytic activity of ZnHCF obtained by a direct modification of the Zn electrode. Several procedures of chemical modification of an electrode are reported as well. Joseph *et al.* [33] studied the behaviour of ZnHCF on wax-impregnated graphite electrode, evaluating the influence of the Zn^{2+} and ferricyanide salts ratio on electrosynthesis step as well as the electrochemical behaviour in different supporting electrolytes. Kemmegne-Mbouguen *et al.* [34] investigate the clay-zinc hexacyanoferrate carbon paste electrode as sensor for Uric acid, Dopamine and Tryptophan.

Furthermore, thanks to the low toxicity of zinc, it could be a valid alternative to replace lithium in aqueous ion batteries [35]. Generally, ZIBs (Water-based Zinc-ion battery) show several advantages, such as high theoretical gravimetric and volumetric capacity of 820 mAh g^{-1} and 5855 MmAh cm^{-3}, low electrochemical potential (-0.76 V vs. SHE), high abundance and intrinsic safety, which are ideal features for an anode material [36, 37].

Several advantages of ZIBs are reported in terms of safety, cost and performances and they are compared with nonaqueous Li/Na/K-ion ones, in table 1.2.

Table 3. 2 Advantages of aqueous ZIBs over nonaqueous Li/Na/K-ion batteries[37]

Characteristics	**Li**	**Na**	**K**	**Zn**
Ionic radius [Å]	0.76	1.02	1.38	0.75
Cost of metal anode (USD) kg^{-1}	19.2	3.1	13.1	2.2
Volumetric capacity (mA h m^{-3})	2042	1050	609	5857

Characteristics	Li	Na	K	Zn
Capacity density [mA h cm^{-3}]	2061	1129	610	5855
Ionic conductivity (S cm^{-1})	10^{-3}–10^{-2} (organic electrolytes)			10^{-1}–6 (aqueous liquid electrolytes)
Safety	Low			High

As cathode types are commonly used manganese- or vanadium-based materials, or Prussian blue analogues. In particular, CuHCF [36]and ZnHCF[38] have been already tested, because of their high output voltage of about 1.6V. In particular, Zhang and al.[38], applied ZnHCF as ZIBs cathode firstly. They synthetized rhombohedral ZnHCF, which led to many $Fe(CN)_6$ vacancies because of the adaption of Zn^{2+} to ZnN_4 tetrahedron rather than an octahedral configuration. Briefly, the reaction involved are the following:

Cathode

$$x Zn^{2+} + 2xe^{-} + Zn_3[Fe(CN)_6]_2 \leftrightarrow Zn_{3+x}[Fe(CN)_6]_2 \quad (1)$$

Anode

$$x Zn \leftrightarrow 2xe^{-} + x Zn^{2+} \quad (2)$$

The electrochemical behaviour of ZnHCF as cathode material in aqueous rechargeable batteries is extensively reported [23, 38–43].

Based on the literature data, substitution or partial substitution with Zn ions occurs in several MHCFs during cycling, such as CuHCF [44]. Li et al.[45] report that the Mn substitution with Fe in MnHCF for Na ion battery, lead to an improvement of the cycle life, limiting the phase transition and the active material dissolution. In addition, Ni et al. demonstrate that the electrochemical stability is improved by the Mn (partially) substitution into the ZnHCF lattice.

3.2 Experimental

3.2.1 ZnHCF-GC modified electrode

Materials

Chemicals were reagent grade from Sigma-Aldrich ($K_3Fe(CN)_6$, $ZnCl_2$, H_3BO_3, KCl, NaCl, LiCl, $SrCl_2$, $MgCl_2$, $BaCl_2$, $CaCl_2$ $Al(NO_3)_3$, $CrCl_3$)and used without any further purification. All experiments have been performed in air, at room temperature and with Millipore Milli-Q nanopure water with a resistivity of ≈ 17MΩcm.

Apparatus

Electrochemical measurements were performed with a Model 730e (CH Instruments) electrochemical workstation using a standard three-electrode electrochemical glass cell (10 ml). The substrate of the working electrode was glassy carbon, GC (diameter = 3 mm) or graphite foil, GF (0.10 mm thick, 99.9%, Goodfellow); and a Pt counter electrode was used. All potentials were reported vs Ag/AgCl reference electrode in saturated KCl.

Preparation of modified electrode

ZnHCF films were deposited by a Zn reduction on GCE through cyclic voltammetry scans in 0.5 M $ZnCl_2$ and 0.4 M H_3BO_3 solution between -0.40 and -1.2 V at 0.1mV/s. Zn-GC modified electrode was soaked in a 50 mM $K_3Fe(CN)_6$ and 0.1M KCl solution for 5 minutes and then dried at room temperature. The electrochemical behaviour in presence of different monovalent, di- and trivalent metal cations was investigated by recording CVs in various supporting electrolytes and following a precise protocol.

Physical Characterisation

To perform SEM and ATR-FTIR analysis, ZnHCF was deposited on graphite foil following the protocol described in the experimental section used for GCE modification. Briefly, the oxidised electrode (ZnHCF-O) was obtained potentiodynamically by applying a linear sweep from OCP to + 1.2 V in KCl 0.1 M, while the reduced electrode (ZnHCF-R) from OCP to + 0.4 V, in the same electrolyte.

ATR- FTIR

IR spectra were recorded from 4000 to 400 cm^{-1} on a PerkinElmer Frontier FT-IR instrument, equipped with single reflection ATR unit (universal diamond ATR top-plate) as a sample support.

SEM

SEM experiments were performed on a field emission scanning electron microscope (FESEM) ZEISS SIGMA 300.

3.2.2 ZnHCF powders

Chemicals and solutions

Chemicals were reagent grade from Sigma-Aldrich ($K_3Fe(CN)_6$, $ZnCl_2$, KCl). Deionized water was used throughout this work. All experiments were carried out at room temperature and in air.

Chemical synthesis

Zinc-hexacyanoferrate powders were synthesized by a co precipitation method: 25mM $ZnCl_2$ solution was dropwise added to a 25mM stirred $K_3Fe(CN)_6$ solution. A yellowish colloidal solution was obtained. The solution was allowed to stand overnight. The precipitated sample was washed with deionized water and centrifuged several times in order to remove the unreacted salts and separate the solid products. The precipitate was dried at 80°C overnight.

Electrochemical measurements

Electrochemical measurements were performed with a Model 730e (CH Instruments) electrochemical workstation using a standard three-electrode electrochemical glass cell (10 ml). The substrate of the working electrode was graphite foil, GF (0.10 mm thick, 99.9%, Goodfellow); and a Pt counter electrode was used. All potentials were reported vs Ag/AgCl reference electrode in saturated KCl. The electrodes were prepared by evaporation of an aqueous suspension of the sample on graphite foil.

X-ray powder diffraction (PXRD)

Powder X-ray diffraction (PXRD) data were recorded by using a monochromatic X-ray beam (wavelength of 1 Å) at the MCX

beamline in ELETTRA synchrotron Trieste (Italy). Data were collected in a capillary geometry, setting the spinner at 300 rpm. The X-ray diffraction pattern was collected consecutively in the range 5º<2θ<70º, with steps of 0.01º and an acquisition time of 1 s/step. The crystal structure was refined using Fullprof Suite [46].

Fourier Transform Infrared spectroscopy (FT/IR)

FT/IR spectra was recorded on a Jasco FT/IR-4600 PLUS instrument working in transmission mode in the spectrum range between 4000 and 500 cm^{-1} and were carried out in solid form using KBr pellet method, containing about 1% w/w of the sample.

Scanning Electron Microscope (SEM)

The morphology of the particles was observed by ESEM Quanta-200 - Oxford Instruments, in High Vacuum. The images were collected with the backscattered electron detector (BSE).

Oxford INCA-350 X-EDS microanalysis system, equipped with Si (Li) detector with thin window for investigations on low atomic number elements.

Atomic Absorption spectroscopy (AAS)

Elementary composition was obtained with Perkin Elmer- Analyst 400 Spectrometer.

Thermogravimetric analysis (TGA)

Thermogravimetric analysis (TGA) was performed in air from room temperature to 500°C, with a heating rate of 5°C/min, and rapid cooling.

3.3 ZnHCF thin film

3.3.1 Electrochemical studies

Zinc hexacyanoferrate films were obtained on a GCE following the double step electrosynthesis protocol detailed in the "Experimental section". Firstly, Zn^0 was deposited on GCE by Cyclic voltammetry (Fig.3.1A), then the soaking of Zn modified-GCE in a $K_3Fe(CN)_6$ solution causes the redox reaction in about 10 minutes. It takes place

on the surface of the electrode, with the conversion of zinc to potassium zinc hexacyanoferrate, as follows:

$3\ Zn^{0} + 6\ K_3Fe^{III}(CN)_6 + \ x\ H_2O \leftrightarrows K_2Zn_3\ [Fe^{II}(CN)_6]_2 \cdot x\ H_2O + 4\ K_4Fe^{II}(CN)_6$ (2)

The ZnHCF films on GCE were characterized in a 0.1M KCl solution by cyclic voltammetry. Voltammograms show the $K_2Zn_3[Fe^{II}(CN)_6]_2$/ $KZn_3[Fe^{III}(CN)_6]_2$ reversible redox couple with a formal potential of about +0.9 V vs Ag/AgCl and a steady current density for the first 30 segments (Figure 3.1B). The CV shape is characterized also by the weak anodic and cathodic peaks at ca. 0.65 V. As reported, this particular morphology is due to the cubic structure [23], that is confirmed also by the SEM analysis (Section 3.2). Furthermore, the stability of the film by repeated CV scans at 0.1 V s^{-1} was checked. The intensity of the cathodic and anodic peak current is stable until the 15^{th} cycle, then, it decreases gradually until 50^{th} cycle and the last cycles are characterized by a fast decrease of the current with the number of the cycles. (Figure 3.1C) The procedure, described in the "Experimental section", was tested several times obtaining charge values with a RSD % of 21. It was obtained by the CVs showed in figure 3.1D. The data is affected by the electrochemical control lacking during the deposition. The stickiness was ensured by the electrode drying at room temperature, whereas the electrode rinsing was a precondition to obtain a well define peak. Three ZnHCF film comparable CV responses were showed in fig. 1D, with similar peak current values. The current involved in the process is closely related to the amount of the electroactive material originated from the reaction taking place on the electrode surface during the soaking step. The calculated surface coverage value was $1.46 \cdot 10^{-08}$ mol/cm^2, considering the charge value of the first five CVs.

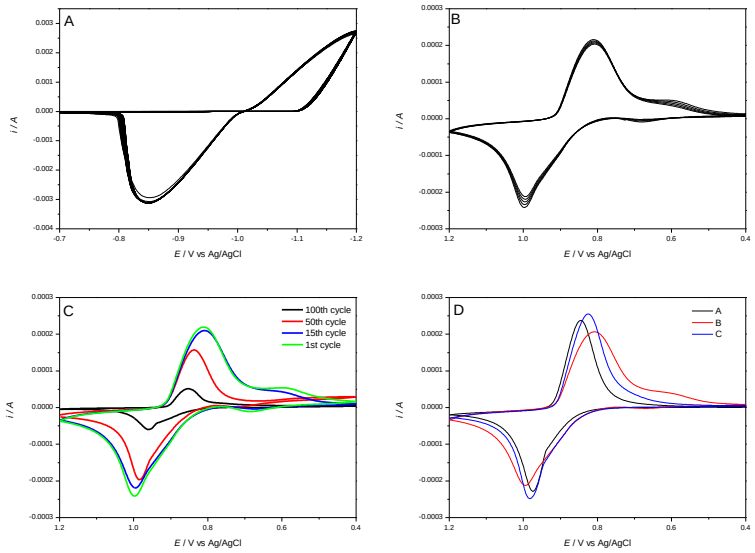

Figure 3.5 A) CV of Zinc electrodeposited on GCE; B) CV of ZnHCF-GC modified electrode at 0.1 V s^{-1} in a 0.1M KCl solution-10 cycles; C) CV of ZnHCF film: 1st cycle, 15th cycle, 50th cycle and 100th cycle recorded; D) First cycles of ZnHCF film CVs response for three different electrodes.

ZnHCF films were characterized using different concentrations of a KCl solution, and the result are reported in Figure 3.3.2. This test reveals the role of the potassium cation in the redox reaction, based on Nerstian equation for a solid film:

$$K_2Zn_2[Fe^{III}(CN)_6]_2 + K^+ + e^- \leftrightarrows K_3Zn_2[Fe^{II}(CN)_6]_2 \quad (3)$$

$$E = k + 0.059 \log [a_{k+}] \quad (4)$$

According to the equation (4), Figure 3.2 shows linear dependence of the two variables (E cathodic vs log of KCl solution concentration) with a slope of about 68 mV, close to theoretical value of 59 mV. This, in turn, confirms a Nerstian behaviour and a one-electron transfer reaction. In addition, the effect of other supporting electrolytes was investigated, the results are shown in section 3.3.

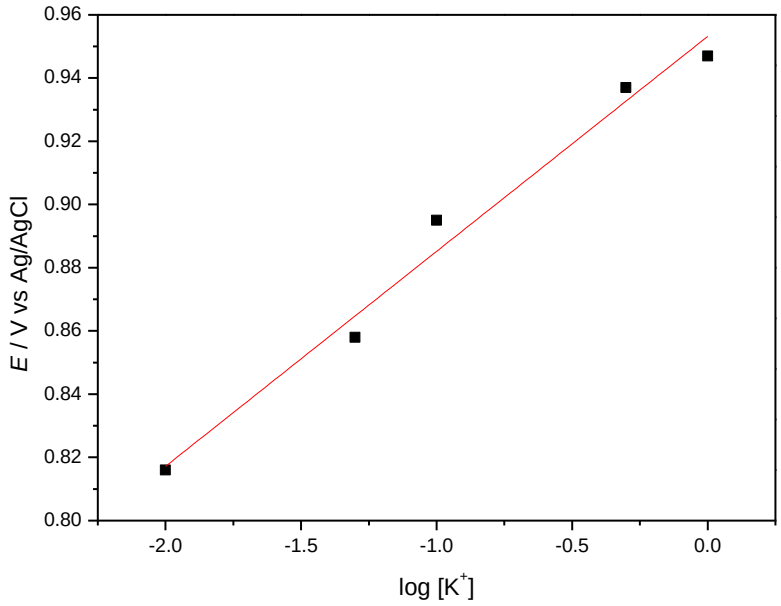

Figure 3.6 Potential vs log[K^+] of ZnHCF-GC modified electrode

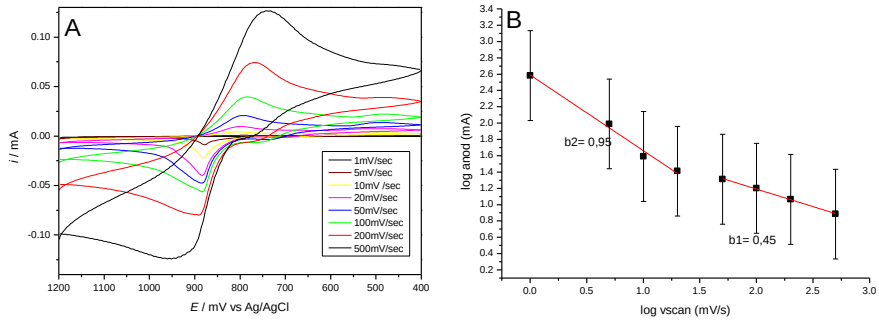

Figure 3.7 A) ZnHCF-GC modified electrode at several scan rate in KCl 0.1 M; B) Relation between log ip_A (mA) and log scan rate (mV/s)

Figure 3.3B shows the characterization of the ZnHCF electrode in terms of anodic current dependence to the scan rate. Specifically, the CVs of ZnHCF-GCE at several scan rates are displayed in Figure 3.3A. The curves highlighted that the decreasing of the scan rate causes a decreasing of the anodic and cathodic peaks, as expected, and a shifting of E^0. A checking the power-law relationship with the scan rate, i.e.; $i = av^b$ where i is the current of anodic and cathodic peaks, v the scan rate, and a and b are experimental parameters, is

shown in the panel B of the Figure 3.3. The panel displays two different slopes for the log(*v*) -log(*i*) plot, where b value is about 0.5 at higher scan rate underling a diffusion-controlled process, whereas b is quoted around 1 at low scan rate, indicating a surface-controlled process. Therefore, the K^+ insertion/de-insertion processes are surface-controlled at lower scan rates and diffusion-controlled at higher ones. In light of this evidence, we consider 100 mVs^{-1} is a suitable scan rate to investigate ZnHCF capability as ionic sieve, which ensure the occurrence of a diffusion controlled-process. Similar results were reported by Eftekhari and Joseph et al. [32, 33], who studied the effect of the support electrolytes at high scan rate and at low scan rate, respectively. Eftekhari reported the effect of the support electrolytes on the voltammogram shape and formal potential shifting of the ZnHCF chemically modified electrode, testing several alkali cations, while Joseph et al. focused on surface processes of a ZnHCF- wax-impregnated graphite electrode.

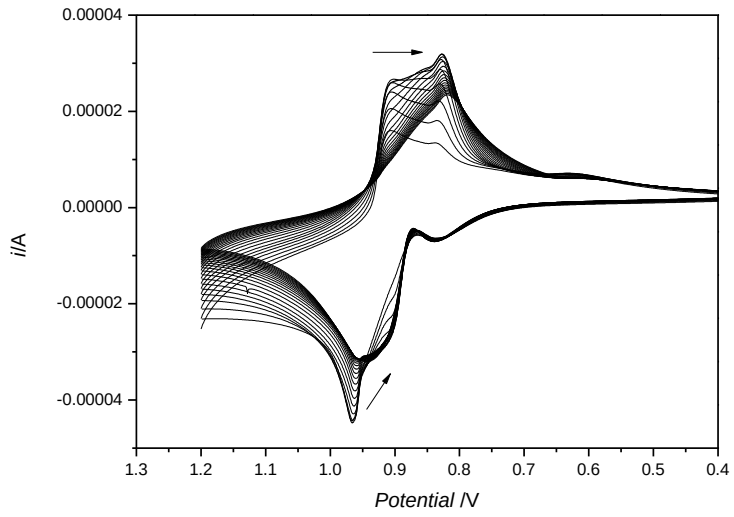

Figure 3.8 ZnHCF in Mixture 0.1M $ZnCl_2$ and 0.1M KCl $0.1Vs^{-1}$ vs Ag/AgCl

Figure 3.4 shows the voltammogram of ZnHCF-film in a mixture electrolyte of $ZnCl_2$ and KCl. It is worth noting the shifting of the CV scans to lower potential, which indicates the accommodation of Zn^{2+} as well as K^+. After ca. 10 cycles the voltammogram stabilised.

The film was studied also in 0.1M $ZnCl_2$ and in 0.1M KCl, the results are showed in Fig. 3.5. The ZnHCF voltammograms in $ZnCl_2$ are lightly shifted if compared to KCl scans. It indicates the Zn^{2+} uptake/releasing, as already reported [23, 38]. Furthermore, in the support electrolyte mixture (0.1M $ZnCl_2$ and 0.1M KCl) both redox couples are observed, which means the intercalation of both Zn^{2+} and K^+. In particular, the black CV shape results different both from the red CV and the blue one. It means that ZnHCF hosts both K^+ and Zn^+ at the same time. Furthermore, the isosbetic points at ca 0.95 V indicate the transformation from KZnHCF to a mixture of KZnHCF and ZnZnHCF. The mass balance condition was maintained.

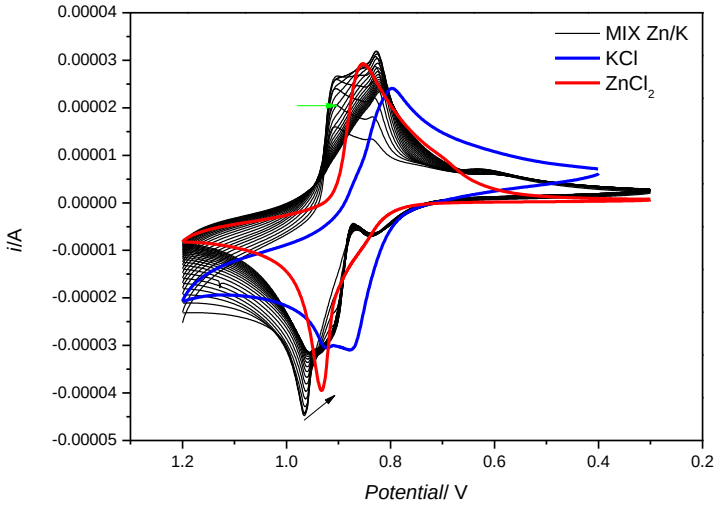

Figure 3.9 ZnHCF in Mixture 0.1 M $ZnCl_2$ and 0.1M KCl (black line), in 0.1M $ZnCl_2$ (red line) and 0.1M KCl (blue line) at $0.1 Vs^{-1}$ vs Ag/AgCl

3.3.2 Physico-chemical characterization of ZnHCF films

The ZnHCF was electrodeposited on grafoil following the same experimental protocol, in order to be investigated by SEM and *ATR-FTIR* spectroscopy. For this purpose, two different electrodes were analysed: ZnHCF-O, referring to the oxidized electrode and ZnHCF-R to the reduced one.

SEM characterization reveals a surface morphology composed of poly-dispersed particles that are aggregated to form a porous network. The ZnHCF-samples consist of size-heterogeneous particles, of about 100-300 nm (Fig. 3.6C), although some particles

are bigger (Fig. 3.6B). The morphology is characterized by cubic particles which are pointed out distinctly, at a nanometric level as well. The cubes visible in the figure can be related to the cubic structure of zinc hexacyanoferrate. The morphologies displayed in the Fig. 3.6A and 3.6B, for the ZnHCF-R and ZnHCF-O respectively, confirms a similar behaviour of the modified electrode. Therefore, the potentiodynamic modification do not affect the overall shape and morphology of the films.

FTIR characterization provides useful information on the oxidation state of the studied compounds. The ATR-FTIR spectra of the oxidised and reduced electrodes are represented in Figure 3.7. All samples show a broad band of the ν_{CN} adsorption at about 2000-2200 cm^{-1}, as expected for bimetallic cyanide Fe-C-N-Zn, which can be used as a fingerprint of the oxidation state. A close inspection of the figure reveals that the spectrum recorded for ZnHCF-O shows a band at 2096 cm^{-1}, which is close to the band at 2091 cm^{-1} founded for Fe^{II}-C-N-Zn^{II} system [41]. In addition, the insert in the figure displays a couple of broad peaks at 489 cm^{-1} and 603 cm^{-1} which are related to Zn-N and Fe-C stretching respectively. Lastly, peak at 1622 cm^{-1} and 3620 cm^{-1} are due to the presence of OH from water molecules.

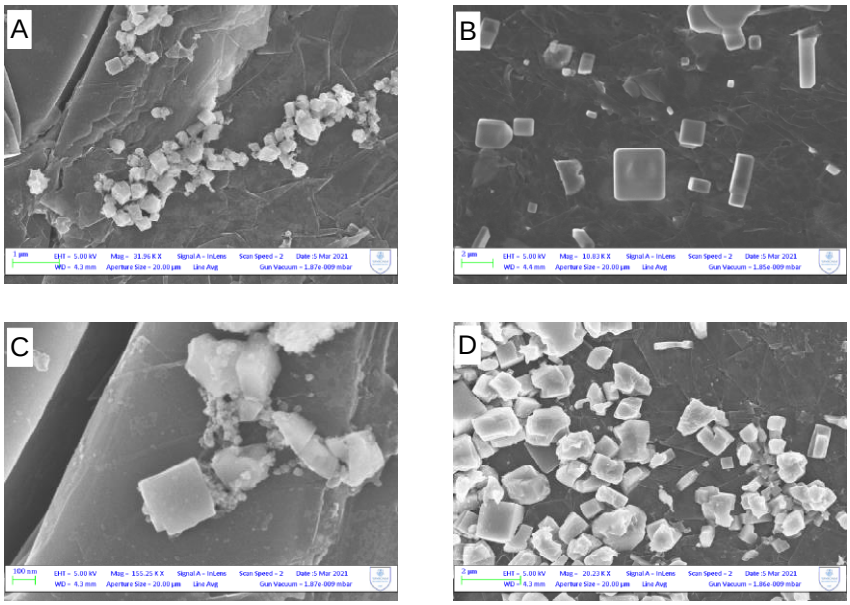

Figure 3.10 SEM micrographs of ZnHCF modified electrodes: A) and D) ZnHCF-R at different magnification; B) and C) ZnHCF-O at different magnification.

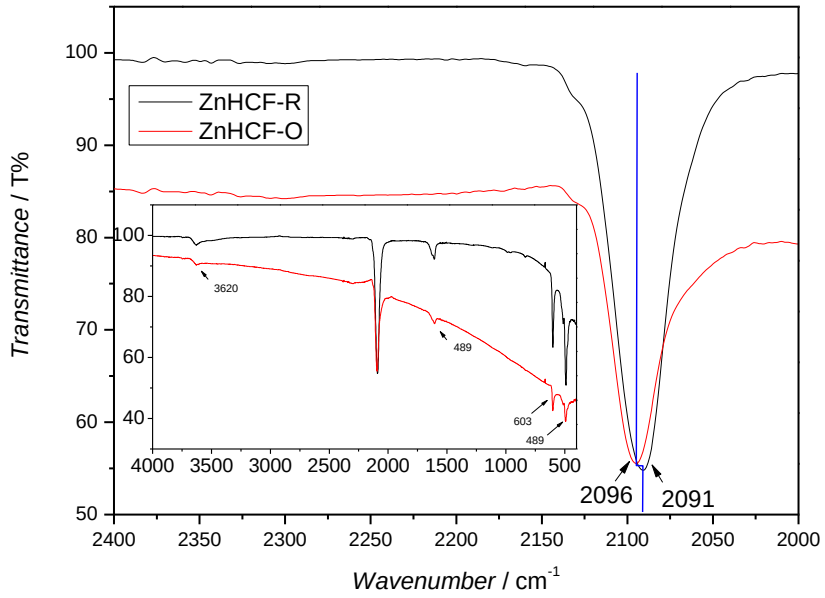

Figure 3.11ATR-FTIR spectra of ZnHCF-O and ZnHCF-R on graphite foil.

3.3.3 Exchange capability

A precise protocol was followed to investigate the ZnHCF-GCE electrochemical behaviour in several mono-, di- and trivalent cations in order to evaluate the affinity of the tested cations compared to K^+:

the first CV was recorded in 0.1 M KCl; the second CV was recorded in 0.1 M of cation tested, and finally the last CV was repeated in 0.1 M KCl [16].

The CVs of ZnHCF-GCE was studied in different support electrolyte cations in addition to K^+. The results are shown in Fig. 3.8A (all cations), 3.8B (monovalent cations), 3.8C (divalent cations) and D (trivalent cations).

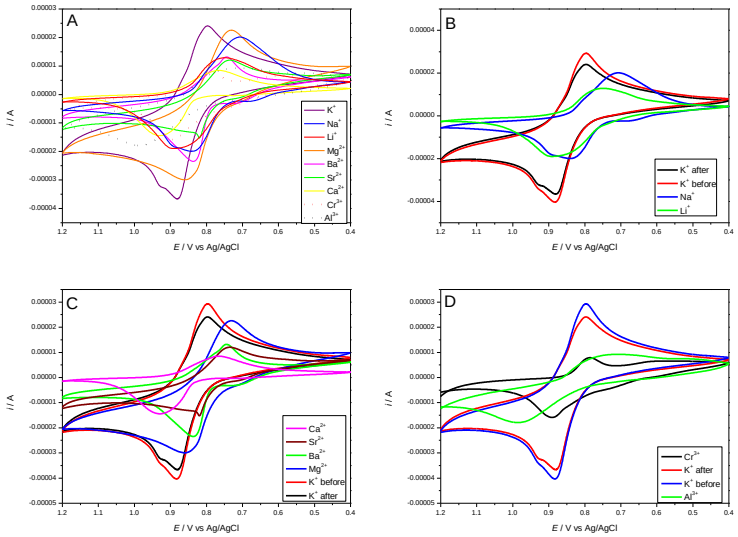

Figure 3.12 CVs of ZnHCF film in A) 0.1M LiCl, NaCl, $MgCl_2$, $CaCl_2$, $SrCl_2$, $BaCl_2$, $CrCl_3$, $Al(NO_3)_3$, KCl before and after exchanges; B) in 0.1M KCl before and after 0.1M LiCl and NaCl; C) in 0.1M KCl before and after 0.1M $MgCl_2$, $CaCl_2$, $SrCl_2$ and $BaCl_2$; D) in 0.1M KCl before and after 0.1M $CrCl_3$, $Al(NO_3)_3$

The various cation species cause a potential shifting and a peak shape variation (Fig. 3.8A). This behaviour has been reported for other MHCFs [47–49] and rationalized in terms of cation overall dimension. An insertion/de-insertion mobility order of monovalent cations was reported for ZnHCF film, and potassium shows the best cation mobility [33]. Fig. 3.8 B, C and D show the ZnHCF film capability to intercalate/de-intercalate respectively monovalent, divalent and trivalent cations compared to K^+. The perfect reversibility of the process is confirmed for all the cations, by the CV recorded in K^+ before and after the CV. There is almost complete

match of the pristine and of the recovered CVs in potassium salt, also in terms of peak current. This unambiguously electrochemical behaviour suggest that ZnHCF film here reported has the capacity to exchange mono-, divalent- and trivalent cations with high efficiency. Kinetics of the exchange was also investigated, and our experimental data suggests that the uptake of di- or trivalent ions is slower than the uptake of the potassium. For example, Figure 3.9 shows the CVs of ZnHCF recorded in KCl 0.1 M, in $CaCl_2$ 0.1 M and then back to KCl. Unlike the CV related to the re-uptake of K^+ ion, the CV recorded during the insertion of Ca^{2+} shows a potential shift from the first segment to the steady last ones. A similar behaviour does not occur for the potassium insertion, in fact the voltammogram (Fig. 3.9A) is characterized by the overlapping segments. Therefore, these processes are controlled by kinetics and the uptake of di- and trivalent cations takes place slowly, whereas smaller radii cations were exchanged easily. Although the channel diameter for metals hexacyanoferrates is similar and close to 320pm, the cationic radii influence the potential shift and also the attitude of each ion to be inserted and de-inserted [50].

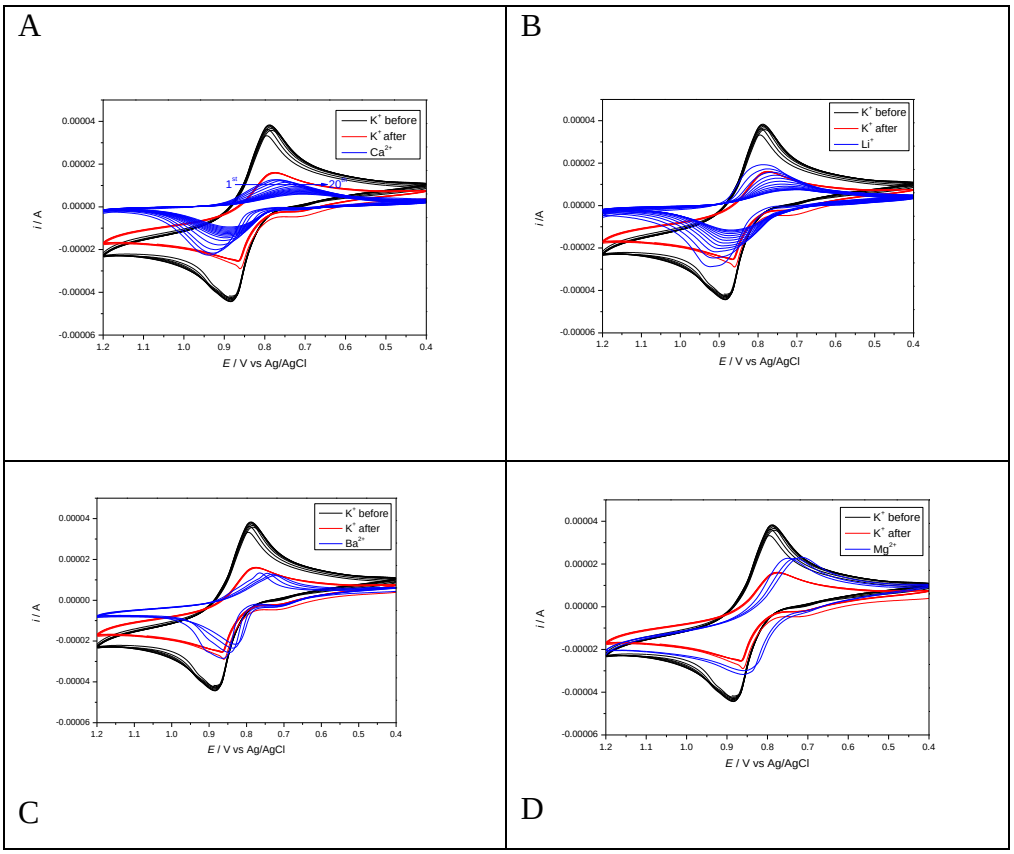

Figure 3.13 ZnHCF film in: A) KCl 0.1M (black line); $CaCl_2$ 0.1M (blue line); KCl 0.1M after $CaCl_2$ (red line); B) KCl 0.1M (black line); LiCl 0.1M (blue line); KCl 0.1M after LiCl (red line); C) KCl 0.1M (black line); $BaCl_2$ 0.1M (blue line); KCl 0.1M after $BaCl_2$ (red line); D) KCl 0.1M (black line); $MgCl_2$ 0.1M (blue line); KCl 0.1M after $MgCl_2$ (red line)

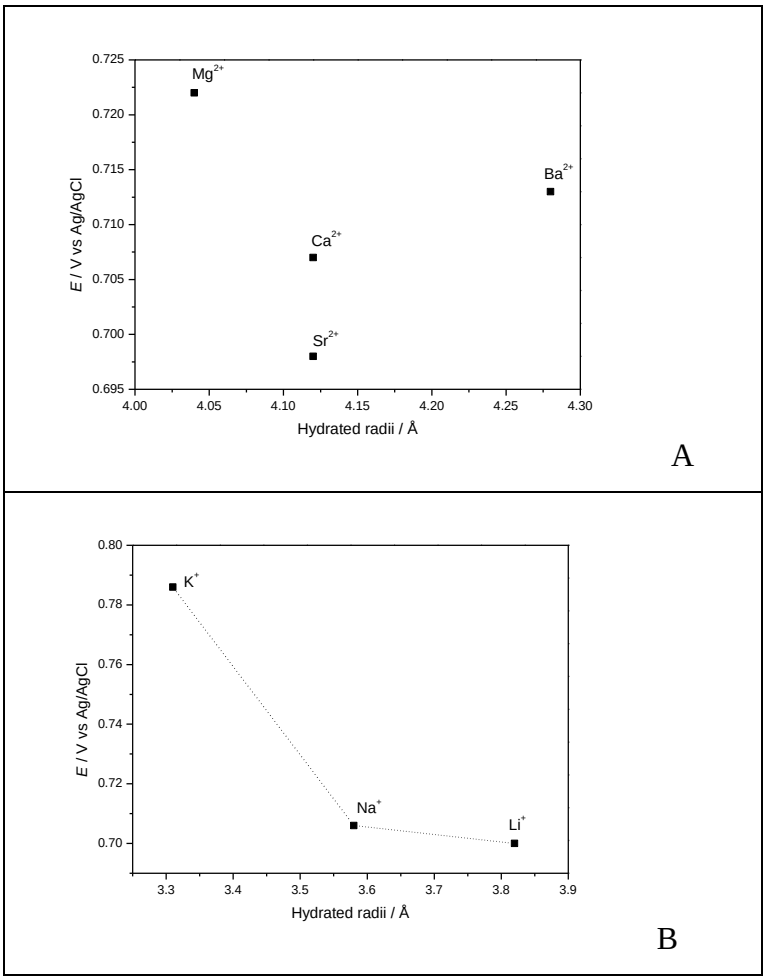

Figure 3.14 Variation of ZnHCF potential vs and Hydrated radius of: Mg, Ca, Sr and Ba; B) Li, Na and K.

Table 3.3 Ionic and hydrated radii, cathodic and anodic potential of different cations tested.

	Ionic radii r_x(Å) [51]	**Hydrated ionic radii r_h (Å)** [51]	**Cathodic Potential (V) vs Ag/AgCl**	**Anodic Potential (V) vs Ag/AgCl**
Li^+	0.6	3.82	0.700	-0.870
Na^+	0.95	3.58	0.706	-0.838
K^+	1.33	3.31	0.786	-0.881
Mg^+	0.65	4.28	0.713	-0.858
Ca^{+2}	0.99	4.12	0.707	-0.896
Sr^{+2}	1.13	4.12	0.698	-0.801
Ba^{+2}	1.35	4.04	0.722	-0.828
Al^{+3}	0.5	4.75	0.723	-0.988
Cr^{+3}	0.64	4.61	0.774	-0.870

Figure 3.10 shows the relationship between radii size (hydrated radius) of alkali cations and the ZnHCF intercalation potential. It decreases with the hydrated radii size (in details in Table 3.3), following the order K>>Na>Li, as also accepted for other MHCFs [52]. ZnHCF easily hosts alkali earth cations as well. The diffusion coefficients (D_{app}) were calculated by the Ip vs $v^{½}$ slope. As showed in Table 3.4, potassium D_{app} is by far the highest as described by the potential vs hydrated radius. As a matter of fact, Li^+ shows a faster diffusion then Na^+ into ZnHCF, even though their D_{app} values are comparable. The CVs (fig. 3.9) show a good reversible process in spite of the increasing of ionic radii size of the cations accommodated into the structure. As matter of fact, the lattice might go to microstructural distortions. Ions with smaller ionic radii have larger hydrated radii so they hold on their hydration shells. On the other hand, larger radii ions are less strongly hydrated, therefore they able to break off their hydration shells during the insertion into the ZnHCF lattice.

Table 3.4 Diffusion coefficient (D_{app}) of alkali cation (0.1M solution) in the ZnHCF film, obtained from CV at high scan rates.

Cation	**Li^+**	**Na^+**	**K^+**
10^{-8} D_{app}*rid* (cm^2 s^{-1})	3.66	1.67	8.56
10^{-8} D_{app}*ox* (cm^2 s^{-1})	5.08	3.28	6.02

3.4 ZnHCF powders

3.4.1 Characterization

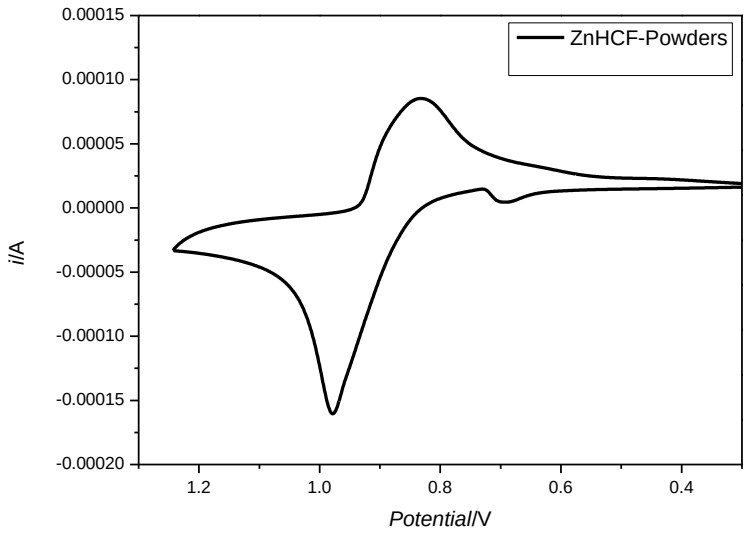

Figure 3.15 ZnHCF powders on grafoil in a 0.1M KCl solution at 0.1 Vs^{-1}

The electrochemical measurement recorded between 1.2 and 0.2V at 0.1V/s in a KCl 0.1M solution shows a two peaks voltammogram at about 1V and 0.8V corresponding to the species $Zn_3[Fe(CN)_6]_2$ and $Zn[Fe(CN)_6]$, respectively.

The general formula $Zn_3[Fe(CN)_6]_2{\cdot}xH_2O$ where *x* equals 0 indicates the rhombic phase, where Zn^{II} has a tetrahedral configuration, saturated by four cyanide and without coordinative water [2].

The IR spectra of hexacyanometallates shows the *ν*(CN) band frequency fingerprint between 2000-2200cm^{-1}, detecting the electronic configuration.

Specifically, for $Zn_3[Fe(CN)_6]_2$ two strong peaks at 2185 cm^{-1} and at 2099 cm^{-1} were evaluated as shown in Fig 3.12. The band at 2100 cm^{-1} is attributed to the CN stretching in the Fe–CN–Zn of ZnHCF. A high absorption frequency is due to the rhombohedral structure indicating, also no coordinated water in the structure [39].

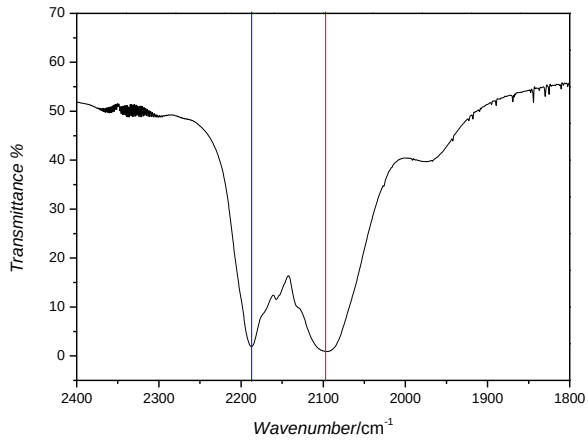

Figure 3.16 v(CN) vibration band of Zinc Hexacyanoferrate powders.

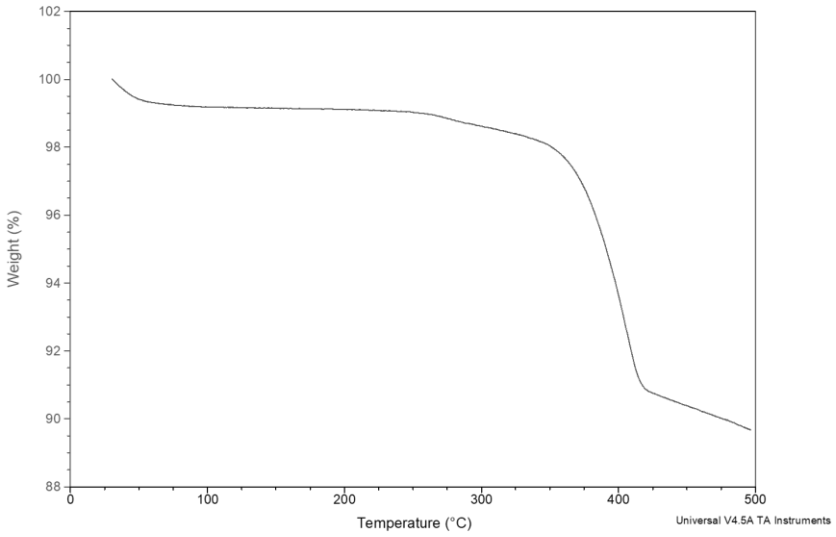

Figure 3.17 Thermo-gravimetric curve

TG curve reveals a negligible weight loss, suggesting the absence of coordinative water and confirming the rhombic phase of ZnHCF.

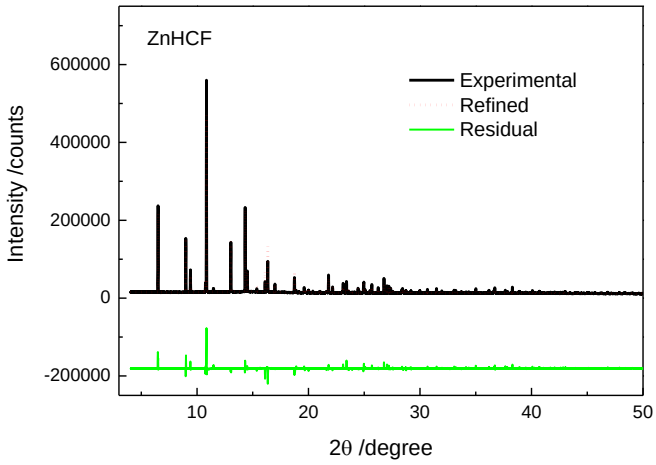

Figure 3.18 XRPD pattern and refinement of ZnHCF

ZnHCF was taken for XRD analysis to confirm both the success of the synthesis and the identification of the structure lattice. The diffraction patterns obtained for the sample were consistent with the rhombic phase as has been reported [23]. ZnHCF shows a rhombohedral structure (space group: R-3C) with a, b, c and γ equal to 12.57(9) Å, 12.57(9) Å, 33.05 (1) Å and 120º, respectively (figure 3.14).

SEM images show a well-organized structure related to the rhombic phase. Furthermore, according to Zhang et al. concentration of reagents influences the structure of the ZnHCF. In fact, a 25mM $ZnCl_2$ solution was used in a 1:1 molar ratio with $K_3Fe(CN)_6$ obtaining only one phase (Fig. 3.15) . Also, chemical composition obtained by SEM analysis matches with AAS-analysed one.

Table 3.5 Comparison of atoms ratio in ZnHCF powders tested by AAS and SEM

	AAS	**SEM** WD 14mm abundance percentage (%)
C	-	40,41
Fe	7.375 mmol	7,67
Zn	9.95 mmol	11.39
K	0.277 mmol	-

Elemental composition was giving from AAS as $K_{0.04}Zn_{1.35}[Fe(CN)_6]$ and confirmed by SEM elemental analysis.

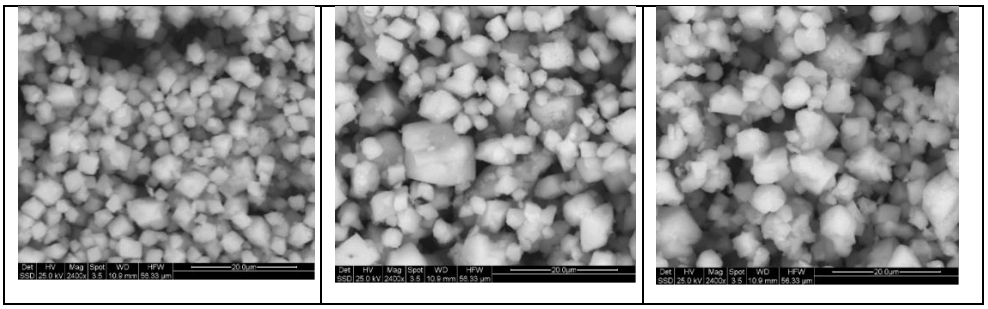

Figure 3.19 SEM images of ZnHCF powders

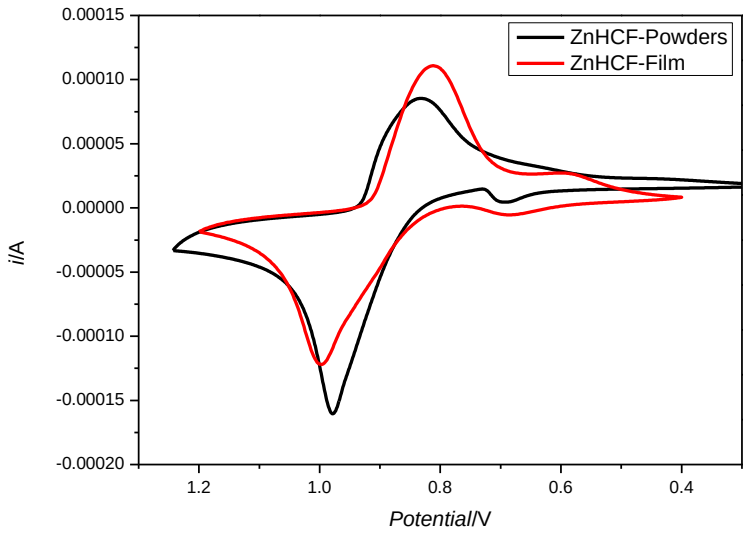

Figure 3.20 CVs overlay of ZnHCF-powders and ZnHCF-film in KCl 0.1 M at 0.1 Vs^{-1} vs Ag/AgCl.

Also, the CVs confirm the same behaviour both for ZnHCF powders and ZnHCF thin film.

3.4.2-ZIBs

ZnHCF powders were tested to check the potential use of a ZnHCF-based cathode material in aqueous Zn-ion batteries (ZIB). In addition, it was used as a standard to compare data obtained from a similar material based on metal hexacyanoferrates, the MnHCF as a cathode in ZIBs.

Zn/ZnHCF battery electrochemical proprieties were evaluated cyclic voltammetry at first, as indicated in the figure 3.17.

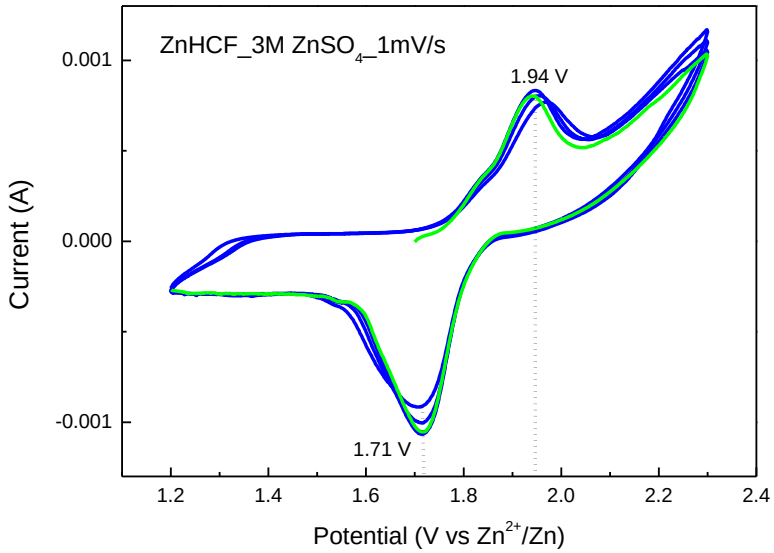

Figure 3.21 CV curve of ZnHCF vs Zn^{2+}/Zn at 1 mVs^{-1}

Zn/ZnHCF shows a reversible process during cycling (Fig. 3.17), two different peaks at 1.94 V in oxidation and at 1.71 V in reduction are visible. The difference between cathodic and anodic peaks (ΔEp) of 230mV indicates the reversible intercalation/deintercalation of Zn^{2+} into the lattice of ZnHCF. Thus, the moving direction of cations

follow the scheme, suggested by Zhang et al.[53]:

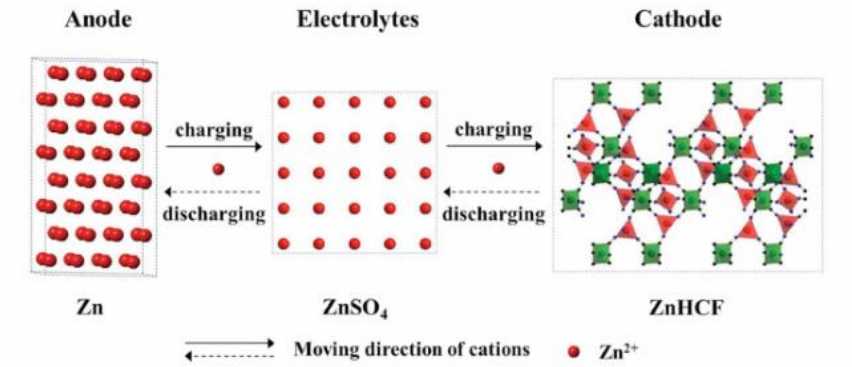

Figure 3.22 Schematic moving direction of cations into the battery

Two electrochemical reactions (1) and (2) occur:

$$\text{Cathode : } Zn^{2+} + 2\,\lambda\, e^- + Zn_3[Fe(CN)_6]_2 \leftrightarrows Zn_{3+\lambda}[Fe(CN)_6]_2 \qquad (1)$$

$$\text{Anode: } \lambda\, Zn \leftrightarrows + 2\,\lambda\, e^- + \lambda\, Zn^{2+} \qquad (2)$$

Indeed the insertion/de-insertion of Zn into the ZnHCF lattice occurs effortlessly, as already reported by Zhang and al.[55]. This behaviour was also confirmed by CVs and XRD patterns.

The charge and discharge profile of ZnHCF at C/5 is shown in figure 3.19, with a discharge capacity around 60 mAh g^{-1}, and a discharge plateau around 1.71 V, which is interesting. However, the cyclability performance shown in figure 3.4.7 indicates a consistent capacity fading, and only around 33% capacity was retained after 50 cycles. This might be due to the dissolution of ZnHCF material, as reported by Zhang and Ni et al. [53, 54].

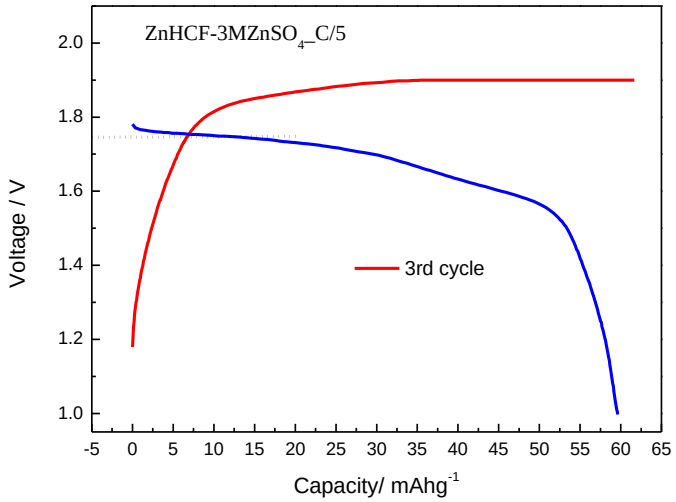

Figure 3.23 Galvanostatic charge (red)/discharge (blu) curves of ZnHCF at C/5.

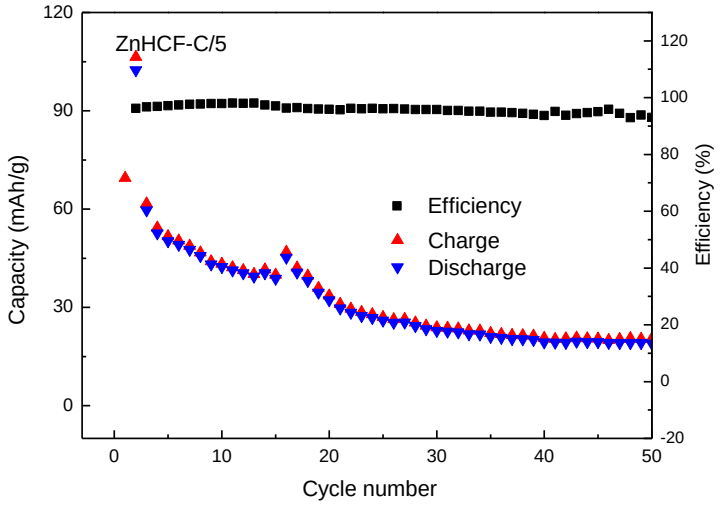

Figure 3.24 Cycling performance of ZnHCF at C/5 rate

These tests were useful to compare the Zn/MnHCF cell behaviour, whose cathode material is similar but with another transition metal coordinating the cyanide in HCFs, the manganese. MnHCF full-cell was tested through CV, as shown in figure 3.21. The redox peaks form 10th to 50th shown similar trend as the first 10 cycles, and the current intensity of the anode peak at around 1.7 V and two

reduction peaks at 1.20-1.40 V are increasing within the first 30 cycles, and after that the current intensity reaches a stable state from 40-50 cycles. Meanwhile, the reduction peak at 1.70-1.75 V keeps decreasing, and becomes stable after 30 cycles.

A rationalization of this behaviour is the following. MnHCF material is reported to display a partial substitution of Mn during cycling, most likely due to the activation of iron sites, with concomitant formation of the ZnHCF phase. Therefore the Zn^{2+} intercalation/ process does not occur in a reversible way, but follows a partial substitution Mn-Zn, as confirmed by Li and al.[46].

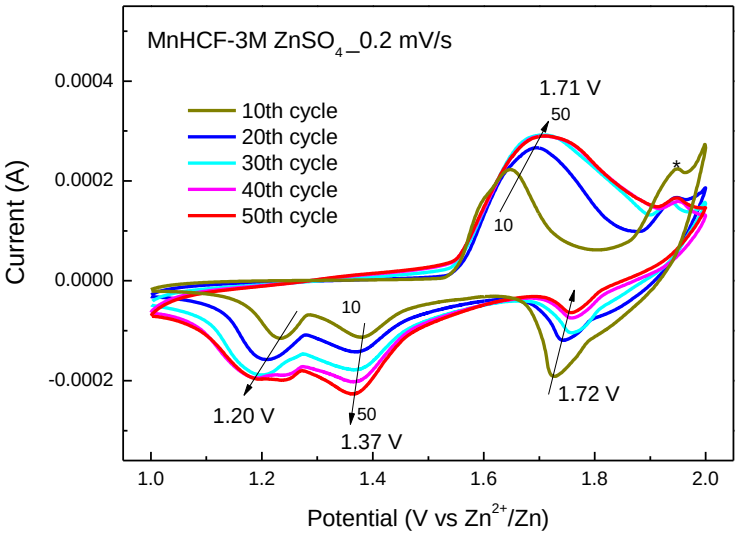

Figure 3.25 CV curves of MnHCF full-cell at 0.2 mV s^{-1} form 10th to 50th cycles

We emphasises here the use of ZnHCF powders for the sake of comparison in this application: firstly because of its unique phase, and secondly because the phase was rhombohedral distinguishable from the MnHCF monoclinic one.

3.5 Conclusion

Films of zinc hexacyanoferrate have been deposited on a Glassy Carbon electrode with a specific protocol aimed at ensuring reproducible electrode characteristics. The morphology of the electrodeposited material has been further studied by SEM. and ATR-FTIR spectroscopy confirming the occurrence of the Fe^{II}-C-N-Zn^{II} structural unit. A full electrochemical characterisation suggested a good stability of the film and the capacity to intercalate several both mono and di-valent cations. Kinetics of the intercalation/deintercalation process has been also addressed. Overall. the low-toxicity and cheapness zinc make zinc hexacyanoferrate films a promising candidate for application in ion exchange system.

Otherwise, ZnHCF powders were characterized by different techniques. All of them confirmed that the synthesis procedure allowed to obtain only the rhombic phase. The CV scans of ZnHCF powders matched with the ZnHCF film ones. Galvanostatic tests show a considerably fast capacity fading. Furthermore, using it as standard we were able to check the Mn-Zn replacement rather than the insertion of zinc ions during cycling.

References

1. Chillawar RR, Tadi KK, Motghare RV (2015) Voltammetric techniques at chemically modified electrodes. J Anal Chem 70:399–418. https://doi.org/10.1134/S1061934815040152
2. Murray RW, Ewing AG, Durst RA (1987) Chemically Modified Electrodes Molecular Design for Electroanalysis. Anal Chem 59:379A-390A. https://doi.org/10.1021/ac00132a721
3. Kimmel DW, LeBlanc G, Meschievitz ME, Cliffel DE (2012) Electrochemical Sensors and Biosensors. Anal Chem 84:685–707. https://doi.org/10.1021/ac202878q
4. Isfahani VB, Memarian N, Dizaji HR, et al (2019) The physical and electrochromic properties of Prussian Blue thin films electrodeposited on ITO electrodes. Electrochimica Acta 304:282–291. https://doi.org/10.1016/j.electacta.2019.02.120
5. Mullaliu A, Giorgetti M (2019) Metal Hexacyanoferrates: Ion Insertion (or Exchange) Capabilities. In: Inamuddin, Ahamed MI, Asiri AM (eds) Applications of Ion Exchange Materials in the Environment. Springer International Publishing, Cham, pp 109–133
6. Mortimer RJ, Rosseinsky DR (1983) Electrochemical polychromicity in iron hexacyanoferrate films, and a new film form of ferric ferricyanide. Journal of Electroanalytical Chemistry and Interfacial Electrochemistry 151:133–147. https://doi.org/10.1016/S0022-0728(83)80429-X
7. Shan Y, Yang G, Gong J, et al (2008) Prussian blue nanoparticles potentiostatically electrodeposited on indium tin oxide/chitosan nanofibers electrode and their electrocatalysis towards hydrogen peroxide. Electrochimica Acta 53:7751–7755. https://doi.org/10.1016/j.electacta.2008.05.035
8. Zadronecki M, Wrona PK, Galus Z (1999) Study of Growth and the Electrochemical Behavior of Prussian Blue Films Using Electrochemical Quartz Crystal Microbalance. J Electrochem Soc 146:620–627. https://doi.org/10.1149/1.1391653
9. Giorgetti M, Scavetta E, Berrettoni M, Tonelli D (2001) Nickel hexacyanoferrate membrane as a coated wire cation-selective electrode. Analyst 126:2168–2171. https://doi.org/10.1039/b107034g
10. Pasta M, Wessells CD, Liu N, et al (2014) Full open-framework batteries for stationary energy storage. Nat Commun 5:3007. https://doi.org/10.1038/ncomms4007
11. Park SI, Gocheva I, Okada S, Yamaki J (2011) Electrochemical Properties of NaTi2(PO4)3 Anode for Rechargeable Aqueous Sodium-Ion Batteries. J Electrochem Soc 158:A1067. https://doi.org/10.1149/1.3611434
12. Mullaliu A, Asenbauer J, Aquilanti G, et al (2020) Highlighting the Reversible Manganese Electroactivity in Na-Rich Manganese Hexacyanoferrate Material for Li- and Na-Ion Storage. Small Methods 4:1900529. https://doi.org/10.1002/smtd.201900529
13. Lilga MA, Orth RJ, Sukamto JPH, et al (2001) Cesium separation using electrically switched ion exchange. Separation and Purification Technology 24:451–466. https://doi.org/10.1016/S1383-5866(01)00145-9
14. Ciabocco M, Berrettoni M, Zamponi, Silvia (2018) An Overview on the Facile and Reversible Cations Intercalation in Nickel-Hexacyanoferrate Open Framework. Int J Electrochem Sci 5535–5551. https://doi.org/10.20964/2018.06.37
15. Wang RY, Shyam B, Stone KH, et al (2015) Reversible Multivalent (Monovalent, Divalent, Trivalent) Ion Insertion in Open Framework Materials. Adv Energy Mater 5:1401869. https://doi.org/10.1002/aenm.201401869
16. Ciabocco M, Berrettoni M, Zamponi S, et al (2013) Electrochemical behavior of Inhcf in alkali metal electrolytes. J Solid State Electrochem 17:2445–2452. https://doi.org/10.1007/s10008-013-2123-2
17. Chen R, Tanaka H, Kawamoto T, et al (2013) Selective removal of cesium ions from wastewater using copper hexacyanoferrate nanofilms in an electrochemical system. Electrochimica Acta 87:119–125. https://doi.org/10.1016/j.electacta.2012.08.124
18. Prout WE, Russell ER, Groh HJ (1965) Ion exchange absorption of cesium by potassium hexacyanocobalt (II) ferrate (II). Journal of Inorganic and Nuclear Chemistry 27:473–479. https://doi.org/10.1016/0022-1902(65)80367-0
19. Ding D, Lei Z, Yang Y, et al (2014) Selective removal of cesium from aqueous solutions with nickel (II) hexacyanoferrate (III) functionalized agricultural residue–walnut shell. Journal of Hazardous Materials 270:187–195. https://doi.org/10.1016/j.jhazmat.2014.01.056
20. Parajuli D, Takahashi A, Noguchi H, et al (2016) Comparative study of the factors associated with the application of metal hexacyanoferrates for environmental Cs decontamination. Chemical Engineering Journal 283:1322–1328. https://doi.org/10.1016/j.cej.2015.08.076
21. Jang S-C, Hong S-B, Yang H-M, et al (2014) Removal of Radioactive Cesium Using Prussian Blue Magnetic Nanoparticles. Nanomaterials 4:894–901. https://doi.org/10.3390/nano4040894
22. Gromadskyi D, Chervoniuk V, Kirillov S (2016) Cyclic voltammetric study of tin hexacyanoferrate for aqueous battery applications. Journal of Electrochemical Science and Engineering 6:225–234. https://doi.org/10.5599/jese.289
23. Ni G, Han B, Li Q, et al (2016) Instability of Zinc Hexacyanoferrate Electrode in an Aqueous Environment: Redox-Induced Phase Transition, Compound Dissolution, and Inhibition. ChemElectroChem 3:798–804. https://doi.org/10.1002/celc.201500538
24. Asai M, Takahashi A, Tajima K, et al (2018) Effects of the variation of metal substitution and electrolyte on the electrochemical reaction of metal hexacyanoferrates. RSC Adv 8:37356–37364. https://doi.org/10.1039/C8RA08091G
25. Malik MA, Kulesza PJ, Marassi R, et al (2004) Countercation intercalation and kinetics of charge transport during redox reactions of nickel hexacyanoferrate. Electrochimica Acta 49:4253–4258. https://doi.org/10.1016/j.electacta.2004.04.021
26. Lu Y, Wang L, Cheng J, Goodenough JB (2012) Prussian blue: a new framework of electrode materials for sodium batteries. Chem Commun 48:6544–6546. https://doi.org/10.1039/C2CC31777J
27. Shen L, Wang Z, Chen L (2014) Prussian Blues as a Cathode Material for Lithium Ion Batteries. Chemistry – A European Journal 20:12559–12562. https://doi.org/10.1002/chem.201403061
28. Do Carmo DR, Franco DW, Rodrigues Filho UP, et al (2001) THE CYANIDE PHOTOISOMERIZATION IN ZINC HEXACYANOFERRATE (II) SUPPORTED ON TITANIUM DIOXIDE-SILICA GEL COMPOSITE: A MATRIX EFFECT. Journal of Coordination Chemistry 54:455–468. https://doi.org/10.1080/00958970108022656
29. Solfa dos Santos V (2017) Voltammetric Behavior of Zinc Hexacyanoferrate (III) Nanoparticles and Their Application in the Detection of N- Acetylcysteine. Int J Electrochem Sci 7142–7153. https://doi.org/10.20964/2017.08.06
30. Fenga PG, Stradiotto NR (2011) Study of zinc hexacyanoferrate—modified platinum electrodes using electrochemical quartz crystal microbalance. J Solid State Electrochem 15:1279–1286. https://doi.org/10.1007/s10008-010-1187-5
31. Fenga PG, Stradiotto NR, Pividori MI (2010) Preparation and Characterization of Graphite-Epoxy Composite Modified with Zinc Hexacyanoferrate and Their Electrochemical Behaviour in Presence of Substituted Anilines. Electroanalysis 22:2979–2984. https://doi.org/10.1002/elan.201000003

32. Eftekhari A (2002) Electrochemical behavior and electrocatalytic activity of a zinc hexacyanoferrate film directly modified electrode. Journal of Electroanalytical Chemistry 537:59–66. https://doi.org/10.1016/S0022-0728(02)01248-2
33. Joseph J, Gomathi H, Rao GP (1997) Modification of carbon electrodes with zinc hexacyanoferrate. Journal of Electroanalytical Chemistry 431:231–235. https://doi.org/10.1016/S0022-0728(97)00169-1
34. Kemmegne-Mbouguen JC, Angnes L, Mouafo-Tchinda E, Ngameni E (2015) Electrochemical Determination of Uric Acid, Dopamine and Tryptophan at Zinc Hexacyanoferrate Clay Modified Electrode. Electroanalysis 27:2387–2398. https://doi.org/10.1002/elan.201500110
35. Zhu W, Wang W, Xue W, et al (2021) Achieving a Zn-ion battery-capacitor hybrid energy storage device with a cycle life of more than 12,000 cycles. Composites Part B: Engineering 207:108555. https://doi.org/10.1016/j.compositesb.2020.108555
36. Trócoli R, La Mantia F (2015) An aqueous zinc-ion battery based on copper hexacyanoferrate. ChemSusChem 8:481–485. https://doi.org/10.1002/cssc.201403143
37. Tang B, Shan L, Liang S, Zhou J (2019) Issues and opportunities facing aqueous zinc-ion batteries. Energy and Environmental Science 12:3288–3304. https://doi.org/10.1039/c9ee02526j
38. Zhang L, Chen L, Zhou X, Liu Z (2015) Towards High-Voltage Aqueous Metal-Ion Batteries Beyond 1.5 V: The Zinc/Zinc Hexacyanoferrate System. Advanced Energy Materials 5:1400930. https://doi.org/10.1002/aenm.201400930
39. Rodríguez-Hernández J, Reguera E, Lima E, et al (2007) An atypical coordination in hexacyanometallates: Structure and properties of hexagonal zinc phases. Journal of Physics and Chemistry of Solids 68:1630–1642. https://doi.org/10.1016/j.jpcs.2007.03.054
40. He B, Man P, Zhang Q, et al (2019) Conversion Synthesis of Self-Standing Potassium Zinc Hexacyanoferrate Arrays as Cathodes for High-Voltage Flexible Aqueous Rechargeable Sodium-Ion Batteries. Small 15:1905115. https://doi.org/10.1002/smll.201905115
41. Jassal V, Shanker U, Kaith BS, Shankar S (2015) Green synthesis of potassium zinc hexacyanoferrate nanocubes and their potential application in photocatalytic degradation of organic dyes. RSC Adv 5:26141–26149. https://doi.org/10.1039/C5RA03266K
42. Heo JW, Chae MS, Hyoung J, Hong S-T (2019) Rhombohedral Potassium–Zinc Hexacyanoferrate as a Cathode Material for Nonaqueous Potassium-Ion Batteries. Inorg Chem 58:3065–3072. https://doi.org/10.1021/acs.inorgchem.8b03081
43. Subramani K, Sathish M (2019) Facile synthesis of ZnO nanoflowers/reduced graphene oxide nanocomposite using zinc hexacyanoferrate for supercapacitor applications. Materials Letters 236:424–427. https://doi.org/10.1016/j.matlet.2018.10.111
44. Renman V, Ojwang DO, Valvo M, et al (2017) Structural-electrochemical relations in the aqueous copper hexacyanoferrate-zinc system examined by synchrotron X-ray diffraction. Journal of Power Sources 369:146–153. https://doi.org/10.1016/j.jpowsour.2017.09.079
45. Li W, Han C, Wang W, et al (2020) Stress Distortion Restraint to Boost the Sodium Ion Storage Performance of a Novel Binary Hexacyanoferrate. Advanced Energy Materials 10:1903006. https://doi.org/10.1002/aenm.201903006
46. Li, M.; Sciacca, R.; Maisuradze, M.; Aquilanti, G.; Plaisier, J.; Berrettoni, M.; Giorgetti, M. Electrochemical Performance of Manganese Hexacyanoferrate Cathode Material in Aqueous Zn-Ion Battery. Electrochimica Acta 2021, 139414. https://doi.org/10.1016/j.electacta.2021.139414.
47. Chen S-M, Chan C-M (2003) Preparation, characterization, and electrocatalytic properties of copper hexacyanoferrate film and bilayer film modified electrodes. Journal of Electroanalytical Chemistry 543:161–173. https://doi.org/10.1016/S0022-0728(03)00017-2
48. Rutkowska IA, Stroka J, Galus Z (2008) Electrochemical properties of modified copper–thallium hexacyanoferrate electrode in the presence of different univalent cations. Electrochimica Acta 53:3870–3878. https://doi.org/10.1016/j.electacta.2007.12.042
49. Bárcena Soto M, Scholz F (2002) The thermodynamics of the insertion electrochemistry of solid metal hexacyanometallates. Journal of Electroanalytical Chemistry 521:183–189. https://doi.org/10.1016/S0022-0728(02)00710-6
50. Scholz F, Dostal A (1996) The Formal Potentials of Solid Metal Hexacyanometalates. Angewandte Chemie International Edition in English 34:2685–2687. https://doi.org/10.1002/anie.199526851
51. Nightingale ER (1959) Phenomenological Theory of Ion Solvation. Effective Radii of Hydrated Ions. J Phys Chem 63:1381–1387. https://doi.org/10.1021/j150579a011
52. Wessells CD, Peddada SV, McDowell MT, et al (2011) The Effect of Insertion Species on Nanostructured Open Framework Hexacyanoferrate Battery Electrodes. J Electrochem Soc 159:A98. https://doi.org/10.1149/2.060202jes
53. Zhang L, Chen L, Zhou X, Liu Z (2015) Towards high-voltage aqueous metal-ion batteries beyond 1.5 V: The zinc/zinc hexacyanoferrate system. Advanced Energy Materials 5:1–5. https://doi.org/10.1002/aenm.201400930
54. Ni G, Han B, Li Q, et al (2016) Instability of Zinc Hexacyanoferrate Electrode in an Aqueous Environment: Redox-Induced Phase Transition, Compound Dissolution, and Inhibition. ChemElectroChem 3:798–804. https://doi.org/10.1002/celc.201500538
55. Zhang L, Chen L, Zhou X, Liu Z (2015) Morphology-Dependent Electrochemical Performance of Zinc Hexacyanoferrate Cathode for Zinc-Ion Battery. Sci Rep 5:18263. https://doi.org/10.1038/srep18263

Chapter 4

Systematic study of REEs intercalation

4.1 Introduction

Rare earth elements (REEs) have been acquired importance because of their wide range of applications, both in traditional and high-tech industries [1,2].Their global demand and consumption have been growing rapidly in conjunction with the developing of technological devices.

The European companies are mainly involved in manufacturing processes for semi-finished or finished products which contain REE like magnets, alloys, automotive catalysts, etc. (detailed in Table 4.1)

Table 4.6 Selected industrial activities in rare earth processing in Europe [3].

Country	**Products**
France	automotive catalysts, phosphors
Estonia	rare earth separation, rare earth metal production
Geramany	Magnet production
United Kingdom	Magnet production Alloys with rare earths
Netherlands	Magnet production

Austria	catalysts, glass polishing powder, glass fusion, pigments and ceramic glazes, pharmaceutical products

The uneasy mineral extraction, the increasing demand, the limited supplies and their location in some areas has led to innovative recovery processes, which in turn produces electronic wastes (e-waste). Such a waste can be considered a valuable end-of-life product containing REEs [4], which needs valorisation. Separation processes are essential both for the REEs extraction and recovery. Not only for the extraction process from an oxide mixture, but also for single REE separation by other metals in wastes. All the REEs are salt minerals in the earth soil as fluorocarbonates, phophates or fluorite minerals [5]. REEs are stable principally as trivalent cations and they show high affinity with oxygen. Although REEs are quite abundant, they are naturally concentrated, so the separation of them result a big challenge from an economic point of view. For this reason they are considered rare. Table 1 shows the metals crustal abundance (ppm) for the first time reported by Wdephol [6]. Noteworthy for the abundance of lanthanum for example is not rare at all.

Table 4.7 Abundance of metals in the Earth's crust.

Elements	**Symbol**	**Atomic number**	**Crustal Abundance (ppm)**
Nickel	Ni	28	90
Zinc	Zn	30	79
Copper	Cu	29	60
Cerium	Ce	58	60.0
Lanthanum	La	57	30.0
Cobalt	Co	27	30
Neodymium	Nd	60	27.0

Elements	Symbol	Atomic number	Crustal Abundance (ppm)
Yttrium	Y	39	24.0
Scandium	Sc	21	16.0
Lead	Pb	82	10
Praseodymium	Pr	59	6.7
Thorium	Th	90	6
Samarium	Sm	62	5.3
Gadolinium	Gd	64	4.0
Dysprosium	Dy	66	3.8
Tin	Sn	50	2.2
Erbium	Er	68	2.1
Ytterbium	Yb	70	2.0
Europium	Eu	63	1.3
Holmium	Ho	67	0.8
Therbium	Tb	65	0.7
Lutetium	Lu	71	0.4
Thullium	Tm	69	0.3
Silver	Ag	47	0.08
Gold	Au	79	0.0031
Promethium	Pm	61	10^{-18}

Furthermore, REEs have been divided into light (LREE) and heavy (HREE) rare earth elements (fig. 1), although Gd and Dy are sometimes classified as medium-weight lanthanides. The classification occurs on the basis of their trend in crustal abundance and the formation geological models [7].

The growing industrial applications of the rare earth elements (REE) led to a growing interest in the research of new technologies for separation and recovery of rare earths, as reported [8,9]. Particularly, lanthanum constitutes starting lighting igniction (SLI), digital camera, etc; dysprosium is essential in high power magnets and lasers; gadolinium is used as imaging contrast agent for NMR.

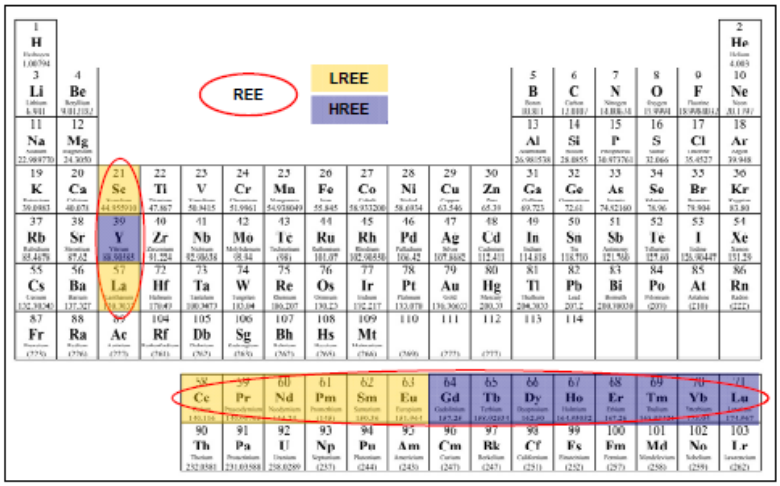

Figure 4.26 REEs in periodic table and their classification in LREEs and HREEs.

REEs appear as malleable and ductile soft metals which can be reactived at elevated temperature, while in aqueous solution they are in their trivalent state. Except for the atomic number and ionic radii, which are inversely correlated, the REEs chemical proprieties are very similar to each other.

Generally, hydrometallurgical techniques are the common methods for the metals recovery. The first step concerns alkali or acid leaching, followed by separation methods (e.g., liquid/liquid extraction), and, lastly, purification by adsorption (e.g., silica gel, activated carbon, zeolites etc.) or by ion-exchange processes [10].

Separation, purification, transport and sensing can occur through selective ligands which are able to coordinate REE ions. Several compounds as DOTA (dodecane tetraacetic acid), EDTA (acido etilendiamminotetraacetico), etc. have the capability to form complex with REEs in aqueous environments [11–13]. Also, Hydroquinoline derivatives (8-HR) are able to create coordination link useful for sensing, although the coordination system results very complex [14]. Another important feature is releted to the possibility to

achieve fuorescent sensor thanks to chemical reactions during the formation of complex. Examples of reaction-mediated sensors are reported [15,16]. Moreover, electrochemical sensors perform a very well response in terms of sensitivity and selectivity. The measurements can be very fast, repeatible and easy to perform, thanks to different techniques like CV (cyclic voltammetry), SWV (square wave voltammetry) and potentiometry. Brindley et al[17] reported the particular feature of Ferrocene derivatives using electrochemical techniques. The electrochemical response, during the redox processes, changes with the concentration of La(III), Lu(III) and Gd(III) linked to it. The anodic peaks shift was observed for all ligands, with an extent in terms of millivolts, depending to the ionic radius of the REE which creates a different polarization near the ferrocene unit.

The adsorption proprieties of MHCFs allow to purify water thanks to a solid/liquid extraction. In addition, they cointain one or more redox center (iron and sometimes transion metal linked), which allow to control by potentiodynamic processes their oxidation states. Finally, these compounds are easily synthetized on carbon active materials.

Thus, the fairly open with a cubic framework with large zeolite-like interstitial sites of MHCFs structure is able to easily accommodate ions during redox reactions, for electroneutrality purposes. Monovalent, divalent and trivalent cations can be involved. Hence, metal-hexacyanoferrates are suitable for the electrochemically switched ion exchange (ESIX) technique: the ion insertion/deinsertion can be regulated by the direct control of the redox states of the electroactive material; the facile electrosynthesis on conductive substrates allows to achieve the ion separation and the following regeneration of the film [18,19]. Therefore, ESIX is recently used in environmental applications, such as for the selective removal of radioactive Cs^{+} [20], or separation of Cu^{2+} [21], Ca^{2+} [22] and Ni^{2+} [23]. It is worth noting that the capability to intercalate a specific cation is influenced by changing metal sites in the lattice [24]. MHCFs can be excellent candidates for the separation of REEs by ion-

exchange, thanks to their electrochemical signature and peculiar structure[25].

Table A1 shows the ionic radii and lattice parameters of MHCFs which are studied as ionic sieve for REEs. As a matter of fact, metal substitution may lead to a changing in cell parameter and consequentely in the intercalation capabilities. All of the MHCFs showed in table 1 were already studied as ion exchanger of common mono, di and trivalent cations [20,26–33].

Table 4.8 Ionic radii and lattice parameters of NiHCF, CuHCF, CoHCF, CrHCF, InHCF [24,34,35].

Metals	r_m (Å)	Experimental Lattice parameter a_{obs} (Å)
Ni^{2+}	0.83	10.21
Cu^{2+}	0.87	10.12
Co^{2+}	0.89	10.28
Cr^{3+}	0.75	10.23
In^{3+}	0.80	10.51

4.2 Experimental

4.2.1 CuHCF film deposition

GCE working electrode pre-treatment consisted of cycling 20 times from 1.0 V to -0.2 V at 0.100 V s^{-1} in 1.0 M KNO_3. The electrodeposition was carried out at -0.80 V using a solution of 0.05 M $Cu(NO_3)_2$ and 0.1 M KNO_3 as supporting electrolyte for 20 seconds, then the electrode was rinsed and soaked in 1.0 × 10^{-3} M $K_3Fe(CN)_6$ and 0.1 M KNO_3 for 300 seconds at +0.6 V [30].

4.2.2 CoHCF film deposition

GCE working electrode pre-treatment consisted of cycling 20 times from 1.0 V to 0.0 V at 0.100 V s^{-1} in 1.0 M KNO_3. CoHCF film was deposited from a solution that contains 2.5 ×10^{-3} M $Co(NO)_2$, 2.5 ×

10^{-3} M $K_3Fe(CN)_6$, and 0.5 M KNO_3 as supporting electrolyte at native pH[36].

4.2.3 CrHCF film deposition

GCE working electrode pre-treatment consisted of cycling 20 times from 1.0 V to 0.0 V at 0.100 V s^{-1} in 1.0 M KNO_3. CrHCF film was deposited from a solution that contains 0.01 M $CrCl_3$, 0.002 M $K_3Fe(CN)_6$, and 0.1 M KCl as supporting electrolyte at pH ≈2[37].

4.2.4 InHCF film deposition

GCE working electrode pre-treatment consisted of cycling 20 times from 1.0 V to 0.0 V at 0.100 V s^{-1} in 1.0 M KNO_3. InHCF film was deposited from a solution that contains 5.0×10^{-3} M $InCl_3$, 5.0×10^{-3} M $K_3Fe(CN)_6$, and 0.1 M KCl as supporting electrolyte at pH ≈2[38].

Table 4.9 Schematic experimentals for thin film MHCFs electrodeposition

MHCF	$K_3Fe(CN)_6$	Metal salts	Support electrolyte	pH
CoHCF	2.5×10^{-3} M	2.5×10^{-3} M $Co(NO)_2$	$KNO_3$0.5M	native
CuHCF	1.0×10^{-3} M	0.05 M $Cu(NO)_3$	$KNO_3$0.1M	native
CrHCF	0.002 M	0.01 M $CrCl_3$	KCl 0.1M	2
InHCF	5.0×10^{-3} M	5.0×10^{-3} M $InCl_3$	KCl 0.1M	2
NiHCF	5.0×10^{-3} M	5.0×10^{-3} M $NiCl_2$	KCl 0.1M	native

All chemicals were reagent grade from Sigma-Aldrich® ($K_3Fe(CN)_6$, $Er(NO_3)_3$, $Co(NO)_2$), Alfa-Aesar ® ($InCl_3$,$Gd(NO_3)_3$, $La(NO_3)_3$, $Dy(NO_3)_3$), Merck ® (KNO_3), Carlo Erba reagents ® ($CrCl_3$), Baker reagents® (KCl) and Acros organics® $(Cu(NO)_3)_2$. All experiments have been performed in air, at room temperature, and with bi-deionized water.

4.2.5 Apparatus

Electrochemical measurements were performed by using a Model 730e (CH Instruments) electrochemical workstation and a standard three-electrode electrochemical glass cell (10 mL). The substrate

materials of working electrode were glassy carbon (diameter=3 mm). A Pt counter electrode was used.

All potentials were recorded vs. Ag/AgCl in saturated KCl. The glassy carbon (GC) electrode was polished with a 0.05 μm alumina slurry on a cloth and then rinsed with water.

4.2.6 Analysis procedure

The electrochemical behaviour in presence of different are earth cations was investigated by recording CVs in various supporting electrolytes following the protocol: firstly, a CV was recorded in a KCl 0.1 M, then a CV was recorded in other cations 0.1 M solution, finally, a last CV scan was repeated in 0.1 M KCl.

4.3 Results

CuHCF

Intercalation capability of CuHCF thin film was tested for four rare earth elements, in particular erbium, dysprosium, gadolinium and lanthanum, the stable CV shape proved the facile accommodation of each REE into the CuHCF lattice (Fig.4.2).

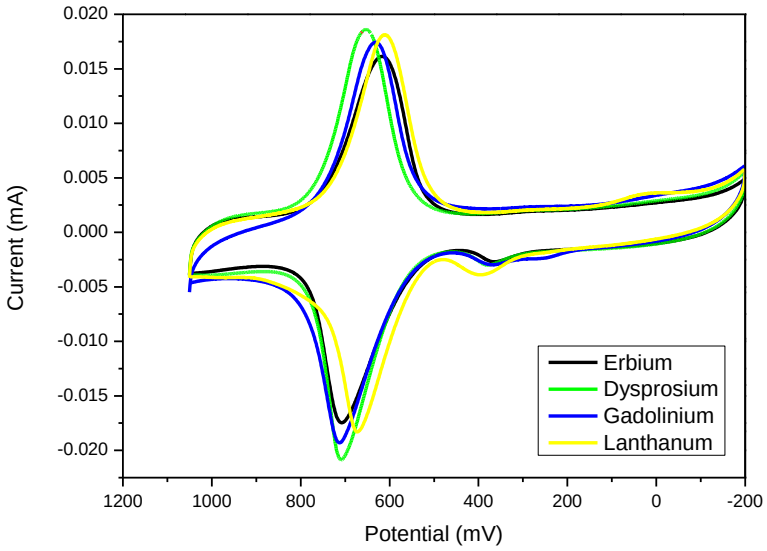

Figure 4.27 CVs of CuHCF recorded in $Er(NO_3)_3$, $Gd(NO_3)_3$, $La(NO_3)_3$, $Dy(NO_3)_3$. vs Ag/AgCl at 0.1 V s^{-1}

As well known, MHCFs are able to intercalate and release cations. Thus, CuHCF reversibility process was studied. The protocol described in experimental section was followed and it allowed to verify the intercalation and release of REE cations compared to K ions.

Indeed, all of the REE tested, showed a very well defined voltammogram, in which the potential shift is due to the variation of the cation accommodated into the lattice. The trivalent cation intercalations not occur a destabilization of the film, only a slight reduction of the current, as described in figure 4.3.

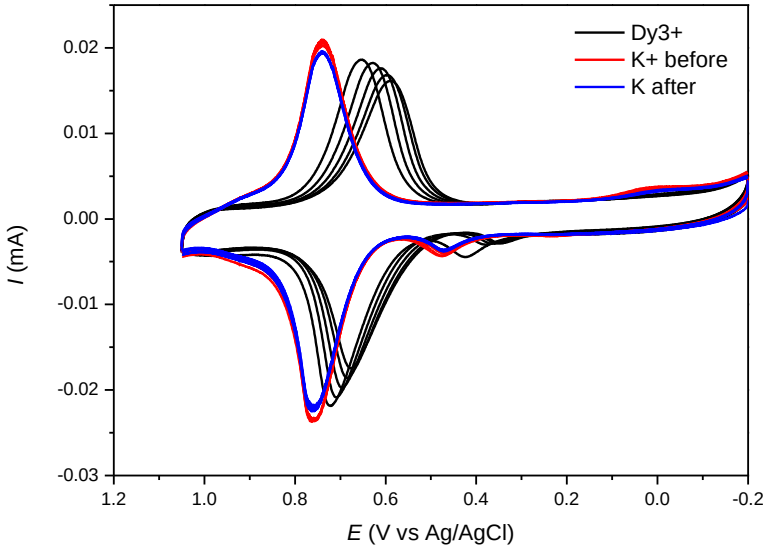

Figure 4.28 CVs at 0.1 V s-1 of a CuHCF film in 0.1 M KNO_3 and $Dy(NO_3)_3$ solutions at native pH

The panels in fig.4.4 show the CVs recorded in KNO_3 and in $Er(NO_3)_3$, $Gd(NO_3)_3$, $La(NO_3)_3$, $Dy(NO_3)_3$ respectively. The CV recorded in KNO_3 before and after the CV recorded in each REE, shows the same shape and potential shift, which indicate the CuHCF capability to intercalate the trivalent cations reversibly. The current intensity decreases slightly, because of the loss of electroactive material from the electrodes.

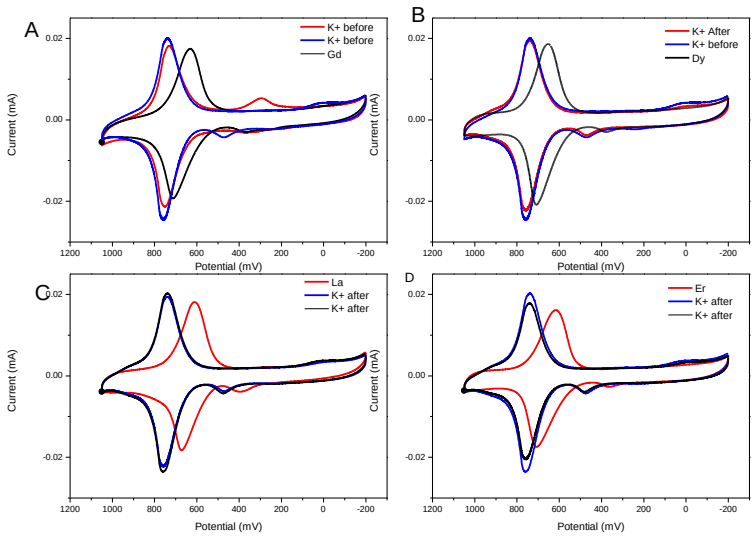

Figure 4.29 CVs of InHCF recorded in KNO_3, in REE and finally in KNO_3 vs Ag/AgCl at 0.1 V s^{-1}. (REE= $Dy(NO_3)_3$ (A), $Gd(NO_3)_3$ (B), $Er(NO_3)_3$ (C), $La(NO_3)_3$ (D)).

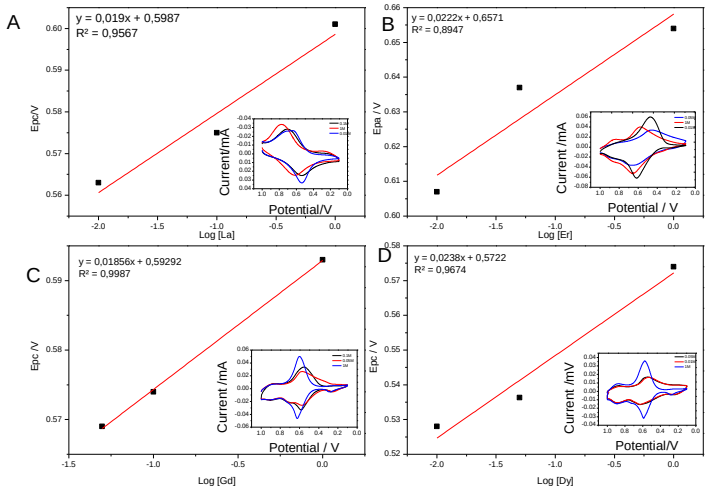

Figure 4.30 Potential (V) vs Log [REE] ((REE= $La(NO_3)_3$(A),$Gd(NO_3)_3$ (B), $Er(NO_3)_3$ (C) $Dy(NO_3)_3$ (D)). - Inset: CVs recorded at several [REE] vs Ag/AgCl at 0.1 V s^{-1}

The same CuHCF film was studied in several concentration of each REE, its behaviour is described by the following redox reaction:

$$Cu_3[Fe^{III}(CN)_6]_2 + 1/3\ A^{3+} + e^- \rightleftarrows A_{1/3}[Cu_3Fe^{II}(CN)_6]_2 \qquad (1)$$

The intercalation of A, which can be on between Dy^{3+}, Er^{3+}, La^{3+} or Gd^{3+}, leads to a controlled potential shift with the variation of its concentration, operated by Nerst equation:

$$\mathbf{E = k + \left(\frac{0.059}{3} \log [A^{3+}]\right)} \qquad (2)$$

Thus, the theoretical slope must be near to 19 mV and similar values are evaluated from the experimental data for each REE (Fig.4.5).

CrHCF

CrHCF was tested because of the chromium abundance.

CrHCF thin film was electrodeposited on GCE and studied in different REEs.

The voltammograms recorded show a clear redox couple at about 0.60/0.65 V. The shapes and the peak positions are so similar that is difficult to tell them apart (Fig.4.6).

As described for other MHCFs, CrHCF is able to intercalate cations into the lattice, through the redox reaction (3).

$$Cr[Fe^{III}(CN)_6] + 1/3\ A^{3+} + e^- \rightleftarrows A_{1/3}[CrFe^{II}(CN)_6] \qquad (3)$$

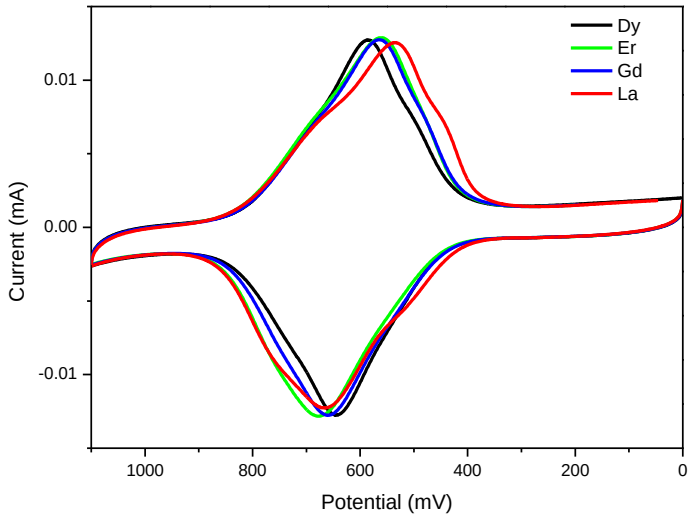

Figure 4.31 CVs of CrHCF recorded in $Er(NO_3)_3$, $Gd(NO_3)_3$, $La(NO_3)_3$, $Dy(NO_3)_3$. vs Ag/AgCl at 0.1 V s^{-1}

The potential shift, caused by the intercalation/deintercalation of the REE, was evaluated at higher potential than in KNO_3, expect for lanthanum. It caused a wide peak without symmetry of cathodic and anodic peaks, that can be related to the kinetic control of the process.

In all cases the reversibility was checked: the uptake/release of REEs happen if compared to potassium ions (fig. 4.7)

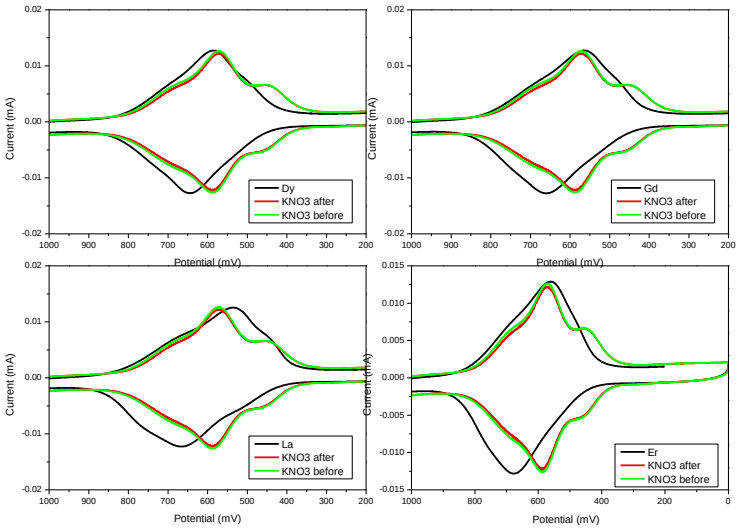

Figure 4.32 CVs of CrHCF recorded in KNO_3, in REE and finally in KNO_3 vs Ag/AgCl at 0.1 V s^{-1}. (REE= $Dy(NO_3)_3$ (A), $Gd(NO_3)_3$ (B), $La(NO_3)_3$ (C), $Er(NO_3)_3$ (D).

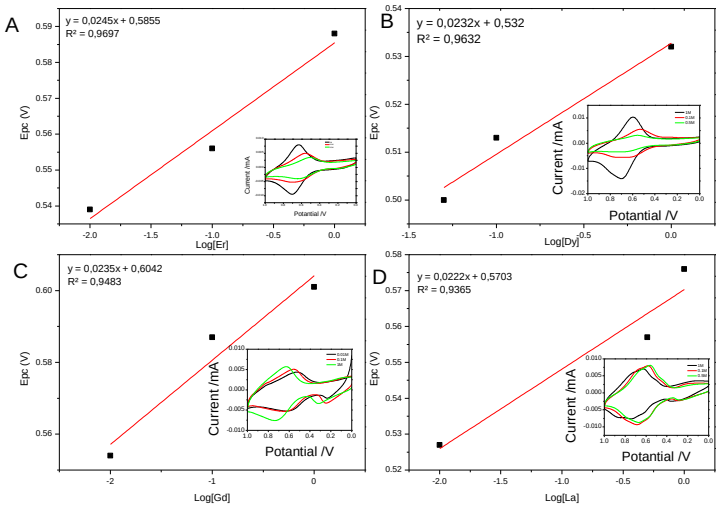

Figure 4.33 CVs of CrHCF recorded in KNO_3, in REE and finally in KNO_3 vs Ag/AgCl at 0.1 V s^{-1}. (REE= $Er(NO_3)_3$ (A), $Dy(NO_3)_3$ (B), $Gd(NO_3)_3$ (C), $La(NO_3)_3$ (D)).

As well as for CuHCF, CrHCF shows a nerstian behaviour, showing slopes near to 22mV, close to the theoretical one (Eq. 2).

CoHCF

CoHCF CVs recorder in different REEs (Fig.4.9) show a similar behaviour with the couple peak potential near to 0.55/0.7 V. The peaks appear widely and similar each other.

$$Co_3[Fe^{III}(CN)_6]_2 + 1/3\ A^{3+} + e^- \rightleftarrows A_{1/3}Co_3[Fe^{II}(CN)_6]_2 \qquad (5)$$

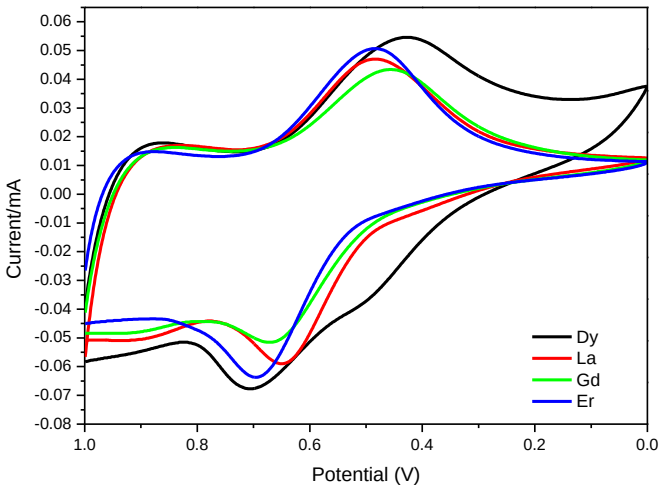

Figure 4.34 CVs of CoHCF recorded in $Er(NO_3)_3$, $Gd(NO_3)_3$, $La(NO_3)_3$, $Dy(NO_3)_3$. vs Ag/AgCl at 0.1 V s^{-1}

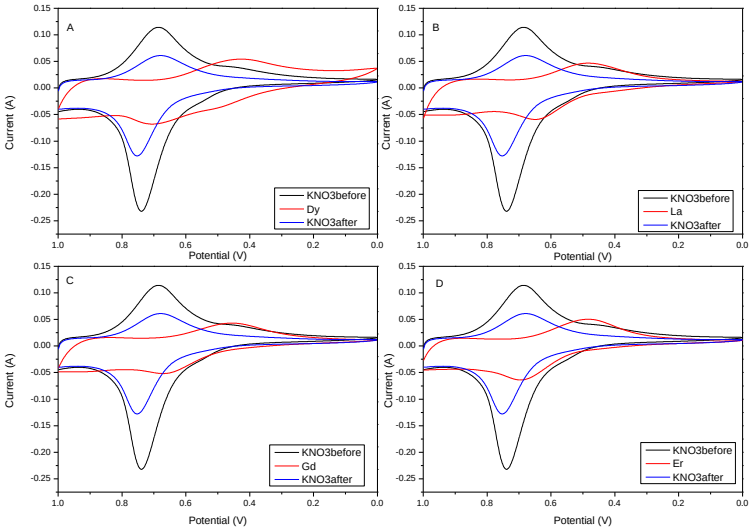

Figure 4.35 CVs of CoHCF recorded in KNO_3, in REE and finally in KNO_3 vs Ag/AgCl at 0.1 V s-1. (REE= $Dy(NO_3)_3$ (A), $La(NO_3)_3$ (B), $Gd(NO_3)_3$ (C), $Er(NO_3)_3$ (D)).

The reversible ability of the CoHCF to intercalate and de-intercalate the REEs is showed in figure 4.10, where it is possible highlight the considerable decrease of the current intensity from during the K^+ intercalation after the REEs one.

Finally, CoHCF shows a nerstian behaviour, the slopes calculated by the following experimental data are ca. 25 mV, close to theoretical one.

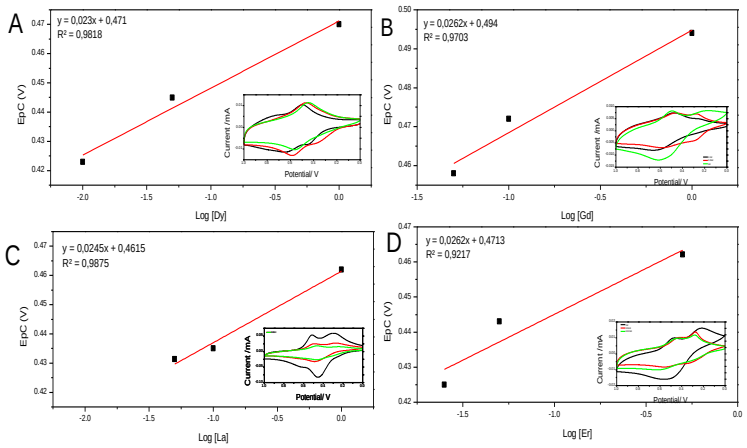

Figure 4.36 Potential (V) vs Log [REE] (REE= $Dy(NO_3)_3$ (A), $Gd(NO_3)_3$ (B), $La(NO_3)_3$ (C), $Er(NO_3)_3$ (D)). – Inset: CVs recorded at several [REE] vs Ag/AgCl at 0.1 V s^{-1}

InHCF

Indium hexacyanoferrate (InHCF) shows a particular behaviour when intercalates REEs, because no nerstian behaviour was evaluated, mainly because of the instability of the voltammograms in low concentration of support electrolytes.

Even though, a well-defined CV in REEs 0.1 M was recorded, which indicates the InHCF capability to host REEs into the lattice (fig. 12). The CV shapes of InHCF film in Er^{3+}, La^{3+}, Gd^{3+} and Dy^{3+} result very similar and the potential shifting are very close each other. It is not possible recognized the REE intercalated trough the CV shape.

Generally, as for other MHCFs, the redox reaction which involve during the insertion and de-insertion processes is the following:

$$In^{III}[Fe^{III}(CN)_6]_2 + 1/3\ A^{3+} + e^- \rightleftarrows A_{0.33}[In^{III}\ Fe^{II}(CN)_6]_2 \qquad (6)$$

InHCF may show a nerstian behaviour, with a linear slope of 19 mV ca.. Despite of the other MHCF tested, InHCF did not show a good stability al low concentration of support electrolytes.

Several reasons can justify this behaviour. One of that could be the characteristic of Indium. For example, it is a trivalent cation, despite of Co or Cu already tested, so the third charge can influence its behaviour during the intercalation process, even though the intercalation of trivalent cations was reported [38].

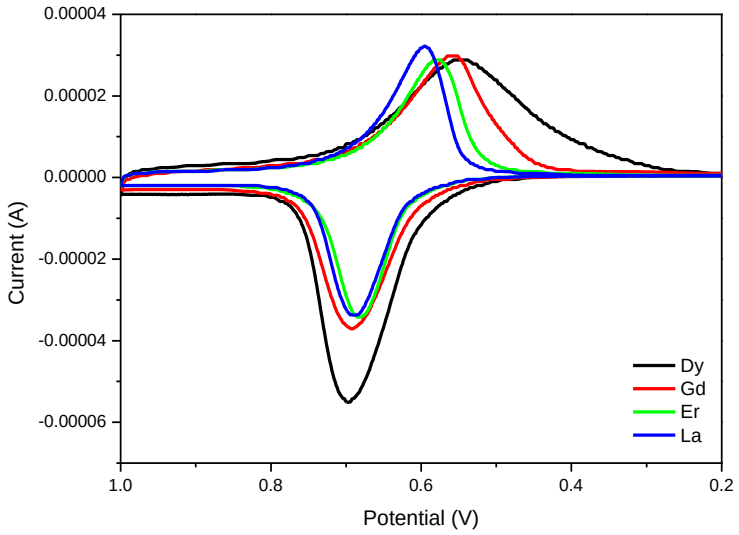

Figure 4.37 CVs of InHCF recorded in 0.1M $Er(NO_3)_3$, $Gd(NO_3)_3$, $La(NO_3)_3$, $Dy(NO_3)_3$. vs Ag/AgCl at 0.1 V s^{-1}

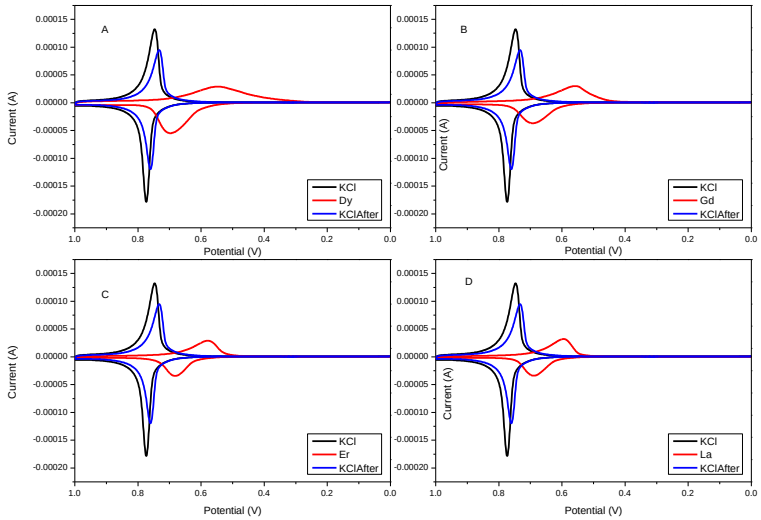

Figure 4.38 CVs of InHCF recorded in KNO_3, in REE and finally in KNO_3 vs Ag/AgCl at 0.1 V s^{-1}. (REE= $Dy(NO_3)_3$ (A), $Gd(NO_3)_3$ (B), $Er(NO_3)_3$ (C), $La(NO_3)_3$ (D)).

Ionic radii influences

Table 4.10 Electronic configuration and ionic radii of lanthanum, gadolinium, dysprosium and erbium.

Element	**La**	**Gd**	**Dy**	**Er**
Configuration	$5d^1\ 6s^2$	$4f^7\ 5d^1\ 6s^2$	$4f^{10}\ 6s^2$	$4f^{12}\ 6s^2$
Ionic Radii (pm)	106.1	93.8	91.2	89

As a matter of fact, the intercalation of the REEs tested is influenced by the lattice composition and the dimensions of each REE. In particular, except for InHCF, all of the MHCFs tested show the reversible capability to intercalate easily lanthanum, gadolinium, dysprosium and erbium. This behaviour is probably due to the dimensions of lattice which are very similar (table 4.5). Dissimilar

dimension of InHCF could influence the intercalation of these cations, which caused the film instability.

Also the lattice parameter, which changes during the oxidation and reduction, could influences the intercalation processes as already reported by Asai et al. [24].

Selective recovery of REEs

Among the metal hexacyanoferrates, nickel hexacyanoferrate (NiHCF) and copper hexacyanoferrate (CuHCF) are excellent candidates for cation extractions [20,26–29]. Ciabocco *et al.* [31] showed the NiHCF capability to easily intercalate trivalent cations as well as monovalent cations. The ions exchange capabilities of CuHCF were also highligthed [30].

Herein, we report evidence of an unprecedent selectivity of NiHCF and CuHCF for rare earth elements. The outcome suggests an exclusive selectivity for REEs depending on the MHCF.

The proposed procedure is focused on the selective separation of REEs through a very simple process and consisting in a loop of two electrochemical steps. The CuHCF and NiHCF electrochemical sorption capabilities for different rare earth cations were conducted

by

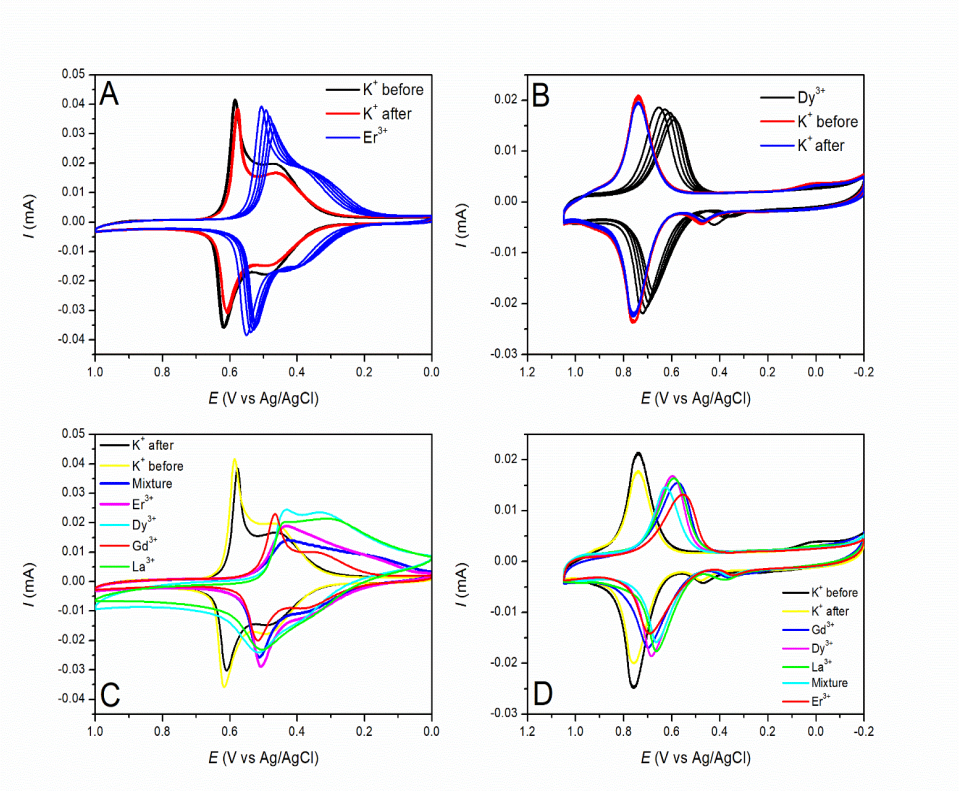

Figure 4.39 CVs at 0.1 V s-1 of A) of a NiHCF film in 0.1 M KNO_3 and $Er(NO_3)_3$ solutions at native pH; B) of a CuHCF film in 0.1 M KNO_3 and $Dy(NO_3)_3$ solutions at native pH; C) NiHCF and D) CuHCF film in 0.1 M KNO_3, $RE(NO_3)_3$ (RE=La, Dy, Gd, Er)

using a precise protocol [38] . The protocol allowed the potassium - rare-earth replacement estimation and, in the last step, the evaluation of the reversibility of the process. The procedure was applied to several rare earth elements cations, namely, La^{3+}, Gd^{3+}, Dy^{3+} and Er^{3+}, representing light-group rare-earth "LREE" and heavy-group rare-earth "HREE" elements

Figure 14A shows the reversibility process toward to the trivalent erbium in NiHCF film. The CV signature is characterised by two predominant species that can be assigned to $K_2Ni^{II}[Fe^{II}(CN)_6]$ and $KNi^{II}_{1.5}[Fe^{II}(CN)_6]$ [39].

This electrochemical system shifts of about 100 mV depending of the ion accomodated into the structure. When Er^{3+} is inserted there is a positive shift respect to K^+ at the initial stage. This underlined the electrochemical driven sorption&release of ions into the structure. It is seen that the first 10 cycles recorded in KNO_3 (black line) are almost coincident with the last (red line) recorded after performing

10 cycles in a solution containing Er^{3+} cations (blue line); thus confirming the perfect cation exchange reversibility. Also, the release of erbium is faster than the uptake of potassium, as shown in Fig.14A. As a matter of fact, the potential shift related to the CVs recorded in erbium highlights the different kinetic control for the release/uptake of the cations. Furthermore, the perfect cation exchage reversibility is confirmed for all the investigated cations, as well. By analogy, but using Dy^{3+}, figure 14B shows 10 CVs of CuHCF recorded in potassium nitrate before (red line) and after (blue line) the test in dysprosium nitrate (black line). This polarization curve displays one main process at ca. +0.8 V vs. SCE, which is due to the $KCu^{II}[Fe^{III}(CN)_6]_2$/ $K_2Cu^{II}[Fe^{II}(CN)_6]_2$ couple **[30]**. Once again, there is a peak potential dependency to the inserted ion, at first. In addition, the complete overlapping of the CVs recorded in K^+, underlines the reversibility of the process. The voltammogram in $Dy(NO_3)_3$ reaches a potential stability in 4 cycles, slower than in K^+. Therefore, this electrochemical behavior makes the CuHCF potentially useful for REE sorption and release, using a different ion. This feature, together with the perfect electrochemical reversibility, confirmed by the absence of any substitution of Ni or Fe, is a basic requirement in order to test these devices as selective molecular sieves.

Furthermore, the dependence of CVs upon the concentration were studied for each rare-earth cation in the $1.0 - 1.0\times10^{-2}$ M range in order to assess the role of the rare earth cation in the electrochemical process. The replacement of K^+ ions with another cation causes substantial changes in the peak shape and position, as already pointed out. The peak potentials shift can be related to the radius of the hydrated cation, as has been noted previously for other Prussian Blue type of compounds **[38]** or to the ionic potential (ratio of ionic charge to radius) as reported by Scholz et *al.***[40]**. The redox mechanism involves the rare earth cations insertion during reduction and its release during oxidation, in according with the following redox reactions:

$Ni_{1.5}[Fe^{III}(CN)_6] + 1/3\ A^{3+} + e^- \rightleftarrows A_{1/3}[Ni_{1.5}Fe^{II}(CN)_6]$ (7)

$Cu_3[Fe^{III}(CN)_6]_2 + 1/3\ A^{3+} + e^- \rightleftarrows A_{1/3}[Cu_3Fe^{II}(CN)_6]_2$ (8)

The Nernst equation for reactions (7) and (8) reads (in volts):

$$\mathbf{E = k + \left(\frac{0.059}{3}\ log\ [A^{3+}]\right)} \quad (2)$$

Where A is one of the rare earth ions between erbium, lanthanum, dysprosium, and gadolinium.

We confirm equation (7) and (8) as the insertion/de-insertion mechanism of the tested rare earth elements, being the Nerstian slope values very close to 19 mV. This is a consequence of the zeolitic structure of the MHCF characterized by open channels whose chemical-physical characteristics constitute the driving force for ion discrimination: the nature and the size of the ion are the limiting factors in order to be inserted into the structure.

Figure 14C reports the CVs of NiHCF films in 0.1 M $La(NO_3)_3$, $Gd(NO_3)_3$, $Dy(NO_3)_3$ and $Er(NO_3)_3$ solutions at 0.1 V s^{-1} and in a mixture containing all the investigated rare earth elements. Even though, the peak position and the overall shape depend on the nature of rare earth cations, as evidenced above, it is worth noting the perfect analogy between the CV in the solution containing the Er^{3+} alone and in the mixture containing all the rare earth elements, for the NiHCF case. This fact suggests an exclusive selectivity of NiHCF toward to a specific cation, i.e. the Er^{3+}.

Figure 14D reports the CVs of CuHCF films in 0.1 M $La(NO_3)_3$, $Gd(NO_3)_3$, $Dy(NO_3)_3$ and $Er(NO_3)_3$ solutions at 0.1 V s^{-1} and in a mixture containing all the investigated rare earth elements. Unlike NiHCF, the CV of each RE cation is very similar to the others, so a possible analogy between the mixture and one of the REE tested, is not easily identified. Though, the oxidation peak potential in mixture is very close to the Lanthanum one (ca. +0.67 V).

To verify the above hypothesis, MP-AES analysis were carried out on the solutions after the REE releasing, during the restoring step. NiHCF is confirmed to not only uptake erbium, as suggested from the CVs, but also dysprosium. The binary selectivity can be due to the similarity of erbium and dysprosium, which belong to the class

of “heavy rare earth elements”. Concerning CuHCF, even though a REE selectivity order cannnot be anticipated based on CV results, the MP-AES analysis indicated the presence of dysprosium and lanthanum. Lanthanum belongs to the “light rare earth elements” class and the ionic radii is bigger than the other REES tested; therefore CuHCF can preferentially select it. These data must be improved, using other techniques.

Kinetic behaviour during the exchange process K/REE of NiHCF film

In order to optimize experimental parameters of the REEs extraction/separation procedure thank to a NiHCF thin film-modified electrode, an EFA (Evolving factor analysis) technique was used. The REEs extraction/separation procedure is based on an exchange process, in which K+ was exchanged by REE and afterward a REE was released and insertion of K+ occurs again. A voltammograms sequence was carried out:

30 cycles in KNO_3

30 cycles in REE mixture (uptake di RE)

30 cycles in KNO_3

30 cycles in REE mixture (uptake di RE)

30 cycles in KNO_3

30 cycles in REE mixture (uptake di RE)

Furthermore, 180 cycles in KNO_3 were recorded as background. The whole of 180 cycles was analysed by the EFA technique by the

The Unscrambler X version 10.2 2009-2012, CAMO softwares.

EFA technique allows to define the presence of several species and their evolution (in terms of concentration), changing one or more parameters, providing the mass balance conservation (close condition). For our aim, the close condition occurs when the total

charge keeps constant, namely the same amount of electrode material reacts during the process and the external parameter variation corresponds to the cycles recorded.

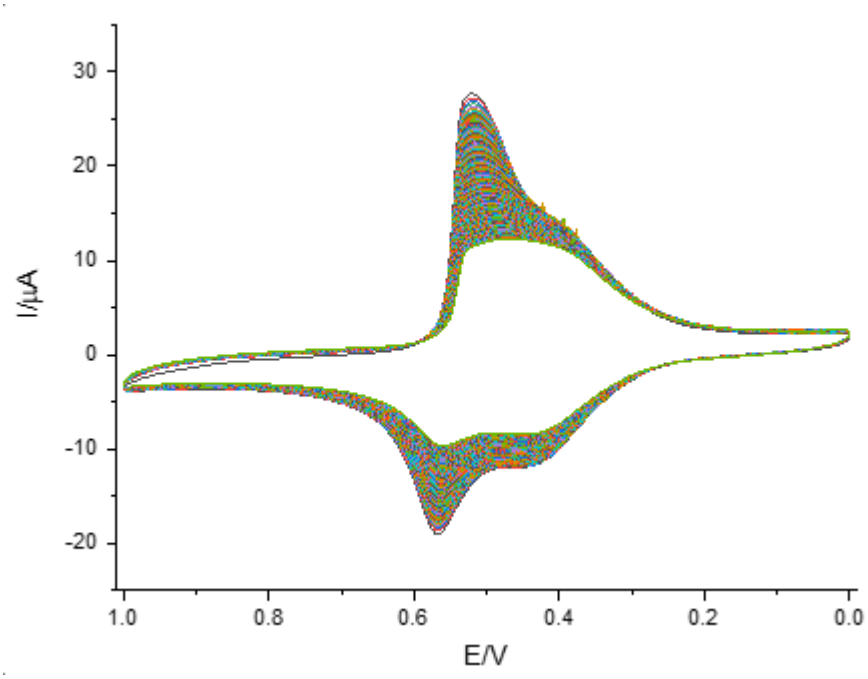

Figure 4.40. 180 cycles of NiHCF film in KNO_3

Fig. 4.15 show the overlapping of 180 cycles of the NiHCF modified electrode in KNO_3: the voltammograms morphology changes with the increasing of cycles number. Some considerations must be done:

1. the decreasing of the single cycle charge value: the total amount of the electroactive amount decreases with the time because of the mechanical loss of the electroactive material.
2. The voltammograms shape variation: during the progression of the cycles recorded, on one hand the peak intensity at ca 0.55V decreases on the other hand the peak intensity at ca. 0.4V increases

To avoid the problem due to the loss of the electroactive material and to maintain the close condition, the voltammograms were normalized considering the charge as constant. We report only the cathodic process of the voltammograms for clarity. Figure 4.16 reports the 180 voltammograms afterward the normalizing process.

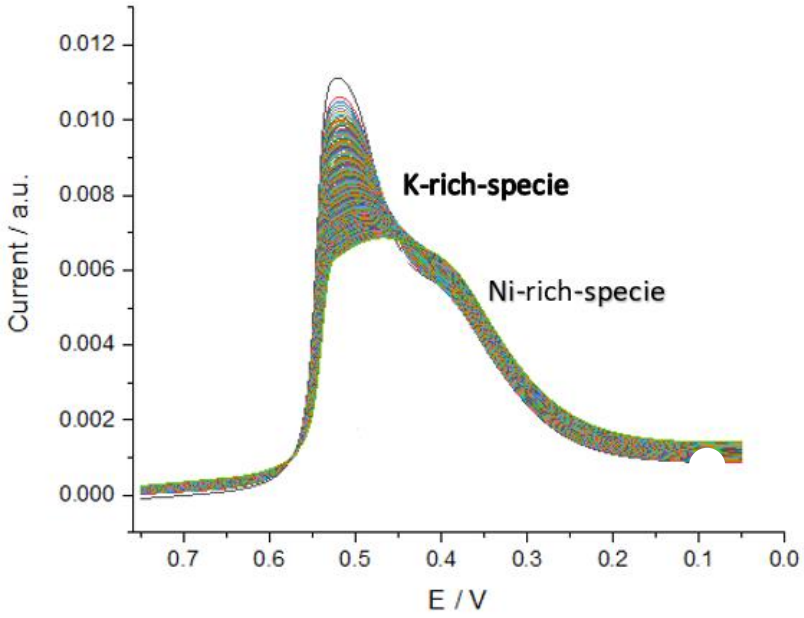

Figure 4.41. Cathodic voltammograms overlapping cycle 1-180 after charge normalization.

The absence of a clear isosbestic point, although detectable, is due to the normalization on the charge of the whole cathodic span. The morphological evolution of the voltammograms indicates the progressive changing from the K-rich-specie to the Ni one [39]. This particular characteristic is confirmed by the calculated concentration obtained from the EFA analysis (Fig. 4.17).

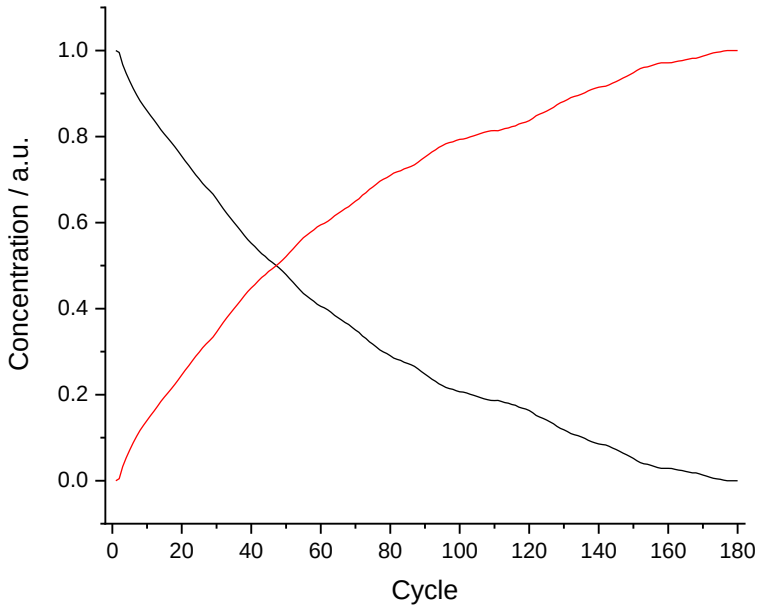

Figure 4.42. Calculated concentrations profiles of Ni-rich-specie (red) and K-rich-specie (black).

Then, the 180 cycles of REEs extraction procedure were analysed. In figure 4.18 the overlapped and charge normalized cathodic CVs (in total 180 cycles) were reported.

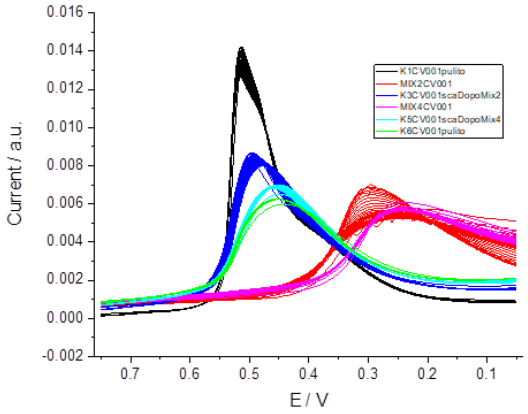

Figure 4.43. Overlapped cathodic voltammograms, charge normalized. The six phases are marked by different colours (detailed in the legend).

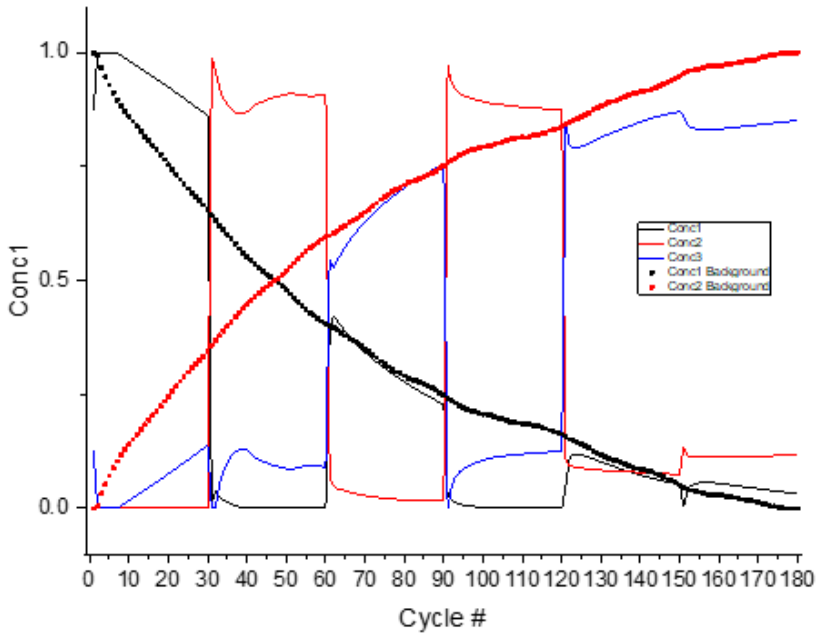

Figure 4.44. Concentration profiles calculated fixing 3 species. The dot curves show the overlapping of the K-rich-NiHCF (red), Ni-rich-NiHCF (black) obtained by the 180 cycles in KNO_3 elaboration.

The gradual increase of the number of the cycles leads to an evolution of the peaks morphology according to the NiHCF behaviour in KNO_3 examined above. The CVs recorded in the mixture of REEs, after the first cycles, the morphology of the voltammograms remains constant. The concentration profiles reported in figure 4.19 were calculated by EFA, fixing three species: K-rich-NiHCF, Ni-rich-NiHCF, the NiHCF containing REEs. To this elaboration data was overlapped the curves obtained from the background elaboration (dot curves).

The detailed analysis of figure 4.19, highlights six different steps:

- 1^{st} Step (cycles 1-30) in KNO_3

In the first 30 cycles there are only two species: the K-rich-specie (black line- curve 1), majority specie, and Ni-rich specie (blue line - curve 2).

- 2^{nd} Step (cycles 31-60) in REEs mixture

Starting from the 31st cycle appear a new specie (red line- curve 3) and at the same time disappear the curves 1 and 2 almost completely. The curve 3 shows some fluctuation before the stationary state.

- 3rd Step (cycles 61-90) in KNO_3

The curve 3 decays immediately to zero, which means that only two cycles are enough for the REEs releasing and the re-uptake of K^+. The intensity of curves 1 and 2 are reversed.

- 4th Step (cycles 91-120) in REEs mixture

The situation is analogous to the one described in the 3rd step.

- 5th Step (cycles 121-150) in KNO_3

The curve 3 decays immediately to zero, therefore the releasing of REEs occurs, while the curve 1 still decreases and the curve 2 still increases.

- 6th Step (cycles 161-180) in KNO_3

Here a stabilization of the curve 1 (decreasing) and curve 2 (increasing) occurs.

It worth noting that the evolution of the curves 1 and 2 is the same behaviour of the film in KNO_3 during the 180 cycles recorded, with a perfect overlapping of the dot curves.

Therefore, the kinetic behaviour of NiHCF release of REEs occurs faster than their uptake, related to K ions.

4.5. Conclusion

In conclusion, we demonstrated the reversible uptake and release of several REEs into/from different hexacyanoferrate lattices. Also, the intercalation of REEs results different from the deintercalation process from a kinetic point of view. Finally, the nerstian behaviour was tested, as well.

Finnaly, we also demonstrate the uptake and release capability of two films of metal hexacyanoferrate electrodes for the sorption of REEs. Interestingly, the EFA analysis shows the kinetic behaviour of NiHCF confirming the CVs results: the release of REEs from the lattice occurs faster than the uptake process, leading the NiHCF film to be a facile way for REEs recovery. Despite of the co-precipitation methods, the proposed electrochemical one is also facile, reproducible and fast (few minutes).

References

1 M. A. Alam, L. Zuga and M. G. Pecht, *Ceramics International*, 2012, **38**, 6091–6098.

2 X. Du and T. E. Graedel, *Environ. Sci. Technol.*, 2011, **45**, 4096–4101.

3 Schüler, Doris, et al, *Öko-Institut eV Darmstadt*, 2011, **49**, 30–40.

4 Q. Tan and J. Li, in *Waste Electrical and Electronic Equipment (WEEE) Handbook (Second Edition)*, eds. V. Goodship, A. Stevels and J. Huisman, Woodhead Publishing, 2019, pp. 393–421.

5 H. Öztürk, S. Altuncu, N. Hanilçi, C. Kasapçı and K. M. Goodenough, *Ore Geology Reviews*, 2019, **105**, 423–444.

6 K. Hans Wedepohl, *Geochimica et Cosmochimica Acta*, 1995, **59**, 1217–1232.

7 D. Paderni, L. Giorgi, V. Fusi, M. Formica, G. Ambrosi and M. Micheloni, *Coordination Chemistry Reviews*, 2021, **429**, 213639.

8 A. Amato, A. Becci, I. Birloaga, I. De Michelis, F. Ferella, V. Innocenzi, N. M. Ippolito, C. Pillar Jimenez Gomez, F. Vegliò and F. Beolchini, *Renewable and Sustainable Energy Reviews*, 2019, **106**, 41–53.

9 W. Zhang and R. Q. Honaker, *International Journal of Coal Geology*, 2018, **195**, 189–199.

10 R. K. Jyothi, T. Thenepalli, J. W. Ahn, P. K. Parhi, K. W. Chung and J.-Y. Lee, *Journal of Cleaner Production*, 2020, **267**, 122048.

11 C. Benelli, E. Borgogelli, M. Formica, V. Fusi, L. Giorgi, E. Macedi, M. Micheloni, P. Paoli and P. Rossi, *Dalton Trans.*, 2013, **42**, 5848.

12 S. Amatori, G. Ambrosi, M. Fanelli, M. Formica, V. Fusi, L. Giorgi, E. Macedi, M. Micheloni, P. Paoli and P. Rossi, *Chem. Eur. J.*, 2014, **20**, 11048–11057.

13 P. Rossi, S. Ciattini, M. Formica, V. Fusi, L. Giorgi, E. Macedi, M. Micheloni and P. Paoli, *Inorganica Chimica Acta*, 2018, **470**, 254–262.

14 R. Akbar, M. Baral and B. K. Kanungo, *Spectrochimica Acta Part A: Molecular and Biomolecular Spectroscopy*, 2014, **129**, 365–376.

15 B. S. Lukyanov and M. B. Lukyanova, *Chem Heterocycl Compd*, 2005, **41**, 281–311.

16 Z. Liu, L. Jiang, Z. Liang and Y. Gao, *Tetrahedron*, 2006, **62**, 3214–3220.

17 G. D. Brindley, O. D. Fox and P. D. Beer, *J. Chem. Soc., Dalton Trans.*, 2000, 4354–4359.

18 A. F. Tawfic, S. E. Dickson, Y. Kim, W. Mekky, M. Gobara and A. Baraka, *J Solid State Electrochem*, 2017, **21**, 2939–2946.

19 M. A. Lilga, R. J. Orth, J. P. H. Sukamto, S. D. Rassat, J. D. Genders and R. Gopal, *Separation and Purification Technology*, 2001, **24**, 451–466.

20 R. Chen, H. Tanaka, T. Kawamoto, M. Asai, C. Fukushima, H. Na, M. Kurihara, M. Watanabe, M. Arisaka and T. Nankawa, *Electrochimica Acta*, 2013, **87**, 119–125.

21 F. Gao, X. Du, X. Hao, S. Li, X. An, M. Liu, N. Han, T. Wang and G. Guan, *Chemical Engineering Journal*, 2017, **328**, 293–303.

22 C. Weidlich and K.-M. Mangold, *Electrochimica Acta*, 2011, **56**, 3481–3484.

23 Z. Wang, Y. Feng, X. Hao, W. Huang and X. Feng, *Journal of Materials Chemistry A*, 2014, **2**, 10263–10272.

24 M. Asai, A. Takahashi, K. Tajima, H. Tanaka, M. Ishizaki, M. Kurihara and T. Kawamoto, *RSC Adv.*, 2018, **8**, 37356–37364.

25 M. Berrettoni, A. Mullaliu and M. Giorgetti, in *Green Adsorbents to Remove Metals, Dyes and Boron from Polluted Water*, eds. Inamuddin, M. I. Ahamed, E. Lichtfouse and A. M. Asiri, Springer International Publishing, Cham, 2021, pp. 171–194.

26 M. Giorgetti, E. Scavetta, M. Berrettoni and D. Tonelli, *Analyst*, 2001, **126**, 2168–2171.

27 S. D. Rassat, J. H. Sukamto, R. J. Orth, M. A. Lilga and R. T. Hallen, *Separation and Purification Technology*, 1999, **15**, 207–222.

28 M. Pyrasch, A. Toutianoush, W. Jin, J. Schnepf and B. Tieke, *Chem. Mater.*, 2003, **15**, 245–254.

29 R. Chen, H. Tanaka, T. Kawamoto, M. Asai, C. Fukushima, M. Kurihara, M. Ishizaki, M. Watanabe, M. Arisaka and T. Nankawa, *ACS Appl. Mater. Interfaces*, 2013, **5**, 12984–12990.

30 M. Ventura, A. Mullaliu, D. E. Ciurduc, S. Zappoli, G. Giuli, D. Tonti, E. Enciso and M. Giorgetti, *Journal of Electroanalytical Chemistry*, 2018, **827**, 10–20.

31 M. Ciabocco, M. Berrettoni, and Zamponi, Silvia, *Int. J. Electrochem. Sci.*, 2018, 5535–5551.

32 P. J. Kulesza, M. A. Malik, M. Berrettoni, M. Giorgetti, S. Zamponi, R. Schmidt and R. Marassi, *J. Phys. Chem. B*, 1998, **102**, 1870–1876.

33 R. P. Singh and E. R. Pambid, *Analyst*, 1990, **115**, 301–304.

34 L. Chen, H. Shao, X. Zhou, G. Liu, J. Jiang and Z. Liu, *Nat Commun*, 2016, **7**, 11982.

35 D. Baster, E. Oveisi, P. Mettraux, S. Agrawal and H. H. Girault, *Chem. Commun.*, 2019, **55**, 14633–14636.

36 M. Ciabocco, M. Berrettoni, S. Zamponi and J. A. Cox, *J Solid State Electrochem*, 2016, **20**, 1323–1329.

37 R. Bors, J. Yun, P. Marzak, J. Fichtner, D. Scieszka and A. S. Bandarenka, *ACS Omega*, 2018, **3**, 5111–5115.

38 M. Ciabocco, M. Berrettoni, S. Zamponi, J. A. Cox and S. Marini, *J Solid State Electrochem*, 2013, **17**, 2445–2452.

39 S. Zamponi, M. Berrettoni, P. J. Kulesza, K. Miecznikowski, M. A. Malik, O. Makowski and R. Marassi, *Electrochimica Acta*, 2003, **48**, 4261–4269.

40 F. Scholz and A. Dostal, *Angewandte Chemie International Edition in English*, 1996, **34**, 2685–2687.

Appendix A

Green rust electrochemical characterization

A Introduction

A.1. Iron Corrosion process

Atmospheric corrosion of steel has been widely investigated [1–3], in order to prevent the process. On the other hand, iron corrosion is a crucial problem in the conservation of iron artifacts in the fields of cultural heritage. In fact, the iron products are usually recovered already with the formation of rust, therefore the removal of corrosion products and an adequate treatment must be applied to the iron products to stop or slow down the corrosion process. [4, 5]. However, the corrosion process that takes place is due to the oxygen and water (also humidity) action, as described in the following reactions[6]:

$$Fe \rightarrow Fe^{2+} + 2e^{-} \quad (1)$$

both in neutral/basic solutions:

$$½O_2 + H_2O + 2e^{-} \rightarrow 2OH^{-} \quad (2)$$

and in acid solutions:

$$½O_2 + 2H^{+} + 2e^{-} \rightarrow 2\,H_2O \quad (3)$$

which occur spontaneously.

The rust formation starts at pH > 4 with the precipitation of $Fe(OH)_2$ and continues with the further oxidized by O_2 to Fe_3O_4 and FeOOH or $Fe_2O_3{\cdot}H_2O$.

The continue formation of the rust film is related not only to the presence of oxygen or water but also to the salinity. So, salinity control becomes an important feature, especially in the submarine excavation archaeology for the preservation of artefacts.

The structure and composition of the film of rust consisting of several polymorphs of oxy/hydroxide of iron, detailed in the section (A1.2) summarized as follow:

- **Goethite**, α-FeO(OH), has been used as an ocher pigment since prehistoric times.
- **Akageneite** is the β polymorph, formed by weathering and noted for its presence in some meteorites and the lunar surface. However, recently it has been determined that it must contain some chloride ions to stabilize its structure, so that its more accurate formula is $FeO_{0.833}(OH)_{1.167}Cl_{0.167}$.
- **Lepidocrocite**, the γ polymorph, is commonly encountered as rust on the inside of steel water pipes and tanks.
- **Feroxyhyte** (δ) is formed under the high-pressure conditions of sea and ocean floors, being thermodynamically unstable with respect to the α polymorph (goethite) at surface conditions.
- **Green rust** is a generic name for various green crystalline chemical compounds containing iron (II) and iron(III) cations, the hydroxide (HO^-) anion, and another anion such as carbonate (CO_3^{2-}), chloride (Cl^-), or sulfate (SO_4^{2-}), in a layered double hydroxide structure.

A.1.2. Iron polymorphs in Marine Atmospheres

1.2.1. Green Rust

Green rusts (GR) occur when anions like Cl^-, SO_4^{2-}, etc., replace OH- ions during the redox processes Fe(II)- Fe(III) oxyhydroxide in barely aerated environments. They are amorphous and unstable intermediate products, they show a greenish-coloured, for this reason named Green Rust [7]. GR cans contain primarily monovalent anions such as OH^- and Cl^- (GR1), or it cans contain mainly divalent ions such as CO_3^{2-} and SO_4^{2-} , called GR2 [8].

Green rusts stoichiometry and composition depends on the particular environmental conditions; therefore, they are rarely defined. The formula of GR1 and GR2 was reported by Refait et al.:

GR1 $[3Fe(OH)_2 \cdot Fe(OH)_2Cl \cdot nH_2O]$, with Cl^-/Fe^{3+} ions ratio equal to one,

GR2 $[2Fe(OH)_3 \cdot 4Fe(OH)_2 \cdot FeSO_4 \cdot nH_2O]$[9].

The same authors proposed a pyroaurite-similar crystalline structure, containing a random Fe atoms distribution among the octahedral positions. Furthermore, the Cl^- and O_2 (from water) occupy the interlayers.

GR1 can be prepared in several ways:

- by aerial oxidation of $Fe(OH)_2$ suspensions with dissolved $FeCl_2$.

- by oxidation of an initial $Fe(OH)_2$ layer or by direct precipitation in the simultaneous presence of Fe^{2+} and Fe^{3+} dissolved species.

$7Fe(OH)_2 + Fe^{2+} + 2Cl^- + ½O_2 + (2n + 1)H_2O \rightarrow$
$2[3Fe(OH)_2 \cdot Fe(OH)_2Cl \cdot nH_2O]$,

- By electrochemical technique, used in this work. [10]

1.1.2. Akaganéite (β-FeOOH)

In the rust Akaganéite, the β phase of the polymorphs of ferric oxyhydroxides (-FeOOH), plays a key role in the corrosion process. The crystalline structure is stabilized by the presence of halogens like Cl^-, which is strictly link to this oxyhydroxide. $FeO_{0.833}(OH)_{1.167}Cl_{0.167}$ is the chemical formula that was reported by Stahl et al. for the first time [11]. About the structure Watson et al. [12] suggested that at the subcrystal level the square prisms contained a circular central tunnel along all the subcrystals. These tunnels show a diameter of 0.21-0.24 nm, stabilised by 0.25-0.50 mmol/mol of Cl- ions (from 2 to 7 mol %) [13]. The Cl^- room temperature leaching by washing not occurs, because of the Cl^- ions are into the crystalline lattice [11, 14].

Akageneite unit cell is monoclinic with eight formula units per unit cell as tested by XRD[15]. Crystallographic structure is very close to the hollandite one ($BaMn_8O_{16}$) because of the tunnels are parallel to

the lattice C-axis. Characteristic tunnel-structure causes a minor density compared to the other oxyhydroxides (goethite and lepidocrocite)[16, 17].

Akaganéite can be synthesized by hydrolysis of acid $FeCl_3$ solutions at 25–100 °C.

The akageneite formation mechanism occurs when iron is exposed to a Cl^--rich marine atmosphere: firstly, the accumulation of Cl^- ions in the aqueous lead to the formation of $FeCl_2$, which gradually hydrolyses as:

$$FeCl_2 + 2H_2O \rightarrow Fe(OH)_2 + 2HCl, [15] \quad (1)$$

At interface takes place a very slow process through metastable precursors. So, the Cl^- ions accumulate combined with acidic conditions (pH range 4-6), cause the formation of ferrous hydroxychloride (β-$Fe_2(OH)_3Cl$)[18,19].

The total oxidation process require a long time and conditions above-mentioned, it can be summarised by the reaction [9, 19, 20]

$$FeCl_2 \rightarrow \beta\text{-}Fe_2(OH)_3Cl \rightarrow GR1\ (Cl^-) \rightarrow \beta\text{-}FeOOH, \quad (2)$$

1.1.3. Magnetite (Fe_3O_4)/Maghemite (γ-Fe_2O_3)

The structure of magnetite has a face-centred cubic unit cell where each unit cell is made up by eight formula units [13]. In spite of other oxyhydroxides, Magnetite includes both divalent and trivalent iron as described by the formula $Fe^{III}\ [Fe^{II}Fe^{III}]O_4$, where the brackets indicate octahedral sites, even though a mixture of tetrahedral and octahedral layers interchange [13].

About the stoichiometry, magnetite shows Fe^{II}:Fe^{III} ratio of 0.5, and Fe:O ratio of which varies from 0.750 to 0.744 [21]. Furthermore, in order to preserve the electroneutrality, the accommodation of H_2O or OH^- into magnetite vacancies (octahedral sites are favourite), is balanced by the ferrous and ferric ions valence electrons.

On the other hand, maghemite presents Fe the trivalent state mainly, if compared to magnetite. But they show the same cubic unit cell and the vacancies are limited to the octahedral sites [13]. Maghemite defects with the Fe:O ratio, which is in the range of 0.67–0.72 [21].

The similarity of maghemite with the magnetite phase and other phases prevent a differentiation during the corrosion process by XRD as well.

However, both of them can originate from the $Fe(OH)_2$ or green rust oxidation, alternatively from the lepidocrocite reduction in limited-oxygen environment according to[22] :

$$2\gamma\text{-FeOOH} + Fe^{2+} \rightarrow Fe_3O_4 + 2H^+ \quad (3)$$

Schematically, magnetite particles are obtained by the reaction of ion Fe^{2+}_{aq} with ferric oxyhydroxide species (Eq. (18)) following a precise order: akaganéite > lepidocrocite >> goethite [23, 24]. The formation of magnetite can be represented as the following reaction:

$$Fe^{2+} + 8FeOOH + 2e^- \rightarrow 3Fe_3O_4 + 4H_2O \quad (4)$$

Several studies report that the spinel phase is related to the electrochemical reduction [20, 25]. Several techniques allow to characterize the phases of oxyhydroxides, i.e. X-ray spectroscopy (XPS) or TEM can check the magnetite amount [25]. Furthermore, FTIR is a reasonably diagnostic technique to discriminate the same oxidation state-phases (maghemite or magnetite) [26].

A. 1.3 Mechanism of rust formation and akageneite role

Several studies were carried out in order to check the salinity role during the corrosion process. Especially, Stratmann focused on the atmospheric rusting cycle mechanism [27], studying the phase transition rust layer electrochemically. In a few words, when the iron sample was wetted, the iron dissolution was balanced by the pre-existing rust layer reduction (lepidocrocite), rather than by a

reaction with oxygen. Hence, three-step mechanism was proposed for the wet/dry transition showed in Figure A.2.

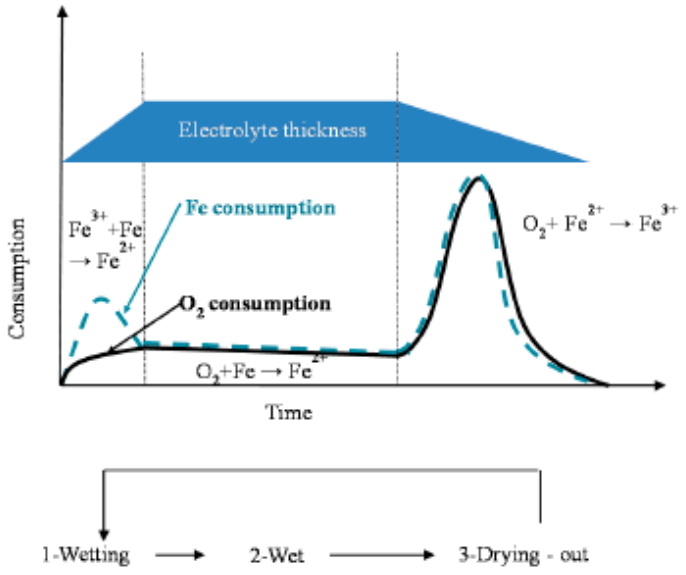

Figure A.45 Schematic representation of iron consumption/ time in wet/dry transition. [27].

Other tests clarified that corrosion acceleration was caused by the Cl^- ions, particularly from 10 to 100 mg $Cl^-/m^2 \cdot d$.

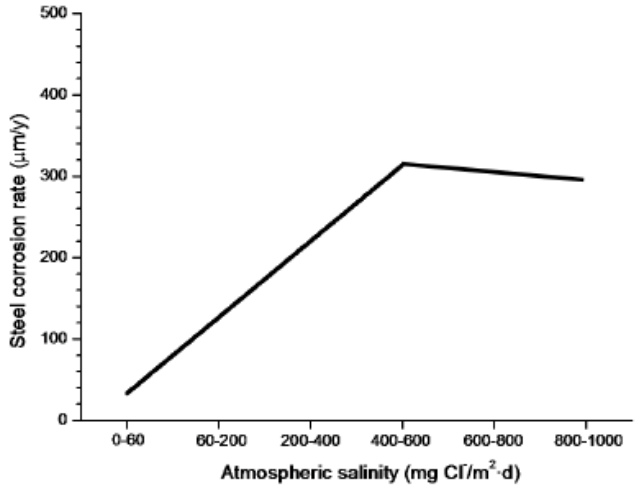

Figure A.46 Variation in the corrosion rate of mild steel with salinity over a broad spectrum of atmospheric salinities. The graph shows a trend. [28]

Nishimura et al. [25, 29] studied the correlation between the corrosion rate and the NaCl concentration during wet/dry conditions. The results suggest a linearity of the NaCl concentration and

akaganéite/lepidocrocite weight ratio, from a NaCl concentration above 0.05 wt % exclusively.

During the wet and dry phases akaganéite was reduced to an amorphous oxide and re-oxidized respectively (Fig.A3).

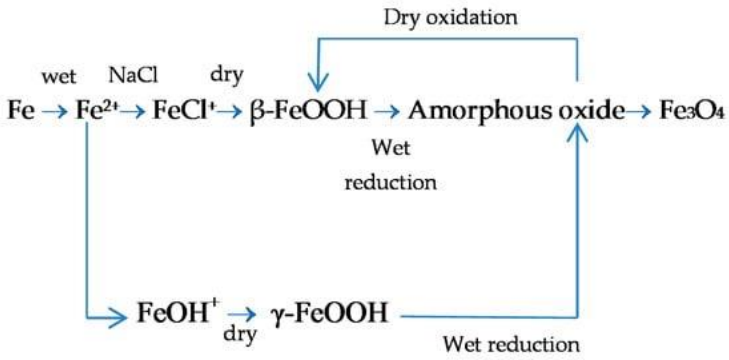

Figure A3. Rusting model of iron in wet and dry corrosion condition containing NaCl [29].

Later, Nishimura et al. observed the formation of akaganéite from GR1 during the drying and it was related to the Cl^- ion concentration [25]. Furthermore, only lepidocrocite formation from $Fe(OH)_2$ was observed at low Cl- concentration, associated to a low corrosion rate. While, the akageneite formation was associated to a high corrosion rate, caused by a high Cl- concentration. From in-situ XRD analysis is possible well-understand the process involved: at low Cl- concentration, GR1 wasn't evaluated, and it increased in 180 min. After 12 h, GR1 was transformed completely in akageneite.

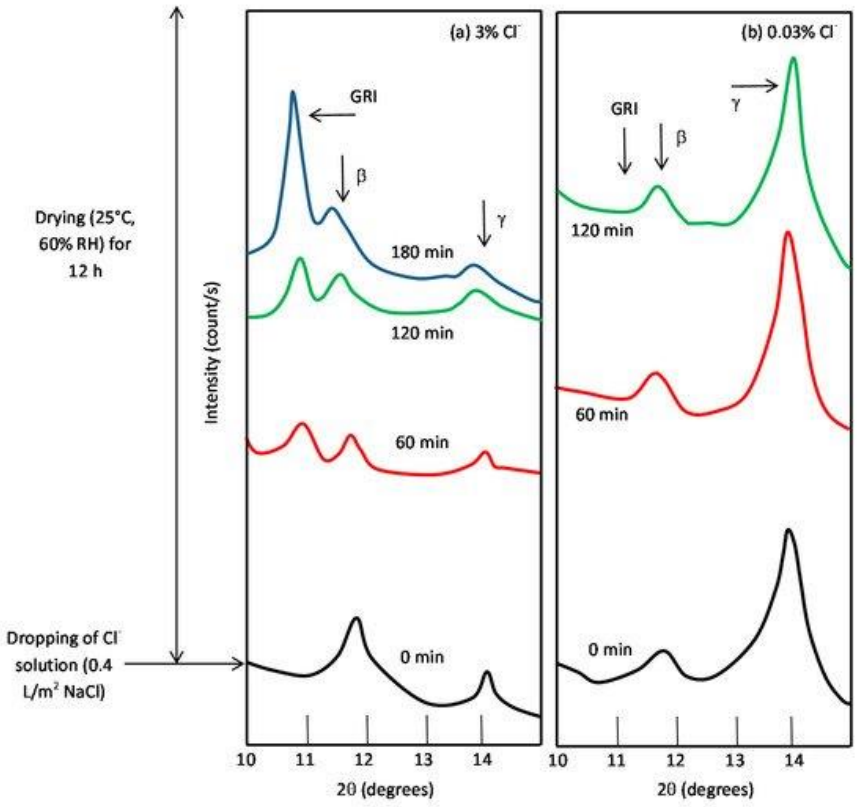

Figure A4. In-situ X-ray diffraction (XRD) results in wet and dry corrosion test using (a) 3% Cl^- and (b) 0.03% Cl^- solution[25].

In conclusion, in a Cl^--rich environment akageneite production is prevalent over the lepidocrocite and magnetite.

The authors carried out XPS and TEM observations on those portions of iron rust that could not be detected by XRD. It was determined that they contained large amounts of spinel oxide (magnetite structure) with bivalent/trivalent iron. This spinel oxide may have been formed by reduction of akaganéite during the wet process of the cycle. The growth of corrosion layer is due to the stabilization of the compounds thorough processes such as hydrolysis, crystallisation, nucleation, etc., controlled by three factors: temperature, time, and pH. Indeed, the rusting process involves by autocatalysis, where the oxidized iron (Fe^{2+}) is balanced by the reduction of magnetite (wet stages), which is re-oxidized thanks to the oxygen perfusion and H_2O-free access[30]. This process happens cyclically, promoting the autocatalytic layer growth.

Misawa describes the following mechanism for rust formation (Fig.A5)[31]:

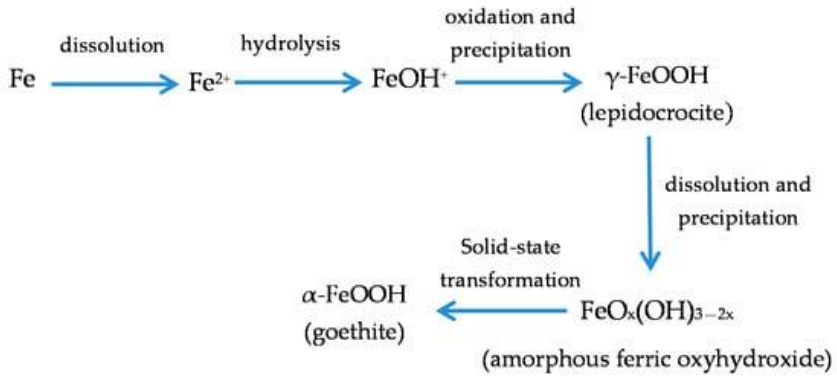

Figure A5. Mechanism for the rusting process according to Misawa [31].

The acidic dissolution of iron lead to the lepidocrocite formation through the hydrolysis of Fe^{2+}. Dissolution and precipitation of lepidocrocite can occur with the weather changing. Drying process simplify the lepidocrocite crystallization. Then, it is transformed in amorphous ferric oxyhydroxides, which turn into goethite by water supply.

Hence, unstable oxyhydroxides are the first compounds that formed in contact with the iron surface. These compounds transform into lepidocrocite because of the oxygen-free-access on the surface. Then, $Fe(OH)_2$ containing Cl^- complex turns into akaganéite and magnetite in the middle layer, between oxyhydroxides and lepidocrocite.

A1.4. Iron corrosion and cultural heritage

The same iron corrosion problems described above, are observed in ferrous archaeological artefacts, which conservation results hard because of the presence of chlorinated phases. Indeed, the “habitat” of the artefacts changes after the excavation, whereas the upset equilibrium is supplied by oxygen, accelerating the corrosion process[32, 33].

Artefacts irreversible degradation occurs with cracking or swelling of the rust layer, which causes the rapid deterioration of the core. Surely, this process involves both in marine atmosphere and in soil.

Akageneite is the corrosion product which catalysed the rust formation in presence of Cl^-. Several studies report the importance of the desalinization [34]. But it is necessary to know the mechanisms in which Cl^- ions are involved. As a matter of fact, Refait and al.[9, 19] report the linking between the corrosion evolution and the pH, O_2 and Cl^- ion concentration. They studied how the $[Cl^-]/[OH^-]$ ratio influences the formation of specific products:

- If $[Cl^-]/[OH^-]>1$, the product will be $Fe_2(OH)_3Cl$
- If $[Cl^-]/[OH^-]<1$, the product will be $Fe(OH)_2$
  In both cases they will form intermediate products Fe^{II} and Fe^{III} such as GR1.
- If $4<[Cl^-]/[OH^-]<8$, the final oxidation products will be α-FeOOH and β-FeOOH
- If $[Cl^-]/[OH^-] >4$ only β-FeOOH will form.

Finally, the hydroxychloride crystallise in a hexagonal–rhombohedral structure, similar to paratacamite ($Cu_2(OH)_3Cl$)[35].

Although some studies report the presence of the oxyhydroxide akageneite β-FeOOH [36, 37], identifying the ferrous hydroxychloride β-$Fe_2(OH)_3Cl$ (as precursor of akageneite) results hard in the iron archaeological artefacts.

A.2 Experimental

Materials

Chemicals were reagent grade from Sigma-Aldrich ($(NH_4)_2SO_4$, $(NH_4)_2Fe(SO_4)_2$,NH_4Cl, $FeCl_2$, NaOH, KCl, KNO_3) and used without any further purification. All experiments have been performed in air, at room temperature and with Millipore Milli-Q nanopure water with a resistivity of ≈ 17MΩcm.

Apparatus

Electrochemical measurements were performed with a Model 730e and 660c (CH Instruments) electrochemical workstation using a standard three-electrode electrochemical glass cell (10 ml). The substrate of the working electrode was glassy carbon, GC (diameter »0.7 mm) or graphite foil, GF (0.10 mm thick, 99.9%, Goodfellow) or *paraffin-impregnated graphite* rods (PIGEs) used for VMP experiments; and a Pt counter electrode was used. All potentials were reported vs Ag/AgCl reference electrode in saturated KCl.

Preparation of modified electrode

GR thin films were deposited on GCE on a solution of 0.2M $(NH_4)_2SO_4$, 0.02M $(NH_4)_2Fe(SO_4)_2$,0.4 M NH_4Cl, 0.02M $FeCl_2$. The solution pH was set at 8.1 with 1M NaOH. [10] The electrodes were immediately rinsed with water and characterized in a deaerated KCl or KNO_3 solution.

Paraffin-impregnated graphite rods (PIGEs), used for VMP experiments, were prepared as reported [38–40]. For our aim PIGEs, have a diameter of 1 cm. The sample was collected by a gentle circular rubbing of the graphite "pencil" on the surface. Voltametric characterization was carried out using microsamples of the corrosion layer.

A.3 Results

Electrochemical characterization

Green rust thin film was obtained on GCE through the procedure detailed in experimental section, where these reaction takes place:

$$Fe \rightarrow Fe^{2+} + 2e^- \quad (5)$$

$$Fe^{2+} + 8\ FeOOH + 2e^- \rightarrow 3\ Fe_3O_4 + 4H_2O \quad (6)$$

It is worth noting that the thin film electrodeposition occurs when the solution is freshly prepared exclusively, maybe because of the acid regeneration cycle, which was reported by Askey et al. [41]:

$$2Fe(s) + 4HCl(aq) + O_2(g) \leftrightarrows 2FeCl_2(aq) + 2H_2O$$

$$2FeCl_2(aq) + 3H_2O + \frac{1}{2}O_2(g) \leftrightarrows 2FeOOH(s) + 4HCl\,(aq)$$

The perfusion of oxygen moves the balance vs the iron formation, hence the loss of Fe^{2+} (aq) amount leads to the formation of oxyhydroxides in solution that does not allow the deposition.

GR-GC modified electrode electrochemical behaviour was explored in potentiodynamic conditions.

CV scans were carried out in a 0.1M KCl solution at $0.1Vs^{-1}$. Voltammogram shows (Fig.A6) three redox peaks related to three redox species. They are involved in cross reactions during the redox process, in fact when the current of A and B species decreases, the current of C' increase. It is worth noting that the redox couple A/A' decrease quickly and an isopoint is present at about -0.4V. this behaviour underlines the coexistence of different compounds which change with potential variation.

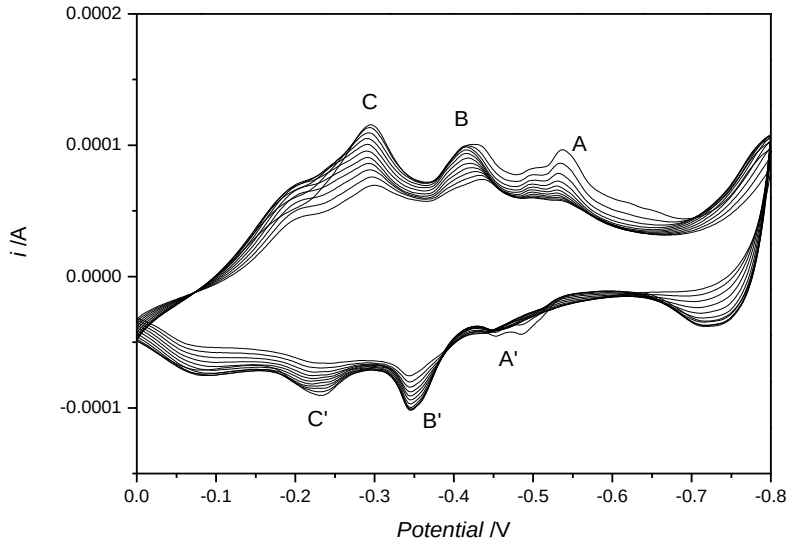

Figure A6. CV of GR film on GCE in 0.1M KCl at 0.1 V/sec. OCP: -0.3 V

In particular, to understand GR film kinetic, it was studied by CV at several scan rates. As shown in the log(v)-log(ip) plot (Fig.A7), the slope value is about 1, that suggests a surface-controlled process for

the insertion/deinsertion of Cl^- ions inside the structure. In this case, cathodic current has been reported.

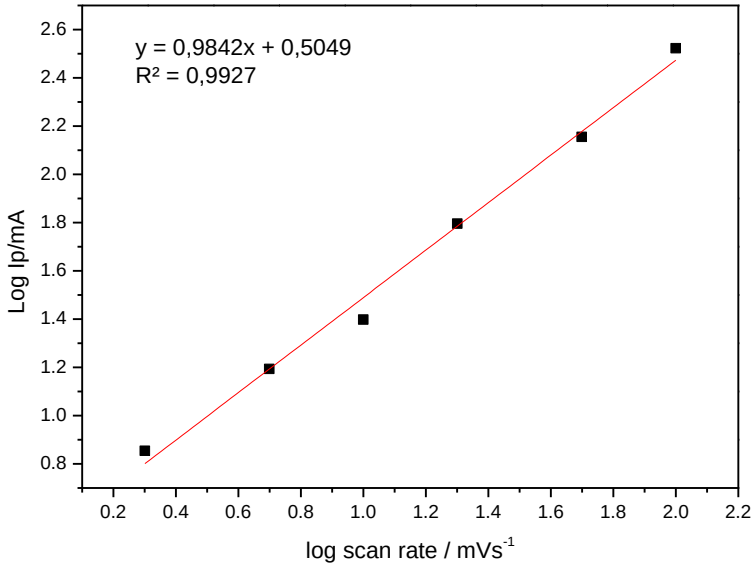

Figure A7 Log(v) vs log(ip) plot of GR film in KCl 0.1M.

Furthermore, GR-CV behaviour was studied in several concentration of KCl in order to highlight the contribution of Cl^- ion. On one hand, Cl^- ion concentration influences the peak position, on the other hand it is related to the specific specie.

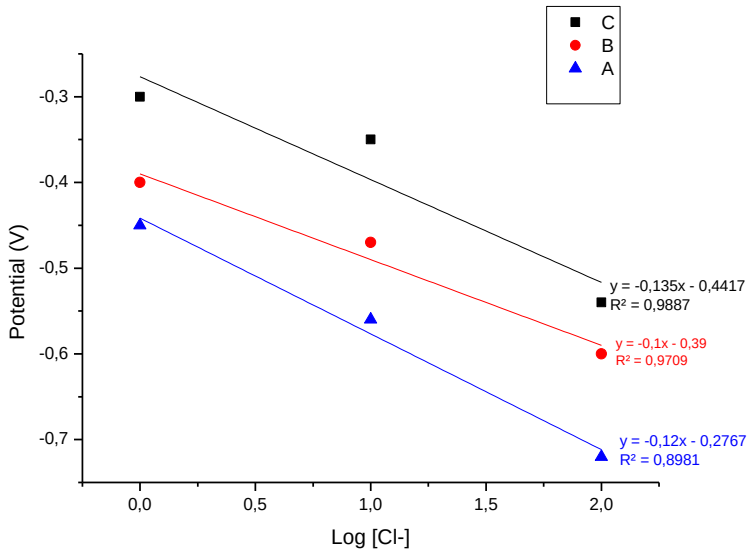

Figure A8. Ep vs log [Cl^-] GR at 0.1 V/sec vs Ag/AgCl.

In the figure A8 has been well-showed the potential variation of each specie in different support electrolyte concentrations: KCl 0.01M, 0.1M and 1M.

The reactions involved are described by Eq. 5 and 6. The system appears more complicated as attest the slope value of 120 mV.

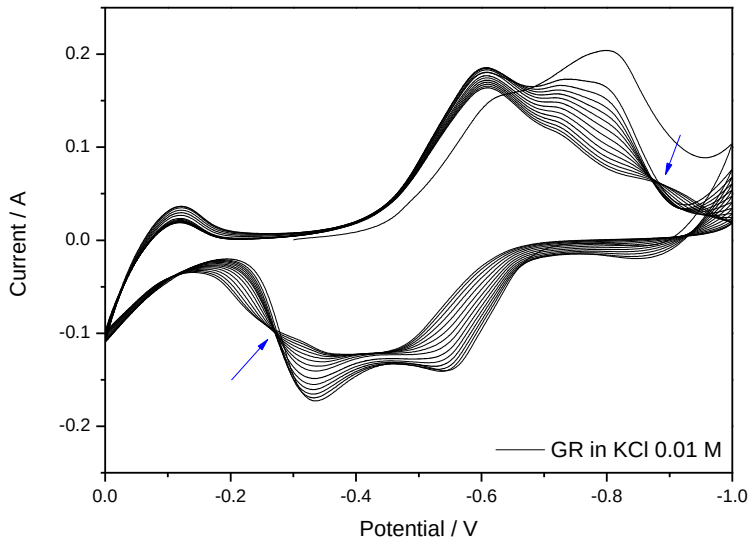

Figure A9. CV of GR film in KCl 0.01M

Particularly this behaviour could be influenced by the presence of chloride ions not only in the support electrolytes but into the structure as well. Indeed, CV of GR KCl 0.01M show a particular behaviour: two clear redox couple peaks are shown between -0.9/-0.6 V and -0.4/-0.3 V. In detail, two isopoints indicate the formation of the species during the redox process. An estimation of the cross reactions involved can be:

$$B + C \leftrightarrows Z + A \qquad (7)$$

$$A + e^- \rightarrow B \qquad (8)$$

$$C + e^- \rightarrow Z \qquad (9)$$

Where A/B and C/Z are two redox couple of iron oxyhydroxides.

Hence, to explore the role of Cl^- in the corrosion process, GR film was investigated also in electrolyte that are not involved in the redox

reactions, like KNO_3. In fact, plot in Fig.A10highlights the several species behaviour in different concentration of KNO_3 (full-black spot) and KCl (empty-red spot) solutions. It is worth noting that potential is related to the changing of Cl^- concentration, while for KNO_3 the potential endures about constant both for each specie and in different KNO_3 concentrations.

Species A, B and C are linearly influenced by the concentration of Cl^-, while species B and C are poorly influenced by KNO_3 concentration, except for specie A: potential shift of specie A is not linear with the concentration of KNO_3, showing a similar potential value in KCl.

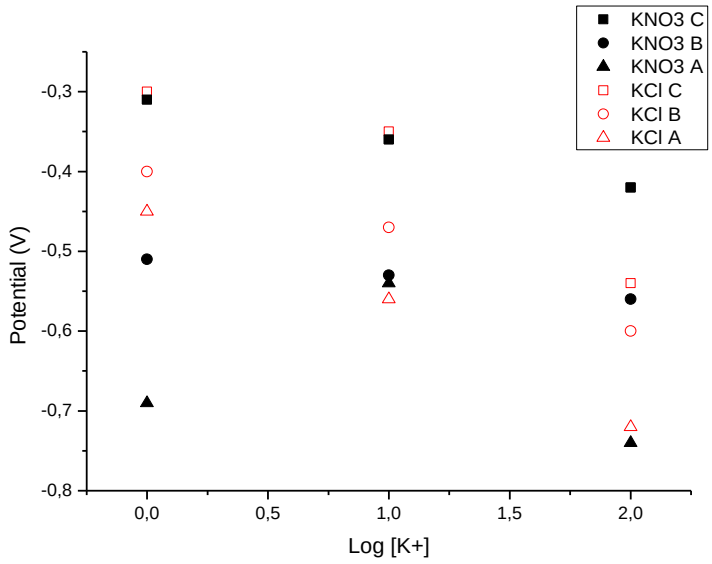

Figure A10. Potential vs log [K^+]. GR in KNO_3 (full-black spot) and in KCl (empty-red spot) at 0.1V/s vs Ag/AgCl.

As reported [42] akageneite is able to insert into its structure halogen as an ionic sieve, therefore GR film was studied in different electrolytes, such as KBr and KI, in order to obtain a CV in which akageneite could be distinguished.

As a matter of fact, CV of Green rust film in KBr 0.1M (Fig. A11) shows only one redox couple at Epc=-0.3 V, Epa=-0.6 V.

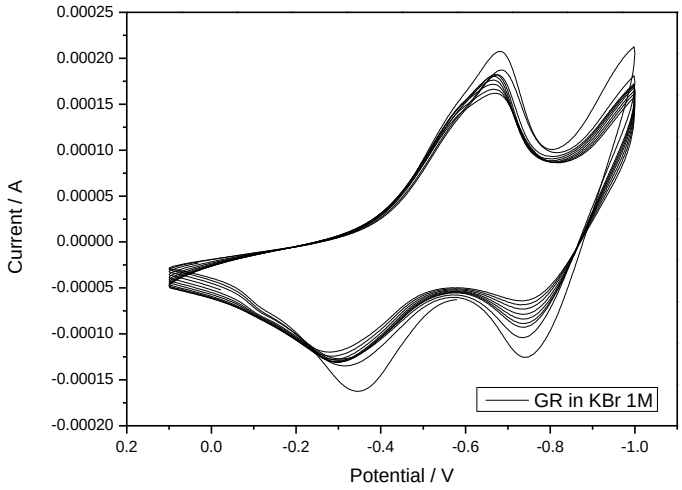

Figure A11. CV of GR film on GCE in 0.1M KBr at $0.1Vs^{-1}$

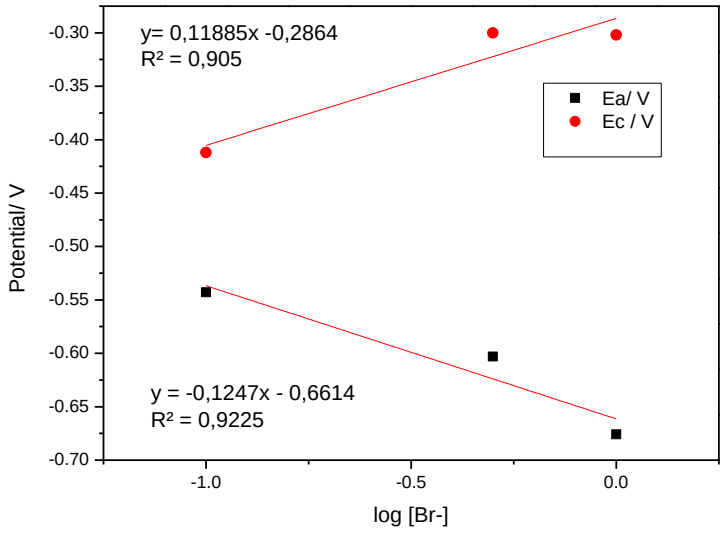

Figure A12. Ep vs log [Br^-] GR at 0.1V/sec vs Ag/AgCl.

Also in this case, the nerstian behaviour was followed (Fig. A12) with a slope of about 120mV, which indicates a two-electrons transfer reaction.

The same experiments were carried out in KI 0.1M (fig. A13, A14). GR film show only one redox couple as well, with a potential shifted

at higher potential (Epc= -0.1 and Epa= -0.3 V) than in KBr recorded.

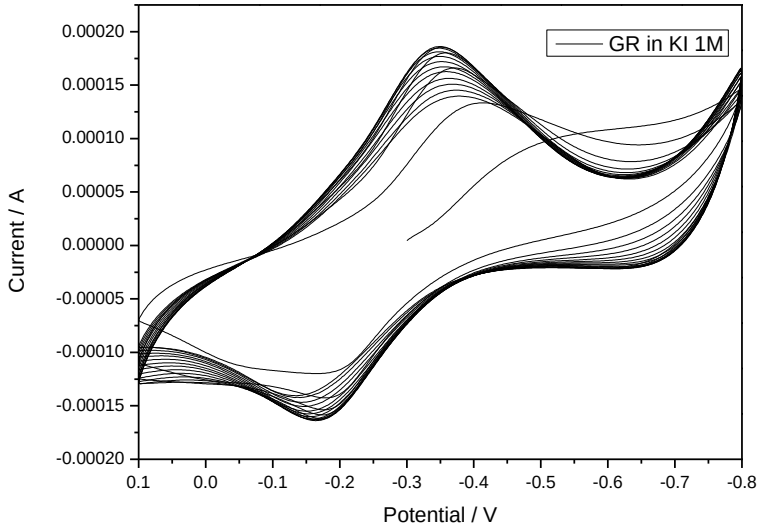

Figure A13. CV of GR film on GCE in 0.1M KI at $0.1Vs^{-1}$

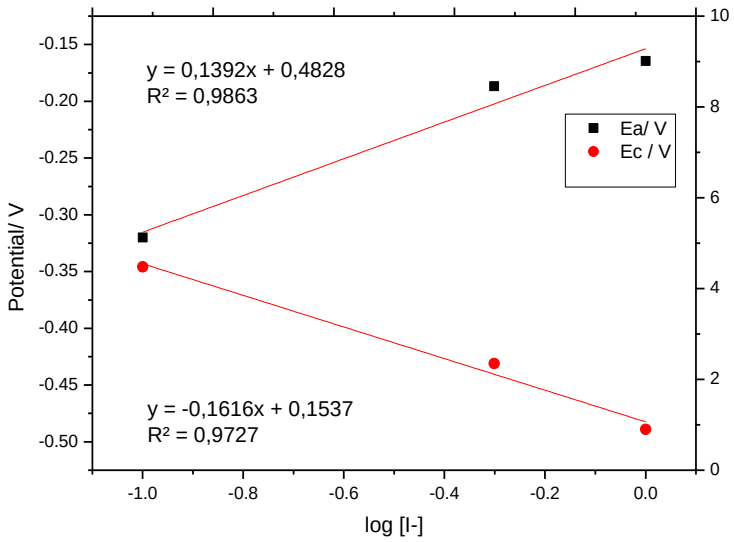

Figure A14. Ep vs log [I^-] GR at 0.1 V/sec vs Ag/AgCl.

Besides, a perfect linearity of potential vs log[I^-] was showed, with a slope value which suggest that this compound follows the Nerst equation.

Briefly, changing the anions of the support electrolyte occurs a considerable variation in CV morphology: the three peak voltammogram recorded in KCl changes in a single-peak voltammograms in KBr or KI 0.1M. This behaviour cans highlight firstly, the influence of chloride ions in the growth and evolution of green rust; secondly, it can be helpful for the identification of the species involved.

Finally, in figure A15 is showed the comparison between a real sample of rust, obtained though VMP technique, and the Green rust electrodeposited on GCE. The analysis was carried out by SWV at 0.1V/s from -1V to 1V and a three peaks voltammogram was obtained. The GR-GCE scan points out a peak at -0.55V, at 0.1V and at -0.75 V, all of them match with VMP Rust sample ones, confirming the GR deposited is rust. To facilitate the comparison the current of GR-GCE was normalized on VIMP Rust sample one.

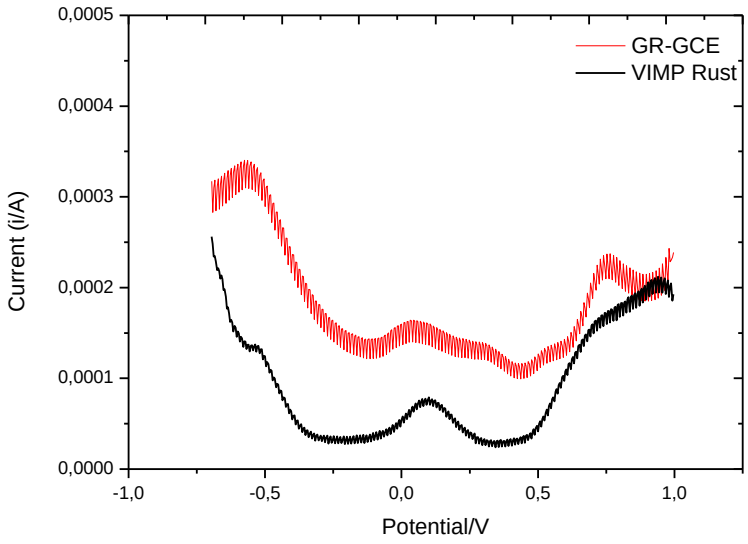

Figure A15. SWV of Rust-VIMP and GR-GC modified electrode in KCl 0.1M.

VMP technique allows to obtain data from real samples. In cultural heritages diagnosis, it results useful because it is a non-destructive Testing. In particular, this technique allows to obtain data from metallic material samples. In fact, metals usually show redox proprieties, which are easily tested electrochemically. Therefore, metal artefacts fit with VMP. Domenech et al. were the first at

testing this technique for copper artefacts dating [43]. In figure A16 a SWV of an old Eurocent and a new one, using VMP technique.

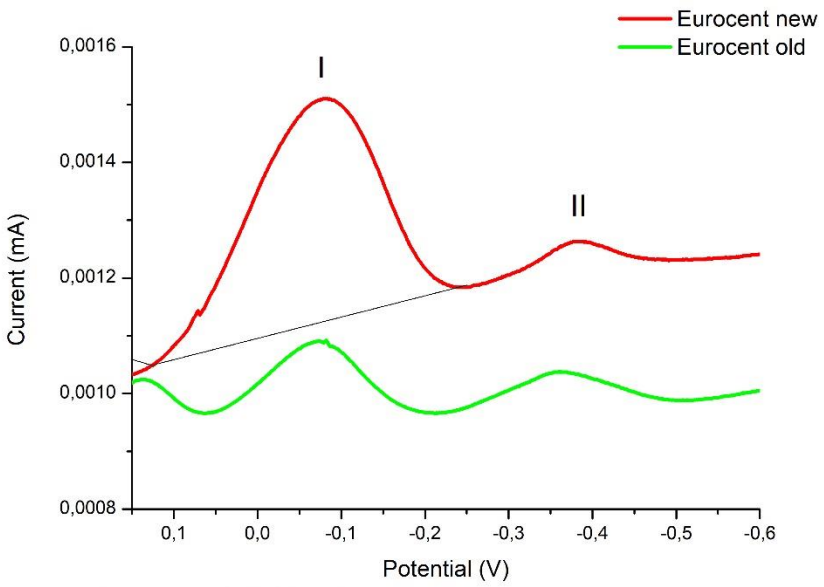

Figure A16. SWV of Eurocents in Acetate Buffer.

Also for ferric artefacts, VMP is a versatile test to obtain information about the aging or the components of the materials, such as the amount ratio of different copper hydroxides, as reported by Domenech et al. [44].

Thus, dating the artefacts is a simple procedure: the ratio of the two peaks II/I (figure 16) is an age marker. Surely, two main problems can be encountered: firstly, the results obtained depend on the area in which the sample is collected, the whole artefact is not considered; secondly, the ratio of the two copper hydroxides is related to the metal composition and structure of the artefact.

A calibration curve with standards, which are artefacts/sample dating known, and data normalization as a function of depth can obviate to the problems described above.

References

1. Leygraf C (2011) Atmospheric Corrosion. In: Corrosion Mechanisms in Theory and Practice, 3rd ed. CRC Press
2. Mansfeld FB (2020) Corrosion Mechanisms. CRC Press
3. Rozenfeld IL (1973) Atmospheric corrosion of metals. 229–229
4. Bernard MC, Joiret S (2009) Understanding corrosion of ancient metals for the conservation of cultural heritage. Electrochimica Acta 54:5199–5205. https://doi.org/10.1016/j.electacta.2009.01.036
5. Réguer S, Neff D, Bellot-Gurlet L, Dillmann P (2007) Deterioration of iron archaeological artefacts: micro-Raman investigation on Cl-containing corrosion products. Journal of Raman Spectroscopy 38:389–397. https://doi.org/10.1002/jrs.1659
6. Evans UR (1972) The rusting of iron: causes and control
7. Arroyave, C, Morcillo M (1997) Atmospheric corrosion products in iron and steels. Trends Corros 2:1–16
8. Butler G, Beynon JG (1967) The corrosion of mild steel in boiling salt solutions. Corrosion Science 7:385–404. https://doi.org/10.1016/S0010-938X(67)80052-0
9. Refait PH, Abdelmoula M, GÉnin J-MR (1998) Mechanisms of formation and structure of green rust one in aqueous corrosion of iron in the presence of chloride ions. Corrosion Science 40:1547–1560. https://doi.org/10.1016/S0010-938X(98)00066-3
10. Chung KW, Kim KB, Han S-H, Lee H (2005) Novel Synthesis of Nanosized Cellular Iron Oxide/Oxyhydroxide Thin Films: I. Electrochemical Synthesis of Green Rust Thin Films and Their Chemical Oxidation. J Electrochem Soc 152:C560. https://doi.org/10.1149/1.1945647
11. Ståhl K, Nielsen K, Jiang J, et al (2003) On the akaganéite crystal structure, phase transformations and possible role in post-excavational corrosion of iron artifacts. Corrosion Science 45:2563–2575. https://doi.org/10.1016/S0010-938X(03)00078-7
12. Watson JHL, Cardell RR (19620000) The internal structure of colloidal cyrstals of beta-FeOOH and remarks on their assemblies in schiller layers. The journal of physical chemistry 66:1757–1763
13. Cornell RM, Schwertmann U (2003) The Iron Oxides: Structure, Properties, Reactions, Occurrences and Uses. John Wiley & Sons
14. Rezel D, Genin JMR (1990) The substitution of chloride ions to OH−-Ions in the akaganéite beta ferric oxyhydroxide studied by Mössbauer effect. Hyperfine Interact 57:2067–2075. https://doi.org/10.1007/BF02405765
15. Post JE, Buchwald VF (1991) Crystal structure refinement of akaganéite. American Mineralogist 76:272–277
16. Mackay AL (1962) β-Ferric oxyhydroxide—akaganéite. Mineralogical magazine and journal of the Mineralogical Society 33:270–280. https://doi.org/10.1180/minmag.1962.033.259.02
17. Mackay AL (1960) β-Ferric Oxyhydroxide. Mineralogical magazine and journal of the Mineralogical Society 32:545–557. https://doi.org/10.1180/minmag.1960.032.250.04
18. Rémazeilles C, Refait Ph (2008) Formation, fast oxidation and thermodynamic data of Fe(II) hydroxychlorides. Corrosion Science 50:856–864. https://doi.org/10.1016/j.corsci.2007.08.017
19. Refait P, Génin J-MR (1997) The mechanisms of oxidation of ferrous hydroxychloride β-Fe2(OH)3Cl in aqueous solution: The formation of akaganéite vs goethite. Corrosion Science 39:539–553. https://doi.org/10.1016/S0010-938X(97)86102-1
20. Rémazeilles C, Refait Ph (2007) On the formation of β-FeOOH (akaganéite) in chloride-containing environments. Corrosion Science 49:844–857. https://doi.org/10.1016/j.corsci.2006.06.003
21. Fasiska EJ (1967) Structural aspects of the oxides and oxyhydrates of iron. Corrosion Science 7:833–839. https://doi.org/10.1016/S0010-938X(67)80116-1
22. Singh AK, Ericsson T, Häggström L, Gullman J (1985) Mössbauer and x-ray diffraction phase analysis of rusts from atmospheric test sites with different environments in Sweden. Corrosion Science 25:931–945. https://doi.org/10.1016/0010-938X(85)90022-8
23. Tanaka H, Mishima R, Hatanaka N, et al (2014) Formation of magnetite rust particles by reacting iron powder with artificial α-, β- and γ-FeOOH in aqueous media. Corrosion Science 78:384–387. https://doi.org/10.1016/j.corsci.2013.08.023
24. Ishikawa T, Kondo Y, Yasukawa A, Kandori K (1998) Formation of magnetite in the presence of ferric oxyhydroxides. Corrosion Science 40:1239–1251. https://doi.org/10.1016/S0010-938X(98)00045-6
25. Nishimura T, Katayama H, Noda K, Kodama T (2000) Electrochemical Behavior of Rust Formed on Carbon Steel in a Wet/Dry Environment Containing Chloride Ions. Corrosion 56:935–941. https://doi.org/10.5006/1.3280597
26. Antony H, Perrin S, Dillmann P, et al (2007) Electrochemical study of indoor atmospheric corrosion layers formed on ancient iron artefacts. Electrochimica Acta 52:7754–7759. https://doi.org/10.1016/j.electacta.2007.04.029
27. Stratmann M (19900000) The atmospheric corrosion of iron and steel. Metalurgia i odlewnictwo 16:45–52
28. Alcántara J, Chico B, Díaz I, et al (2015) Airborne chloride deposit and its effect on marine atmospheric corrosion of mild steel. Corrosion Science 97:74–88. https://doi.org/10.1016/j.corsci.2015.04.015
29. NISHIMURA T, TANAKA K-I, SHIMIZU Y (1995) Effect of NaCl on rusting of steel in wet and dry corrosion cycle. Tetsu-to-hagané 81:1079–1084
30. Evans UR (1965) Electrochemical Mechanism of Atmospheric Rusting. Nature 206:980–982. https://doi.org/10.1038/206980a0
31. Misawa T, Asami K, Hashimoto K, Shimodaira S (1974) The mechanism of atmospheric rusting and the protective amorphous rust on low alloy steel. Corrosion Science 14:279–289. https://doi.org/10.1016/S0010-938X(74)80037-5
32. Selwyn LS, Sirois PI, Argyropoulos V (1999) The corrosion of excavated archaeological iron with details on weeping and akaganéite. Studies in Conservation 44:217–232. https://doi.org/10.1179/sic.1999.44.4.217
33. Turgoose S (1982) Post-excavation changes in iron antiquities. Studies in Conservation 27:97–101. https://doi.org/10.1179/sic.1982.27.3.97
34. Selwyn LS, Argyropoulos V (2005) Removal of Chloride and Iron Ions from Archaeological Wrought Iron with Sodium Hydroxide and Ethylenediamine Solutions. Studies in Conservation 50:81–100. https://doi.org/10.1179/sic.2005.50.2.81
35. Oswald HR, Feitknecht W (1964) Über die Hydroxidhalogenide Me2(OH)3Cl, -Br, -J zweiwertiger Metalle (Me = Mg, Ni, Co, Cu, Fe, Mn). Helvetica Chimica Acta 47:272–289. https://doi.org/10.1002/hlca.19640470136
36. Zucchi F, Morigi G, Bertolasi V (19770700) Beta iron oxide hydroxide formation in localized active corrosion of iron artifacts. Corrosion and metals artifacts: a dialogue between conservators and archaeologists and corrosion scientists 103–105
37. Rinuy A, Schweizer F (1981) Méthodes de conservation d'objets de fouilles en fer. Etude quantitative comparée de l'élimination des chlorures. Studies in Conservation 26:29–41. https://doi.org/10.1179/sic.1981.26.1.29

38. Dubois F, Mendibide C, Pagnier T, et al (2008) Raman mapping of corrosion products formed onto spring steels during salt spray experiments. A correlation between the scale composition and the corrosion resistance. Corrosion Science 50:3401–3409. https://doi.org/10.1016/j.corsci.2008.09.027
39. Grygar T, Marken F, Schröder U, Scholz F (2002) Electrochemical Analysis of Solids. A Review. Collect Czech Chem Commun 67:163–208. https://doi.org/10.1135/cccc20020163
40. Bard AJ, Rubinstein I (1998) Electroanalytical chemistry: a series of advances. volume 20. M. Dekker, New York
41. Askey A, Lyon SB, Thompson GE, et al (1993) The corrosion of iron and zinc by atmospheric hydrogen chloride. Corrosion Science 34:233–247. https://doi.org/10.1016/0010-938X(93)90004-Z
42. Zhang D, Han X, Kong X, et al (2020) The Principle of Introducing Halogen Ions Into β-FeOOH: Controlling Electronic Structure and Electrochemical Performance. Nano-Micro Lett 12:107. https://doi.org/10.1007/s40820-020-00440-2
43. Domènech A, Scholz F (2019) Electrochemical Age Determinations of Metallic Specimens—Utilization of the Corrosion Clock. Accounts of Chemical Research 52:. https://doi.org/10.1021/acs.accounts.8b00472
44. Doménech-Carbó A, Doménech-Carbó MT, Capelo S, et al (2014) Dating Archaeological Copper/Bronze Artifacts by Using the Voltammetry of Microparticles. Angewandte Chemie 126:9416–9420. https://doi.org/10.1002/ange.201404522

Acknowledgement

I would like to express my deep and sincere gratitude to my research supervisor, Prof. Marco Giorgetti, for giving me the opportunity to discover the world of batteries. His sincerity and motivation have deeply inspired me. He has taught me the methodology to carry out the research and to present the research works as clearly as possible. It was a great privilege to work and study under his guidance, during the last year. I would also like to thank Prof. Mario Berrettoni who followed my research projects during the first two years. His friendship, empathy, and food passion, made me feel right at home. I am extending my heartfelt thanks to all the "Battery group- Bologna". Especially, I would like to thank Min and Mariam for their moral support and their tests on ZnHCF.

I am thankful to Prof. Paolo Conti and Prof.ssa Silvia Zamponi for his genuine support throughout this research work.

I am extremely grateful to my family for their patience. In particular, I would like to thank my grandparent Barbara, Antonio and Rosa, who taught the perseverance and determination. I am very much thankful to my sister Barbara and my brother in law for their support and presence, especially during the times of trouble. Also, I express my thanks to my parents and my aunt Rosa, who accepted my choose and understood the importance of this route. My Special thanks goes to Giuseppe, who was able to make me happy, also during trouble moments. A thank to my friends Martina, Giulia and Maria Giovanna for the keen interest shown to complete this thesis successfully.

I would like to say thanks to my friends and research colleagues, Irene, Benedetta, Paolina and Nuria for their constant encouragement

I am extending my thanks to the Tecnopolo of Rimini professors, students and colleagues for their kindness.

Finally, my thanks go to all the people who have supported me to complete the research work directly or indirectly.